Application of Radiative Fluid Dynamics Scaled from the Laboratory to Astrophysics

Joseph Edward Cross

St Hugh's College
University of Oxford

Thesis submitted for the degree of

Doctor of Philosophy in Atomic & Laser Physics

Michaelmas 2015

This thesis is dedicated to my
parents for always encouraging
me to do my best.

Acknowledgements

First and foremost I wish to thank my supervisor, Professor Gianluca Gregori, for all his help, guidance and support throughout my DPhil. Many times has he spotted an interesting angle to pursue, or pushed me to go further. Without doubt this body of work would not exist without him, and I am thankful for the opportunity he has given me.

I was lucky enough to also have the guidance of John Foster, whom I consider to be my secondary supervisor at AWE. John is the greatest experimentalist I know, and coupled with his modesty and thoroughness, he is also a great pleasure to work with. I have certainly learned a lot from working with John, and from his 'naive' questions which are always pertinent!

Of course, I was not the sole member of our group, and so I also thank my colleagues. Hugo offered advice and help both in the lab and the pub in equal measures (pints). Tom, as the senior student, gave guidance in work but also in exploring the social aspect of Oxford, which I am indebted to him for. Jena, Nick and Pawel offered useful advice in the lab, and at coffee. To the new students Alex and Mat (as well as Archie and Riccardo), I say thank you for helping me understand things better by having to try to explain them!

Outside of my group, I am fortunate to have met a great collection of people who have helped me with my Physics, but also made experiments, and time at Oxford, just that little bit more bearable and fun. Many thanks to Peter Norreys (for support and advice), Andy Higginbotham (for AWE advice), Carolyn Kuranz (for speaking to me on Facebook about Physics), Brian Reville (for always having the time to talk about theory), Chris Murphy (for conference advice), Ellie Tubman (I shall still be sending weekly emails), Rob Crowston (for much needed distraction at experiments and whilst writing, and also for being the font of all knowledge relating to Matlab, flights etc.), Chris Spindloe (who probably never wants to see me

again after all the visits relating to targets), Roman Yurchak (for helping me with French related matters) and to Émeric Falize and Michel Koenig (for all their help and support, and allowing me to lead the UK part of their experiment.)

I also owe AWE not just for sponsoring my DPhil, but also for the support, and welcome, they have given me. Colin Danson in particular has gone far beyond to make our experiment, and my presence at AWE, run smoothly, and I owe him a great debt. Peter Graham has tirelessly worked on simulations for us. Ed Gumbrell, John Skidmore and Sid Patankar were instrumental in the success of our optical diagnostics. Thank you also to all the people at the Orion laser for being so professional and efficient, without you the experiment would not have been half the success that it was.

I also owe RAL a great deal, from offering training courses, experiments, support for Orion experiments and for being lovely people to talk to. Everyone is always happy to help. In particular I would like to thank Mags, Dave and Rob.

While the DPhil has taken up a large portion of the past three years, it is also necessary to have some distraction. Thankfully this was offered tremendously by my fellow year students Shamim and Paul, we have had a lot of fun! Paul Jnr., Tom, Andrew, Chris, James, Dave × 3 and the rest of the Simon Room were a pretty good bunch to work with.

St Hugh's was a welcome retreat from work, and I met some great friends there. I want to thank Heather in particular for the support, discussion, and laughter over the past three years. Thanks also to Katharina, Fenner, Scott, Nick, Justin, Chrissy and Uljrike.

Outside of the University, I had the support of many friends: Greg, Rita, Adam, Becky, Bailu, Alun, Aquil, Katie, Laura, Ruth and many others.

Many thanks to my family. My Mum and Dad have always supported me through whatever I do: this thesis is for you. Thanks also to my sister, Kathryn, step-Dad, Paul, step-Mum, Sally, Granny Eve, Grandad, Uncle Clive, Auntie Ann, Auntie Bernita, Uncle Steve, Rachel and Michael.

Final thanks and gratitude to Marc for his support, patience, and help throughout this whole process!

Abstract

Since its inception, the laser has found numerous applications beyond anything that could have been foreseen at its creation. With scientific and technological advancements, lasers are now capable of delivering a large amount of energy in very short timescales: giving us the ability to form interesting states of matter such as plasmas. As it became possible to create such material on earth, it made sense to consider applications this could be used for.

Astrophysics typically uses a combination of observation, theory and simulation in order to further our understanding of the cosmos. The ability of the laser to create matter in similar states to those found in many astrophysical phenomena opened up a complimentary research area: laboratory astrophysics.

The thesis begins by describing the basic physics underlying plasmas and fluid theory, before extending this to a non-dimensional form in the ideal hydrodynamic case: the so-called Euler equations. A novel way of including non-ideal terms, such as radiative, magnetic and quantum effects, is shown. Restrictions, and guidelines, to creating suitable lab experiments are drawn from this, and an experimental analogue of a polar star system is described. The design, simulation, execution and analysis of the experiment, led by the author, is given. Good agreement is found between experimental results, simulations and astrophysical theory. An experimentally measurable quantity, the structure factor, is then derived from hydrodynamics, and extended to include radiative effects, using the framework introduced in the first section. The impact of including such effects is discussed and determined to be non-negligible. Finally, we conclude by drawing together all these areas.

Role of the Author

This thesis contains theoretical and experimental work relating to laboratory experiments, and the applicability of scaling this work to understand astrophysical events. The work was not performed alone, but as part of a series of collaborations with other scientists. In this section the author's contributions to the work will be clarified.

The introductory chapter 1 is written to inform the reader of the area of work in a general sense, and to place its importance, and history, in the wider scientific context. The background theory chapter 2 contains the necessary theory required as the starting point for understanding the rest of the work contained in this thesis. The content contained in both these chapters is reproduced from a variety of sources, of which the original authors are identified within the text.

Chapter 3 marks the beginning of the author's original work. It contains the expansion of the hydrodynamic equations to include the effects of radiative, magnetic and quantum effects. The idea was conceived by Gianluca Gregori and the author. Dimensional analysis, and definition of new characteristic ratios, was carried out by the author. Comparison to experiment was performed by the author and Gianluca Gregori. Brian Reville provided additional theoretical advice. The work was published in The Astrophysical Journal, see Cross et. al. (2014) (1).

Chapter 4 describes the preparation, execution and analysis of the POLAR experiment at the Orion laser facility in Aldermaston. The original experimental idea was conceived by Michel Koenig, Émeric Falize and others at the CEA, Observatoire de Paris and LULI, who carried out the previous experiment at LULI, École Polytechnique. The Orion experiment was conceived by Gianluca Gregori, John Foster and the previously mentioned French collaborators. The preparation and experiment was led by the author in two, two-week experimental blocks performed at the AWE's laser, Orion, Aldermaston in November 2013 and February 2014. Analysis was performed by the author and John Foster. Two-dimensional simulations were carried out by Peter Graham at AWE. One dimensional simulations were carried out by the author using the commercially available HELIOS and SPECT3D codes. The work is under review in Nature Communications.

Chapter 5 describes the derivation of the dynamic structure factor from hydrodynamics, but modified to include the effect of radiation for the cases of optically thick, and optically thin fluids. The idea was conceived by the Gianluca Gregori and the author. The derivation and analysis was carried out by the author. The work has been accepted for publication in Physical Review E.

Work contained in the appendices is reproduced from other sources, albeit slightly modified to fit the scope of this work. Original authors are clearly identified throughout the text.

Over the course of the DPhil, the author has had the opportunity to work with, and contribute to, various international collaborations which are not directly relevant to the work presented here. These are listed below:

- *POLAR Experimental Collaboration at LULI, École Polytechnique, Paris.* Part of the ongoing campaign to understand accretion column physics, of which the Orion experiment is part. The precursor experiment was performed in February 2013, led by Alex Pelka, with a further experiment looking at the effect of an externally applied magnetic field in December 2014, led by Alex Pelka and Roman Yurchak.

- *NLUF Collaboration at Omega, Rochester, NY.* NLUF Collaboration between Pat Hartigan, John Foster and, later, Carolyn Kuranz to perform astrophysically relevant laser experiments, with closer involvement of the astrophysical community. Work on Mach Stems was carried out, as well as experiments designed to observe the effect of magnetic fields and magnetic pressure, which the author was involved in the conception, design, and experimental team. Shot days in February 2013, October 2013, February 2014.

- *Amplified Magnetic Fields at Vulcan Laser, CLF, Rutherford Appleton Laboratory, UK.* Led by Jena Meinecke, Hugo Doyle and Gianluca Gregori in October 2013, this experiment continued the investigation into the amplification of magnetic fields by turbulence, to explain the source of magnetic fields in the universe. A paper on the use of a framing camera was published in IEEE Transactions on Plasma Science, see Tubman et al (2).

- *Laser-produced quasi-static magnetic fields at LULI, École Polytechnique, Paris.* Collaboration led by João Santos in May 2014. The experiment was investigating the production, and characterisation, of a strong, quasi-static magnetic field created by the interaction of a high intensity laser with a capacitor coil target.

The experiment is detailed in the paper in the New Journal of Physics, see Santos et al (3).

- *Carbon white dwarf crystallisation at Vulcan Laser, CLF, Rutherford Appleton Laboratory, UK.* Led by Paul Mabey, Hugo Doyle and Gianluca Gregori in September 2014. This experiment looked at the formation of a new phase of carbon, to understand the interior of white dwarf stars. A paper on the X-ray lens, a crucial diagnostic, was published in the Journal of Instrumentation, see Mabey et al (4).

Publications

First Author

- Cross, Reville and Gregori, "Scaling of Magneto-Quantum-Radiative Hydrodynamic Equations from the Laboratory to Astrophysics", *The Astrophysical Journal*, **759**, 59 (2014).
- Cross et al., "Laboratory analogue of a supersonic accretion column in a binary star system", *Nature Communications (with reviewers)*, (2016).
- Cross, Mabey, Gericke and Gregori, "Theory of Density Fluctuations in Strongly Radiative Plasmas", *Physical Review E*, **93**, 033201 (2016).

Other Publications

- Tubman et al., "Nanosecond Imaging of Shock- and Jet-Like Features", *IEEE Transactions on Plasma Science*, **42**, 2496 (2014).
- Mabey et al., "Characterization of x-ray lens for use in probing high energy density states of matter", *Journal of Instrumentation*, **10**, P04010 (2015).
- Spindloe et al., "Target Fabrication for the POLAR Experiment on the Orion Laser facility", *High Power Laser Science and Engineering*, **3**, e8 (2015).
- Santos et al., "Laser-driven platform for generation and characterization of strong quasi-staic magnetic fields", *New Journal of Physics*, **17**, 083051 (2015).

Fundamental Constants

Physical Quantity	**Symbol**	**Value (SI)**
Boltzmann Constant	k_B	1.38×10^{-23} J K^{-1}
Electron Charge	e	1.60×10^{-19} C
Permeability of Free Space	μ_0	$4\pi \times 10^{-7}$ N A^{-2}
Permittivity of Free Space	ε_0	8.85×10^{-12} F m^{-1}
Mass of an Electron	m_e	9.11×10^{-31} kg
Speed of Light in a Vacuum	c	3.00×10^{8} ms^{-1}
Stefan-Boltsmann Constant	σ	5.67×10^{-8} W m^{-2} K^{-4}
Reduced Planck Constant	$\hbar$	1.05×10^{-34} Js

List of Abbreviations

Abbreviation	**Name**
ISM	Interstellar Medium
HED	High-Energy-Density
WDM	Warm Dense Matter
RT	Rayleigh-Taylor (Instability)
ICF	Inertial Confinement Fusion
AWE	Atomic Weapons Establishment
LTE	Local Thermal Equilibrium
DSF	Dynamic Structure Factor
MHD	Magnetohydrodynamics
CV	Cataclysmic Variable (star system)
MCV	Magnetic Cataclysmic Variable (star system)
SOP	Streaked Optical Pyrometry
VISAR	Velocity Interferometer System for Any Reflector
GOI	Gated Optical Imager
SPCA	Static Pinhole Camera Array
TIM	Ten Inch Manipulator

Contents

List of Figures

List of Tables

CHAPTER 1

Introduction and Motivation

> *"Begin at the beginning," the King said, very gravely, "and go on till you come to the end: then stop."*
>
> – Lewis Carroll, *Alice in Wonderland*

This chapter introduces the concept of laboratory astrophysics, and the motivation for investigating it as a research area. A brief history of laser facilities used for laboratory astrophysics, and the history of experiments, is also given.

No other area of physics seems to attract so much attention and interest from the general public as astrophysics. From the time of the Ancient Greeks – looking up into the sky and separating space into the celestial and terrestrial realms – to the overturning of the theory of the earth-centred universe by Galileo, and the creation of the Hubble Space Telescope in the 1990s, advances in astrophysics have garnered a large following.

Traditionally astrophysics is a science of observation. First by the naked eye, and then using telescopes, much of what we understand comes from observance of light at varying wavelengths, and by related diagnostics (i.e. spectroscopy). Theoretical models are also devised, and checked against observation. More recently, computer simulations have also been used to investigate astrophysical environments.

Improvements in telescope engineering have led to better resolution, and allow us to probe further into different regions of space, but we are still limited to being a passive observer. Imaging rare cosmic events can still be a matter of luck: requiring that your telescope is looking in the right region, at the right time. Astronomical events can also occur over very large time scales, requiring the data be collected over the course of many years. As time on large telescope systems is increasingly at a premium, alternative methods of carrying out experiments would be welcomed. Of course, simulations also offer a chance to simulate large scale events at convenient times, but these are limited by the state of understanding of the physics at the time, and the cost of running a super-computer. Experiments are always required to validate simulation results.

Laboratory astrophysics thus offers an alternative experimental route. If we can create conditions in the laboratory that are similar to astrophysical events, then we can perform experiments on earth to aid our understanding of cosmic phenomena. Performing experiments in the laboratory has advantages: we can perform experiments at a much higher rate, and with greater control over the system's make-up. We also are able to actively probe the material, such as with X-ray radiography (see chapter 4), absorption spectroscopy etc. However; to do this we need to satisfy certain conditions to show that we can:

1. Create conditions required to match the astrophysical case,
2. Show that the underlying physics is independent of the scale of the system,
3. Design relevant experiments to further our understanding of specific astrophysical cases.

1.1 History of Laboratory Astrophysics

1.2 Lasers as a means to create a plasma

The requirement that we can produce astrophysically relevant conditions in the laboratory primarily rests on our ability to create a *plasma*. The majority of the visible matter* in the universe resides in the plasma state: particularly those of interest in astrophysics, such as around stars and in the interstellar medium [ISM]. We can generally think of a plasma as a form of ionised gas, where one, or more, of the electrons per atom is no longer bound in the atomic structure of its component atom. In order to create a plasma, we need to be able to impart a large amount of energy to overcome the internal atomic attractions and ionise the material. Lasers are one such way of delivering the required energy.

---

*The suspected presence of dark matter has somewhat diluted the simplicity of this claim, now requiring 'visible' as a qualifier.

The ability of a facility to be able to deposit such high energies means that the field is relatively young. Laser technology has only been sufficient to reach such conditions, that we call high-energy-density [HED] laboratory astrophysics, since the late 1980s/early 1990s. Lasers such as Shiva, (5), and Janus, Livermore, CA, USA were developed in the 70s and worked in the terawatt power regime.

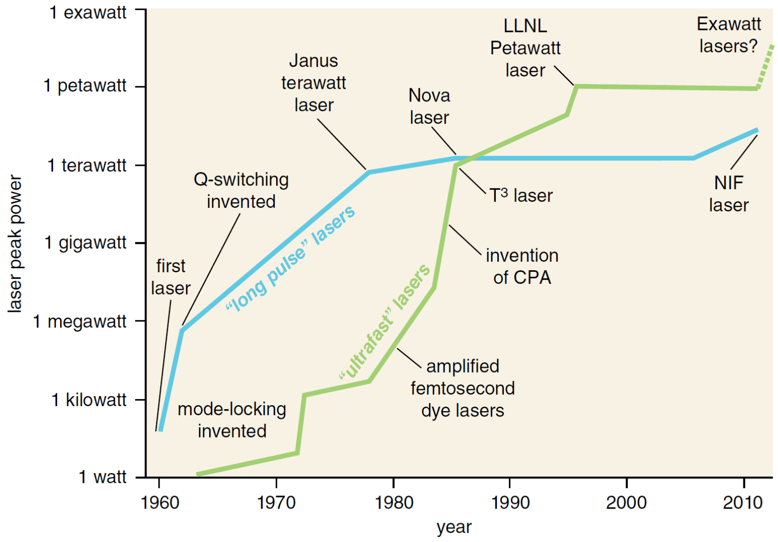

Figure 1.1: Overview of the advances in laser power from 1960s to early 2010s. The introduction of a new laser technology causes a jump in the power reached. Reproduced from (6).

Subsequent work led to lasers such Omega, in Rochester, NY, USA (7); Nova, in Livermore, CA, USA(8); Gekko XII, in Osaka, Japan (9); LULI, in Paris, France; Vulcan in Harwell, UK; and Helen in Aldermaston, UK in the 80s & 90s where laser energy was in excess of the kilojoule level, and systems contained multiple beam lines. Much higher laser energies were possible in the 2000s, such as NIF, Livermore, CA, USA; Orion, Aldermaston, UK, as well as upgrades to many of the previous laser systems. With such systems work began in earnest on HED laboratory astrophysics as it was now easier to reach, reproducibly, the temperatures, densities and pressures of plasma required.

With each successive jump in laser technology, the parameter space that can be accessed has increased. This has implications for both fluid, and warm dense matter regimes[†]: higher pressures allow for more extreme states of matter can be created, coupled also with improved control of laser properties (such as spatial and temporal

---

[†] Warm Dense Matter [WDM] refers to material that is around normal solid density, but is heated above standard conditions. Many planetary cores would be described as warm dense matter.

pulse shaping), and, for fluids, higher velocities and temperatures mean we can leave the realm of ideal hydrodynamics and explore radiative and magnetic effects (10; 11).

It is worth mentioning that there are other methods of producing the correct conditions for laboratory astrophysics: namely pulsed power machines, such as a Z pinch. The plasma in this case is formed by passing a very high current through a thin wire in a very short time (of the order of nanoseconds). The wires themselves then explode and launch a plasma flow, by action of the $\boldsymbol{J} \times \boldsymbol{B}$ force. By using different orientation of the wires, an array of different experiments can be performed. Astrophysically relevant experiments are similar to those that can be achieved with laser-produced plasmas, such as investigation into the formation of astrophysical jets (12). Two such machines are the Z machine in Sandia National labs, NM, USA and MAGPIE at Imperial College London, UK.

1.3 First Laser Experiments

One of the first laboratory HED astrophysics laser experiments involved the investigation of hydrodynamic instabilities of relevance to supernovae (13; 14). When supernovae explode, material can be ejected in many layers, with each having a different make-up of elements. The interactions between these layers can become unstable as a result of their physical properties, such as the relative density, which causes the two layers to mix. At the time of the experiment, the timescale of the mixing could not be explained by current theory: simulations predicted the mixing would occur at half the speed that observation of the supernova explosion showed. The ability to create an analogue of these mixing condition in the lab was thus of great interest.

The target was designed in an ‘indirect drive’ orientation with the laser being used to generate a thermal field of X-rays which, in turn, were used to accelerate a two layered target of copper and plastic. This allowed for investigation of the Rayleigh-Taylor instability [RT] with active probing, and at various times along its evolution. Not only did this experiment provide a stream of data to compare with simulated results, and thus to understand where the difference arose, but it also gave evidence for use in supporting various theories. Thus the concept of a laboratory analogue to an astrophysical event was introduced, and experimental planning began more completely. Previously, due to lower laser energy, laboratory astrophysics experiments had concentrated more on understand one feature of, say, the atomic physics; such as low-energy nuclear cross-sections (15). The greater laser energy now allowed for us to simulate an entire system, and observe it dynamically evolving.

Since 1997, the number of astrophysically motivated laser experiments has grown substantially. From the mixing caused by instabilities in supernova explosions (16), physics of supernova remnants (10; 17; 18), to formation of astrophysical jets (19; 20), and sources of magnetic field in the universe (21), many new areas of astrophysics have been probed by novel, earth-based experiments.

The advent of the laser systems, and interest in laboratory astrophysics, has been aided by other complimentary experiments that can be performed with lasers. One major driver, for which lasers such as Shiva, Nova and Omega were constructed, was to achieve fusion power via Inertial Confinement Fusion [ICF], (5). Weapons research, made even more important following the introduction of the Comprehensive Nuclear-Test-Ban Treaty in 1996, also requires conditions similar to those created for ICF and laboratory astrophysics, and thus also provided funding for construction of high-power laser facilities, such as the Helen and Orion lasers of AWE, Aldermaston, UK.

1.4 Scaling

Whereas ICF and weapons research require similar conditions to be created to those required for laboratory astrophysics, they do not require the same stringent conditions for scaling between the laboratory and astrophysics. Thus of equal importance to the rise of laser systems capable of creating these conditions was the theory behind scaling of the fluid equations (16). Again, this has been expanded beyond hydrodynamics to include many other effects, as will be detailed in chapter 3.

While the equations that describe the motion of plasma are the same wherever and at whatever scale[‡], it is not immediately obvious that this means experiments at small scale (in a lab) have any use, or application, to what happens on a large scale (in space). However, it can be shown that these equations can be rewritten in such a way that does *not* depend on the scale of the system, be that time, space, velocity etc. We can expect the small and large scales to evolve in similar ways, and that understanding something in the lab would have useful implications for understanding cosmic events, under certain conditions. For ideal conditions, this rewriting of the equations turns out to be relatively simple. However, as we include more physics, further criteria are required to be fulfilled before we can be confident of similarity between two systems. Nevertheless, this is not impossible, and is regularly done in

---

[‡] Caveat: not including extreme conditions where quantum and/or relativistic effects become important.

current laboratory astrophysics experiments. The ideal case is described in chapter 2, and expanded to more complicated cases in chapter 3.

1.5 Astrophysical Events

We might ask ourselves what the point is of going to all the effort of designing, and performing, an experiment on a laser system, when we can just use observational data and simulations. Notwithstanding the argument given above – relating to the long timescales of astrophysical events – there are some cases where a laboratory experiment allows us to investigate something that cannot be observed directly.

One such example would be that of material that passes between two stars. The majority of solar-type stars are thought to belong to binary star systems (22), in which two stars are sufficiently close to one another that they orbit around a common point (their centre of mass). In such cases the stars are likely to be of different types, and as their life cycles evolve it is common for material from one star to start moving onto the other. What happens next is determined by the nature of the stars themselves (i.e. how large they are, their mass etc.) but we are particularly interested in the case where one of the stars has a high mass, and strong magnetic field: a white dwarf. In this case, there is a strong gravitational pull from the white dwarf, which begins to pull plasma from the other star towards the white dwarf. However; as plasma is affected by magnetic fields, the stream of material is directed along the field lines of the white dwarf, much like a bar magnet moves iron filings. The material is thus directed onto the poles of the white dwarf, and accelerated towards the surface, where it impacts, and a shock wave is expected to form. Such an energetic event releases significant radiation, and this can be detected by telescopes in the form of X-rays. However, a white dwarf radius is rather small, in astrophysical terms, and the region of interest where the shock forms is only 1/10 th of the radius. In other words we can detect emission, but we cannot work out from which region of the star it has come because the resolution required is too great for modern telescopes. This is important, because the different theories put forward to explain this mass transfer predict different radiation signatures from different regions of the star.

In this case a laboratory experiment allows us to create a testable analogue to the astrophysical event. In the lab it is quite possible to resolve a feature 1/10 th of the scale of the target. This means we can mimic a particular method of mass transfer, and see what happens to the properties by probing them. We can then apply this understanding to the observational data from the telescopes to better characterise the star system. This would not be possible alone by just observing the star. More detail of this can be found in chapter 4.

1.6 Thesis Layout

Thus, this thesis is organised to address these points. Chapter 2 introduces the basic concepts of plasma physics and hydrodynamics, which are required to describe what is happening in space and in the laboratory, and shows how we can create the conditions to match the astrophysical case. Chapter 3 recalls the scaling of the fluid dynamic equations that shows that, if certain conditions are satisfied, the two systems will evolve similarly independent of their size. This is then expanded beyond the ideal case of the Euler Equations to include radiative, magnetic and quantum effects. This simplifed method is original work by the author, and also includes quantum effects for the first time, and satisfies the condition that the underlying physics is independent of the scale of the system.

Chapter 4 details the design, preparation, results and analysis of a laboratory experiment designed to simulate the astrophysical case of accretion between a late, main sequence star and a highly magnetised white dwarf. This experiment was part of a longer series of experiments from a collaboration between many universities, with this experiment primarily led by the author. This satisfies the requirement that we can actually design relevant experiments to aid understanding of astrophysical events in the laboratory. Finally, chapter 5 details how we can apply the effects of radiation, derived from the equations in chapter 3, to the structure factor by deriving this from radiative hydrodynamics. Theoretically the structure factor is important in relating the interaction between particles, and how this changes in time and thus is of importance in understanding dense plasma properties. The dynamic structure factor [DSF] is related experimentally to thompson scattering, and so the effect of radiation could change the diagnostic response. All points are drawn together in the conclusion in chapter 6.

Chapter 2

Background Theory

> *"...the Cabbage Research Institute, whose students were the first to get a cabbage to a height of five hundred yards propelled entirely by its own juices. Nobody asked why they felt it was necessary to do this, but that was science for you, and, of course, students."*
>
> – Terry Pratchett, *Raising Steam*

In this chapter the underlying assumptions and basis of plasma physics will be introduced. A description of single particle motion is given, before being expanded to the idea of plasma as a fluid, and the ideas of hydrodynamics. For the specific case of a plasma, magnetic effects are introduced to lead to the ideal magnetohydrodynamics equations. The chapter ends with a brief introduction to plasma physics in astrophysics, and which phenomena are of particular interest to study, thus giving the motivation for laboratory analogues of such events.

2.1 Plasma Physics

Beyond the more familiar terrestrial states of matter, the plasma state is the most common state of matter in the (visible) universe. Plasma is found in and around stars, in the interstellar medium, and, on earth, within fluorescent lighting and lightning. In simple terms a plasma is considered as an ionised gas, which gives it unique properties that set it apart from the other matter states. However; much like liquids and gases, plasma can be described in terms of fluid theory, which is discussed later.

It is from the ionised nature of a plasma that its unique properties derive. The ions and electrons are free to move separately, but an individual particle's movement is mediated by the local electromagnetic field which is itself dependent on the surrounding ions and electrons. This free, but related, motion leads to the properties of *quasi-neutrality* and *collective effects.* As the electrons and ions can move, any charge imbalance that is formed will cause a movement of nearby particles such that, overall, neutrality is restored. Such a charge imbalance can result from the random thermal motion of the particles. This also gives rise to the collective effects: movement of one particle will cause others to react.

There is some lower limit over which these effects are seen. We quantify this by considering the *Debye length,* λ_D, which defines the distance past which particles shield each other from charge imbalances, and quasi-neutrality holds:

$$\lambda_D = \left[\frac{e^2}{\varepsilon_0 k_B} \left(\frac{n_e}{T_e} + \sum_i \frac{Z_i n_i}{T_i} \right) \right]^{-1/2} \tag{2.1}$$

where e is the electronic charge, k_B Boltzmann's constant, ε_0 vacuum permittivity, n_j the number density and T_j the temperature, of the electrons or ions, subscript e or i respectively, and Z_i is the charge state of the ions. As the ions are much heavier than the electrons, we normally work in the approximation that the ion movement can be neglected compared to the electrons and this leads to the electronic Debye length:

$$\lambda_D = \sqrt{\frac{\varepsilon_0 k_B T_e}{e^2 n_e}}. \tag{2.2}$$

To see how this affects the properties of charged particle interactions, we can compare how the potential of a charged particle differs in a plasma to that felt in a vacuum. For a vacuum, the potential, ϕ_C (Coulomb potential), of a point charge, q, at a distance, r, from the charge is simply defined as:

$$\phi_C = \frac{q}{4\pi\varepsilon_0 r} \tag{2.3}$$

which gives us the standard 1/r dependence of an electric field.

We now consider that the point charge is placed into a plasma, where the ions and electrons are in thermal equilibrium, and thus follow a Boltzmann distribution. We define the charge density, ρ_e, as:

$$\rho_e = e\left(n_i - n_e\right) \tag{2.4}$$

and the distributions of ions and electrons as:

$$n_e = n_0 \exp\left(\frac{e\phi}{k_B T}\right), \quad n_i = n_0 \exp\left(-\frac{e\phi}{k_B T}\right) \tag{2.5}$$

where n_0 is the equilibrium particle number density.

Using Poisson's equation, $\nabla^2\phi = -\rho_e/\varepsilon_0$, and the assumption that the thermal kinetic energy is much larger than the electrostatic energy (i.e. distances greater than the Debye length), we can solve to give the potential:

$$\phi = \frac{q}{4\pi\varepsilon_0 r} \exp\left(-\frac{\sqrt{2}r}{\lambda_D}\right) \tag{2.6}$$

and it is obvious that the potential drops off far quicker - exponentially - in a plasma than in a vacuum, at distances greater than the Debye length. This effect is called *Debye Shielding*. However to be a well behaved plasma, the number of particles that are screening the charge needs to be large: otherwise the screening of the charge is not isotropic. Thus it is useful to determine the number of particles, N_D, in the *Debye sphere*, defined as a sphere with radius of the Debye length centred on the charge q:

$$N_D = \frac{4\pi}{3}\lambda_D^3 n_0. \tag{2.7}$$

To be effectively shielded $N_D >> 1$, or $\lambda_D >> n_0^{-1/3}$. Thus we can determine a length scale over which the plasma is 'well behaved' (23):

$$n_0^{-1/3} << \lambda_D << \ell \tag{2.8}$$

where ℓ is the characteristic length scale of the system. This equation effectively says that the Debye length much be large enough that it encompasses enough particles to allow for isotropic screening, but is smaller than the length scale we are interested in observing, such that collective behaviour and quasi-neutrality apply over that scale.

When describing a plasma, and of similar importance to the Debye length, the *Plasma frequency* is also used to describe a plasma's properties. A movement of electrons will cause a separation of charge locally within the plasma: creating an electric field that acts to restore charge neutrality. From the equation of motion of a charged particle in an electric field, we can thus define this oscillation frequency as:

$$\omega_{pe} = \sqrt{\frac{n_0 e^2}{m_e \varepsilon_0}}. \tag{2.9}$$

which is the *electron* plasma frequency, where m_e is the electron mass. (Again, we have assumed that the ions are stationary over the timescales of electron movement.)

2.2 Plasma Equation of Motion

2.2.1 Kinetic Theory

When considering plasmas we are primarily interested in their movement. The simplest description thus starts with consideration of single particle motion, giving the equation of motion (from Newton's Second Law):

$$m_j \frac{d\boldsymbol{v}_j}{dt} = q_j \left(\boldsymbol{E} + \boldsymbol{v}_j \times \boldsymbol{B} \right) \tag{2.10}$$

which describes the motion of a charged particle in an externally applied electromagnetic field. The standard Lorentz force is recognisable on the right hand side of the equation – where $\boldsymbol{E}$ is electric field and $\boldsymbol{B}$ is magnetic field – $\boldsymbol{v}_j$ is the particle velocity, and subscript j is either for electrons, e, or ions, i.

However this description is somewhat problematic practically. This formalism requires us to separately calculate the forces on, and movement of, each individual particle. Given that one of the criteria of a well-behaved plasma is a large number of screening particles, this can quickly become unwieldy, and, in the case of simulations, far too computationally expensive. Separately, the Lorentz force as depicted here is not exact as it fails to take account of the generation of fields by the particle itself as it moves, thus altering the overall force.

Instead a kinetic description can be used, in which distributions of particles are considered. If we consider Boltzmann distributions of particles, again in an externally applied electromagnetic field, we can write the equation of motion as:

$$\frac{\partial f_j}{\partial t} + \boldsymbol{v}_j \cdot \nabla f_j + \frac{q_j}{m_j} \left(\boldsymbol{E} + \boldsymbol{v}_j \times \boldsymbol{B} \right) \cdot \frac{\partial f_j}{\partial \boldsymbol{v}_j} = 0 \tag{2.11}$$

where f_j is a function that includes the variation of the number density in space and time, and the velocity distribution in each direction, $f_j(\boldsymbol{r}, \boldsymbol{u}, t)$. This is known as the *Vlasov Equation*(24) and is valid for hot (i.e. thermal energy > electric potential), non-relativistic plasmas where collisions can be neglected.

This form of the equation of motion simplifies the single particle case, and allows us to calculate movement for much larger systems. However, in many problems in plasma physics, we do not need to know what is happening to individual particles, or distributions of the particles, but rather we can consider the entire plasma as a fluid and instead follow what happens to fluid elements. This is a much larger simplification than the kinetic approach but it can explain many features of plasma physics.

2.2.2 Fluid Theory

Instead of considering particles, we can consider the plasma to be a fluid which is made up of fluid elements. There exist many fluid descriptions of plasmas, but we shall start with the simplest *single fluid* form which treats the whole plasma as one fluid. The velocity distributions are considered only as a Maxwellian distribution and thus can be defined by a single temperature, rather than explicitly defined as in the Vlasov equation.

2.2.2.1 Continuity Equation

We start by considering a volume of fluid containing a certain mass. The rate of mass flowing through the surface bounding this volume is the surface integral of the density, ρ, and flow velocity, $\boldsymbol{u}$. Using the divergence theorem, and requiring that this be true for any volume, we have:

$$\frac{\partial \rho}{\partial t} + \nabla \cdot (\rho \boldsymbol{u}) = 0. \tag{2.12}$$

This is the *Continuity Equation* and details the conservation of mass within a system. Simply, the change of mass of a fluid element is only dependent on the mass flow into or out of that element. If there were sources, or sinks, of mass then these would appear on the right hand side of equation (2.12).

2.2.2.2 Momentum Equation

Again considering a volume of fluid, the total force acting over the surface of such an element is related to the pressure, p. Using the divergence theorem, and Newton's second law of motion, we have:

$$\rho \frac{D\boldsymbol{u}}{Dt} = -\nabla p. \tag{2.13}$$

This is the *Momentum Equation*, which details the conservation of momentum within a system. Equation 2.13 only includes pressure as a source term, as we are only considering a simple fluid. However, many other terms are important, especially in the case of a plasma, and these will be discussed in later sections.

In equation (2.13) the formalism of a the material derivative is introduced:

$$\frac{D}{Dt} = \left\{ \frac{\partial}{\partial t} + \boldsymbol{u} \cdot \nabla \right\}. \tag{2.14}$$

This is no longer just telling us about how a property varies in time at the position of the particle, but rather how the property changes for a *fluid element* (24). Thus we now consider how the property changes at a fixed point in space, the first term on the right hand side of equation (2.14), but also how a property changes as we move in the frame of the fluid from one region to another, the last term in equation (2.14).

2.2.2.3 Energy Equation

We begin by considering the rate of change of energy of a volume of fluid in time. The internal energy and kinetic energies are treated separately. We make use of the thermodynamic relation $d\epsilon = Td\mathcal{S} - (p/\rho^2)d\rho$ – where ϵ is the internal energy per unit mass, $\mathcal{S}$ is the entropy per unit mass and T is the temperature – , the adiabatic relation $D\mathcal{S}/Dt = 0$ and continuity equation (equation (2.12)) to give:

$$\frac{\partial}{\partial t}\left(\rho\epsilon + \frac{1}{2}\rho u^2\right) = -\nabla\cdot\left[\rho\boldsymbol{u}\left(\frac{u^2}{2}+\epsilon\right)+p\boldsymbol{u}\right]. \tag{2.15}$$

This is the conservative form* of the *Energy Equation* which details the conservation of energy within a system. As with the Momentum equation, equation (2.13), this equation only includes pressure as a source term for energy, whereas many more are important in more complicated systems.

Together equations (2.12), (2.13), (2.15) form the *Euler Equations* of hydrodynamics. (The form of the energy equation, equation (2.15), here is written in a way that is easier to work with practically. It can also be written in a form that is more similar to the other two equations as: $Dp/Dt = -\gamma p\nabla\cdot\boldsymbol{u}$ where γ is the adiabatic index.)

2.3 Magnetohydrodynamics and beyond

In the previous section it was stated that a plasma can be described as a fluid, and then we showed the equations of motion for a fluid system. However, as a plasma contains charged particles, the equations in the previous section need to be expanded before we can use them to describe plasma motion.

The continuity and energy equations remains unchanged, equation (2.12) &(2.15), but the Momentum equation (2.13), requires addition of a magnetic term:

$$\rho\frac{D\boldsymbol{u}}{Dt} = -\nabla p + \boldsymbol{J}\times\boldsymbol{B}, \tag{2.16}$$

---

* By conservative form here we follow the definition in Drake (25), where the change in density of a quantity is determined by the flux of that quantity and the net volumetric sources, or sinks, of that quantity.

where $\boldsymbol{J}$ is the current density.

This is the fluid extension of the kinetic equation (2.10). However; as the fluid element exhibits the 'quasi-neutrality' property of a plasma, the electric term is neglected.

2.3.1 Ideal Magnetohydrodynamics

With this modification, we acquire the *Ideal MHD Equations*, in Eulerian form:

$$\frac{\partial \rho}{\partial t} + \nabla \cdot (\rho \boldsymbol{u}) = 0, \tag{2.17a}$$

$$\rho \frac{D\boldsymbol{u}}{Dt} = -\nabla p + \boldsymbol{J} \times \boldsymbol{B}, \tag{2.17b}$$

$$\frac{Dp}{Dt} = -\gamma p \nabla \cdot \boldsymbol{u}, \tag{2.17c}$$

which correspond to the fluid description of the plasma. However we need to close the system using Maxwell's equations:

$$\frac{\partial \boldsymbol{B}}{\partial t} = \nabla \times (\boldsymbol{u} \times \boldsymbol{B}), \tag{2.17d}$$

$$\boldsymbol{J} = \frac{1}{\mu_0} \nabla \times \boldsymbol{B}. \tag{2.17e}$$

Where equation (2.17d) is the Maxwell-Faraday Equation, with the substitution of $\boldsymbol{E}$ from the expression of the ideal, generalised Ohm's Law:

$$\nabla \times \boldsymbol{E} = -\frac{\partial \boldsymbol{B}}{\partial t}, \quad \boldsymbol{E} = -\boldsymbol{u} \times \boldsymbol{B}.$$

Equation (2.17e) comes from Ampère's Law, neglecting displacement current. The neglection of displacement current, from the approximation of quasi-neutrality – which was also used to neglect the electric term in the Lorentz force in equation (2.13) – also introduces the concept of low frequency/velocity within the system. Naturally this means the Ideal MHD equations are non-relativistic.

The approximations required for the Ideal MHD equations to be valid are as follows:

1. Velocities are non-relativistic – to be consistent with quasi-neutrality,

2. Resistivity of the fluid is zero, i.e. the fluid is perfectly conducting,
3. Localisation of particles. This can occur as a result of collisions: when the ion mean free path is much smaller than the spatial scale, or magnetic fields: where magnetic entanglement or plasma microfluctuations cause the system to be localised along the field lines: requiring the ion gyroradius to be much smaller than the spatial scale (52).

The range over which ideal MHD is able to predict plasma behaviour is surprisingly large. Even in cases where not all the assumptions are adequately satisfied, the predictions from the ideal case are successful and qualitatively useful.

In these equations, we consider the plasma to act as one fluid, thus, we also assign a single temperature to the fluid. Generally strong coupling between the ions and electrons is seen when the collisionality between the two species is high, which results in both species having the same temperature – thus a single temperature fluid description is valid. This also assumes that radiation is not dominant, which is true in many systems with high density (25). However beyond the simple case it may be required to treat the plasma as two –electron and ion –, or three – electron, ion and radiation –, fluids each with distinct temperatures. In shocks, for example, the ion temperature will differ from the electron temperature as the shock directly heats the ions. However, if the system has a high degree of collisionality, the electron and ion temperatures will equilibrate quickly behind the shock front. If the shock wave is sufficiently radiative, then the radiation temperature can also differ from that of the ion and electrons directly ahead of the front: a so-called ‘radiative precursor’. More of this is discussed later, in chapter 4.

2.3.2 Resistive MHD

The Ideal MHD equations do not take into account many other effects that can be important in plasma evolution, such as heat conduction, fluid viscosity etc. However, arguably magnetic resistivity is the most frequent deviation from the ideal case that could otherwise be explained fully by the above equations. As stated in the approximations of ideal MHD, we assume that the fluid is perfectly conducting. In such a case magnetic field lines are ‘frozen into’ the plasma and thus move with the fluid. In many astrophysical cases, such as sun spots and coronal ejections (26) (where magnetic diffusivity also allows for magnetic reconnection), the finite diffusivity of the plasma means that, while a magnetic field can diffuse out of the plasma, the time that it would take for this to happen is far longer than the time scale of the phenomenon we are interested in. However, in the lab, it can very easily be the case that the diffusion time is of the order of the experiment timescale. We must be aware of this and either design the experiment so that the diffusion time is much greater, or include additional terms into the ideal equations to take into account the effect of resistivity.

To take resistivity into account we have to modify equation (2.17d) as Ohm's Law is now written as $\boldsymbol{E} + \boldsymbol{u} \times \boldsymbol{B} = \rho_E \boldsymbol{J}$ (where ρ_E is the electrical resistivity):

$$\frac{\partial \boldsymbol{B}}{\partial t} = \nabla \times (\boldsymbol{u} \times \boldsymbol{B}) - \nabla \times (\eta \nabla \times \boldsymbol{B}), \tag{2.18}$$

where η ($= \rho_E/\mu_0$) is the magnetic diffusivity.[†]

In equation (2.18) the first term on the right hand side represents advection of the magnetic field with the plasma, whereas the second term represents the diffusion of the magnetic field through the plasma. The ratio of these terms is given by the *Magnetic Reynolds Number*:

$$Re_M = \frac{u_0 \ell_0}{\eta}, \tag{2.19}$$

where u_0 and ℓ_0 are characteristic values of the fluid velocity and length scale of the system respectively. Thus if the Magnetic Reynolds number in a system is sufficiently large, advection outweighs diffusion, and the ideal equations are recovered. Such *characteristic ratios* detail the relative importance of different effects within a system and thus are of great importance when considering scaling between laboratory experiments and astrophysical events. They can be derived by *dimensional analysis* of the fluid equations, as will be done in the following section.

2.4 Scaling

The ultimate aim of laboratory astrophysics is to provide useful insight into cosmic events using small scale experiments on earth. The crux of this approach therefore relies on there existing a connection between small scale, and large scale, events. This can be achieved by rewriting the MHD equations in a dimensionless form which also generates characteristic ratios, much like the Magnetic Reynolds number above. This approach is well known in engineering with standard fluid mechanics, where it is used to determine similarity between flows (27), or to scale between prototypes (28).

[†] If the diffusivity is constant we can write this as: $\frac{\partial \boldsymbol{B}}{\partial t} = \nabla \times (\boldsymbol{u} \times \boldsymbol{B}) + \eta \nabla^2 \boldsymbol{B}$.

2.4.1 Ideal Case

We begin by considering the ideal MHD equations (2.17) (with the form of the energy equation as in equation(2.15)). These equations contain variables for density, fluid velocity, and so on, which are functions that vary in time and space, and have an associated dimension associated with them. For example, ρ is the mass density of the system, usually written in terms of g/cc, which will vary in time and space, as related by the Continuity equation (2.17a). However each variable can be rewritten in terms of a *characteristic value*, which contains the dimension of the property, and a *dimensionless function* that describes how that value changes in time and space. This separates the dimension of a property from its evolution in time and space.

Thus the fluid velocity, position, time and density are written as:

$$\boldsymbol{u} \to u_0 \boldsymbol{u}^*, \quad \boldsymbol{r} \to \ell_0 \boldsymbol{r}^*, \quad t \to \frac{\ell_0}{u_0} t^*, \quad \rho \to \rho_0 \rho^*, \tag{2.20}$$

where u_0, ℓ_0, and ρ_0 are the characteristic fluid velocity, length, and density of the system, respectively. From now on we will use the convention that *starred quantities* (*i.e.* $\boldsymbol{u}^*$) are dimensionless, while *quantities with subscript 0* (*i.e.* u_0) correspond to a characteristic value for that variable.

The above assumptions imply :

$$\frac{\partial}{\partial t} \to \frac{u_0}{\ell_0} \frac{\partial}{\partial t^*}, \quad \nabla \to \frac{\nabla^*}{\ell_0}. \tag{2.21}$$

Similarly, we can set

$$p \to p_0 p^*, \quad \boldsymbol{B} \to B_0 \boldsymbol{B}^*, \quad \epsilon \to \epsilon_0 \epsilon^*.$$

However, the choice of the values for p_0, B_0, and ϵ_0 is not arbitrary. We will see below that these characteristic values are defined as functions of the density and fluid velocity, to keep the equations scale invariant.

Starting with equation (2.17a), we replace the variables with those given above:

$$\frac{\rho_0 u_0}{\ell_0} \frac{\partial \rho^*}{\partial t^*} + \frac{\rho_0 u_0}{\ell_0} \nabla^* \cdot (\rho^* \boldsymbol{u}^*) = 0,$$

and we can divide through by the common factor of $\rho_0 u_0 / \ell_0$, leaving:

$$\frac{\partial \rho^*}{\partial t^*} + \nabla^* \cdot (\rho^* \boldsymbol{u}^*) = 0, \tag{2.22a}$$

which has the same form as equation (2.17a) except now there is no inherent dependence on scale, as all the variables are dimensionless.

The same process can be applied to the Momentum, (2.17b), and Energy, (2.17c), equations:

$$\rho^* \left(\frac{\partial \boldsymbol{u}^*}{\partial t^*} + \boldsymbol{u}^* \cdot \nabla^* \boldsymbol{u}^* \right) = -\frac{p_0}{\rho_0 u_0^2} \nabla^* p^* + \frac{B_0^2}{\mu_0 \rho_0 u_0^2} \left[(\boldsymbol{B}^* \cdot \nabla^*) \boldsymbol{B}^* - \nabla^* \frac{B^{*2}}{2} \right],$$

here we have divided through by a common factor of $\rho_0 u_0^2/\ell_0$, and used the relation $\boldsymbol{J} \times \boldsymbol{B} = (\boldsymbol{B} \cdot \nabla)\boldsymbol{B}/\mu_0 - \nabla(B^2/2\mu_0)$ which follows from equation (2.17e), valid in the ideal case. Here the first term represents the *magnetic tension* and the second the *magnetic pressure* of the system. As we require this to be invariant in the same manner as equation (2.22a), we define $p_0 = \rho_0 u_0^2$, which corresponds to the material, or ram, pressure of the system; and $B_0^2 = \mu_0 \rho_0 u_0^2$. Written in this way, the reference magnetic field has a value such that the fluid velocity and the Alfvén velocity (29) are the same. Substituting these into the above equation gives us the dimensionless form of equation (2.17b):

$$\rho^* \left(\frac{\partial \boldsymbol{u}^*}{\partial t^*} + \boldsymbol{u}^* \cdot \nabla^* \boldsymbol{u}^* \right) = -\nabla^* p^* + \left[(\boldsymbol{B}^* \cdot \nabla^*) \boldsymbol{B}^* - \nabla^* \frac{B^{*2}}{2} \right],. \tag{2.22b}$$

For the Energy equation:

$$\frac{\partial}{\partial t^*} \left(\frac{\epsilon_0}{u_0^2} \rho^* \epsilon^* + \frac{\rho^* u^{*2}}{2} + \frac{B_0^2}{\mu_0 \rho_0 u_0^2} \frac{B^{*2}}{2} \right) = -\nabla^* \cdot \left[\rho^* \boldsymbol{u}^* \left(\frac{\epsilon_0}{u_0^2} \epsilon^* + \frac{u^{*2}}{2} \right) + p^* \boldsymbol{u}^* \frac{E_0 B_0}{\mu_0 \rho_0 u_0^3} \boldsymbol{E} \times \boldsymbol{B} \right],$$

where we have divided through by a common factor of $\rho_0 u_0^3/\ell_0$. As we did to generate equation (2.22b), we define the characteristic internal energy per unit mass to be $\epsilon_0 = u_0^2$ to make the equation invariant to scale, and take the value of B_0 as defined above (also using that $E_0/B_0 \sim u_0$ from Ideal Ohm's Law) and we acquire the dimensionless form of equation (2.15):

$$\frac{\partial}{\partial t^*} \left(\rho^* \epsilon^* + \frac{\rho^* u^{*2}}{2} + \frac{B^{*2}}{2} \right) = -\nabla^* \cdot \left[\rho^* \boldsymbol{u}^* \left(\epsilon^* + \frac{u^{*2}}{2} \right) + p^* \boldsymbol{u}^* + \boldsymbol{E}^* \times \boldsymbol{B}^* \right]. \tag{2.22c}$$

Following the same process, the Induction Equation, (2.17d), becomes:

$$\frac{\partial \boldsymbol{B}^*}{\partial t^*} = \nabla^* \times (\boldsymbol{u}^* \times \boldsymbol{B}^*) \tag{2.22d}$$

where we have divided through by a common factor of $u_0^2\sqrt{\mu_0 \rho_0}$ $(= B_0 u_0/\ell_0)$. Thus we have shown that equations (2.17) can be written in a scale invariant form in the idea case, equations (2.22a)-(2.22d). This implies that we can relate systems of different scales if both cases follow ideal MHD, which provides a link between astrophysical events and laboratory experiments.

2.4.2 Non-Ideal Cases

However, as was touched on in section 2.3.2, real phenomena cannot always be described with ideal MHD. If we include other terms in the equations of motion, how does this affect the scaling? To illustrate this we perform the same process on the resistive MHD induction equation, (2.18):

$$\frac{\partial \boldsymbol{B}^*}{\partial t^*} = \nabla^* \times (\boldsymbol{u}^* \times \boldsymbol{B}^*) - \frac{\eta_0}{u_0 \ell_0} \nabla^* \times (\eta^* \nabla^* \times \boldsymbol{B}^*) , \tag{2.23}$$

$$\frac{1}{Re_M} = \frac{\eta_0}{u_0 \ell_0}$$

We can see that we recover the scale invariant portion of the ideal MHD Induction equation, (2.22d), but the final term, relating to magnetic diffusion, is modified by a constant term. In fact, we can recognise this as the reciprocal of the Magnetic Reynolds number, (2.19). Such values are important when considering non-ideal fluid dynamics as they tell us about the relative importance of competing effects that affect the plasma dynamics (in this case, the ratio between magnetic field advection with the fluid, and magnetic field diffusion through the fluid.)

Here the magnetic diffusion term still depends on parameters of the system and thus it is not so easy to draw a parallel between a small-scale lab experiment and an astrophysical event. However, this can be remedied in one of two ways:

1. If we exactly match the value of the multiplying constant on the non-ideal term in both cases then the equations are once again equivalent. In this case we would require:

   $$[Re_M]_{lab} \equiv [Re_M]_{astro} ,$$

2. If we consider that the magnitude of each term in the equation is similar, then by making the multiplicative constant small, this term can be neglected. In this case, if Re_M is very large then

   $$1 + \frac{1}{Re_M} \approx 1$$

   and we recover the original, scale invariant case.

These two methods allow for a comparison, but by different routes. In the first case the two systems have the same value of the multiplicative constant, and thus exhibit exactly the same behaviour, relevant for that term. The difficulty in this case is that it can be very hard to design an experiment that can exactly replicate the value needed to simulate an astrophysical event. The benefit is that this places no restrictions on the initial value of the constant: as long as they are equal the constant can be very large or very small, or anywhere in-between, thus allowing for different physical meanings.

The second case uses an approximation that considers a term to become unimportant in affecting the overall dynamics if its multiplicative constant is very small. We recall that the magnetic Reynolds number is a ratio of the relative strength of advective and diffusive effects on a magnetic field. If this number is large, advective effects are more important than magnetic diffusion. This then returns the form of the equations to the ideal case: the non-ideal term is neglected. However this does require that numbers, such as the magnetic Reynolds number, are sufficiently large in both systems we are interested in. Fortunately astrophysics is on our side: in many astrophysical events (such as supernova explosions (30)) the magnetic Reynolds number is sufficiently large, $\sim 10^{20}$, that we can ignore diffusion. The difficulty in this case is achieving a sufficiently large magnetic Reynolds number in the lab.

These two cases relate to two different types of *similarity relation* between systems of different scales. As defined by Falize et al. (31), the first case is the *absolute similarity concept* (32) where we rescale physical quantities, but the equations are the same. The second case is the *global similarity concept* (32) where only the form of the equation is invariant, not all of the properties (i.e. as the magnetic Reynolds number differs, so too do the resistivity, scale lengths etc.) Global similarity is less constraining than absolute similarity, but requires more careful justification when attempting to compare two systems. A hierarchy of similarity relations, which we will not go further into here, is found in Falize et. al (2011) (31). [‡]

In this section we have only gone beyond the ideal case by including the effect of resistivity in the induction equation. The underlying fluid equations can, however, be modified to include many other effects, such as as radiation, and these can then be scaled to generate other characteristic ratios. This will be considered in the following chapter 3.

2.5 Shocks

The previous sections have shown that we can describe a plasma using a variety of methods, and that, in the case of fluid theory, we can apply understanding from

---

[‡] Evidently the best similarity relation involves an exact reconstruction of the system of interest. There are some logistical problems with this when considering astrophysical events...

one scale to another by relating the two cases with the scale invariant form of the equations of motion. This is a useful, and necessary, description, but now we turn to describing some of the dynamics that can occur in plasmas that we are interested in studying.

When a plasma moves we can observe standard flow not unlike water flowing down a stream, or air being heated and expanding above a flame. However, it is the cases that lead to more extreme behaviour that are the most interesting, for example weather systems caused by turbulent air flow. Of particular interest in plasma physics, not least because of its ubiquity in astrophysics, is the *shock wave.* Indeed, shocks are an important part of a subset plasma physics which is defined as *High-Energy-Density Physics*, [HEDP]. Such environments may have densities around solid density, or above, and/or temperatures up to hundreds of eV: in short, the conditions you would expect in a supernova explosion (30), or a inertial fusion experiment on earth (33).

2.5.1 Formation of a shock wave

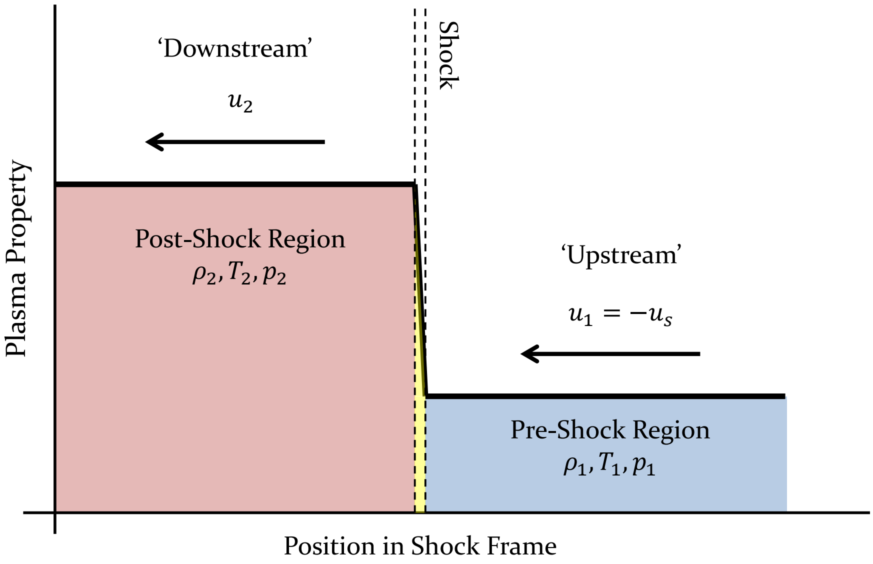

Figure 2.1: An example of how a shock affects fluid properties, adapted from Drake (25). The shock velocity, $\boldsymbol{u}_s$, is the speed at which the incoming flow meets the shock, here defined as $\boldsymbol{u}_s = -\boldsymbol{u}_1$.

A *shock* is defined as a sudden change in fluid properties across a narrow transition region. As can be seen in figure 2.1, the density and temperature jump across a shock front such that the pre- and post-shock regions have quite different properties. Any sudden introduction of energy into a system, such as a laser pulse, can cause a shock wave.

Shocks can be described as a 'hydrodynamic surprise' because they do not give warning to the fluid ahead of themselves, 'upstream', as they travel faster than the sound speed in this, unshocked, material. Generally materials dissipate energy by forming sound waves; but the amount of pressure that can be sustained is limited by the sound speed, an inherent property of the material (25). If more energy is given to the fluid than can reasonably be dissipated by sound waves, then a shock is formed instead.

2.5.2 Jump conditions

As figure 2.1 shows, the properties on either side of a shock can vary quite considerably. However both sides of the shock front still have to obey the laws of conservation of mass, momentum and energy. Thus we can derive jump conditions that link the properties on either side of a shock front.

Starting from the hydrodynamic equations of motion for a fluid, equations (2.12), (2.13) & (2.15) we consider a plane parallel, steady-state disturbance (i.e. only consider the x-direction, and $\partial/\partial t = 0$.) Thus we can write:

$$\frac{\partial}{\partial x}(\rho \boldsymbol{u}) = 0, \tag{2.24a}$$

$$\rho \boldsymbol{u} \frac{\partial}{\partial x} \boldsymbol{u} = -\frac{\partial}{\partial x} p, \tag{2.24b}$$

$$-\frac{\partial}{\partial x}\left(\rho \boldsymbol{u}\left(\frac{u^2}{2} + \epsilon\right) + p\boldsymbol{u}\right) = 0. \tag{2.24c}$$

Integrating across the discontinuity, where $x_1 < x_s < x_2$ where x_s is the shock position, subscript 1,2 referring to pre- and post- shock properties respectively, gives:

$$[\rho \boldsymbol{u}]_{x_1}^{x_2} = 0 \quad \rightarrow \quad \rho_1 \boldsymbol{u}_1 = \rho_2 \boldsymbol{u}_2, \tag{2.25a}$$

$$\left[\rho \boldsymbol{u}^2 + p\right]_{x_1}^{x_2} = 0 \quad \rightarrow \quad \rho_1 \boldsymbol{u}_1^2 + p_1 = \rho_2 \boldsymbol{u}_2^2 + p_2, \tag{2.25b}$$

$$\left[\rho \boldsymbol{u}\left(\frac{1}{2}\boldsymbol{u}^2+\epsilon\right)+p\boldsymbol{u}\right]_{x_1}^{x_2}=0 \rightarrow \rho_1\boldsymbol{u}_1\left(\frac{1}{2}\boldsymbol{u}_1^2+\epsilon_1\right)+p_1\boldsymbol{u}_1=\rho_2\boldsymbol{u}_2\left(\frac{1}{2}\boldsymbol{u}_2^2+\epsilon_2\right)+p_2\boldsymbol{u}_2, \tag{2.25c}$$

where we have used $\frac{\partial}{\partial x}(\rho \boldsymbol{u}^2) = \rho \boldsymbol{u}\frac{\partial \boldsymbol{u}}{\partial x}$, and required that $\rho \boldsymbol{u} \neq 0$. Under these assumptions the shock width is infinitesimally narrow: in reality this is not true and the width is affected by a number of other factors, including viscosity and radiation. However these effects generally only become important at, or near, the shock front and thus these equations, (2.25), are valid as long as we look at the shocked and unshocked regions far from the shock front.

2.5.3 Density Ratios

From the jump conditions we can relate properties before and after the shock. It is useful to rearrange the jump condition equations and extract ratios of properties that can be experimentally measured. Of particular use is the density ratio, sometimes called the compression ratio η, from which information can be drawn relating to the importance of non-ideal terms, such as radiation, in the fluid dynamics. We will consider only the hydrodynamic case here, but this will be expanded to include radiation in a later chapter.

Starting from equations (2.25), and using the equation of state for a polytropic gas to close the system (that is $\rho\epsilon = p/(\gamma - 1)$, we can write the density ratio as:

$$\frac{\rho_2}{\rho_1} = \frac{p_2(\gamma_2+1)+p_1(\gamma_2-1)}{p_1(\gamma_1+1)+p_2(\gamma_1-1)}\frac{(\gamma_1-1)}{(\gamma_2-1)}.$$

In the limit that $p_2 >> p_1$, which we call a *strong shock*, this expression simplifies to:

$$\frac{\rho_2}{\rho_1} = \frac{(\gamma_2+1)}{(\gamma_2-1)} \tag{2.26}$$

which states that the density ratio tends to a set value, and that it is only dependent on the post-shock polytropic index. Equation (2.26) is the source of the claim that the strong shock compression ratio limit is four. This is true for a material with $\gamma = 5/3$, but this maximum value can vary quite considerably for different values of γ, which itself can be dependent on other properties of the system, such as ionisation and radiation.

We quantitatively determine a strong shock by use of the *upstream Mach Number*. This is again a characteristic ratio, which relates the upstream velocity to the sound speed:

$$M_u = \frac{\boldsymbol{u}_1}{c_{s1}} = \left(\frac{\rho_1 \boldsymbol{u}^2}{\gamma_1 p_1}\right)^{1/2} \tag{2.27}$$

where $c_{s1} = (\gamma_1 p_1/\rho_1)^{1/2}$ is the sound speed in the upstream, unshocked material. The alternative form of the Mach number shows that it also relates the ram pressure, $\rho_1 \boldsymbol{u}^2$, to the thermal pressure.

If M_u is large, then we define the shock to be *strong*.

2.6 Radiative Effects

Up until this point, we have only considered equations that describe a fluid, *hydrodynamics*, the ideal case for a plasma, *ideal MHD*, or with some magnetic resistivity effects, *resistive MHD*. Of course it is rarely the case that conditions can be described just using these forms of the equations, especially when considering many astrophysical phenomena. There are a wide range of cosmic events which laboratory experiments can help illuminate, but these straddle a large range of parameters. The interaction of the solar wind with the earth's magnetic field, (34), involves low density plasma which is highly mediated by magnetic effects. At the other end of the parameter space, supernovae explosions are high density, strongly radiative events (30), where radiation plays an important role in the evolution of the system.

We previously touched upon resistive magnetic effects, but we will now also briefly consider the effect of radiation. Generally when considering radiation we use the *optical depth* of the plasma to determine how the equations of motion need to be modified. Optical depth is a measure of how far radiation can propagate within a medium, which is related to the medium's *opacity*. Opacity can be a complicated function of density, temperature, ionisation state etc. in which much work has been done (35), and it is very much still a current area of research (36). Optical depth and opacity are related in equation (2.28) (from (37)) below:

$$I(\nu) = I_0(\nu)\exp(-\tau(\nu)); \quad \tau(\nu) = \kappa(\nu)\rho x \tag{2.28}$$

where I is the transmitted intensity of photons through a plasma, I_0 the initial intensity, τ the optical depth, κ the opacity per unit mass, ρ the mass density and x the path length. The opacity and optical depth, and hence intensity of photons, are dependent on the frequency of the radiation, ν.

2.6.1 Mean Opacities

It would appear that we need to know the spectral distribution of the radiation in order to determine its opacity in the plasma of interest. However, this is normally rather difficult to calculate, and often unnecessary. If we can replace the opacity with a mean opacity that can give the correct value for the radiative properties, we reduce the complexity of the problem considerably. This is not generally possible, but can been done in specific cases. Below we follow the definitions given by Mihalas and Mihalas (38).

The *Rosseland mean opacity*, κ_R, can be used if we are interested in radiation playing the role of transporting energy within a fluid. By replacing the opacity with a single mean opacity we can find the correct value of the radiative energy transport. It requires the fluid to be in local thermal equilibirum [LTE] and in the equilibrium diffusion limit (where the temperature change is negligible over one mean free path of radiation (25)). As such, the Rosseland mean opacity is used to describe radiative effects within stellar interiors: which we define as an *optically thick* fluid. In general we define a fluid to be optically thick when it satisfies:

$$\ell_0 >> \lambda_R = \frac{1}{\rho\kappa_R} \tag{2.29}$$

where ℓ_0 is the characteristic scale of the system and λ_R is the Rosseland mean free path. The Rosseland mean is a harmonic mean which gives greater weight to the transparent regions of the spectrum.

Alternatively, the *Planck mean opacity*, κ_P, can be used when we are interested in correctly calculating the total energy emitted by the fluid. Again the fluid needs to be in LTE, such that the fluid is treated as a thermal source, but this does not give the correct flux in the diffusion limit. Thus this opacity is useful when considering radiation loss from the fluid, without transporting energy throughout the fluid. This we define as being an *optically thin* fluid: i.e. the radiation has minimal interaction with the fluid after being emitted. For a fluid to be optically thin we require:

$$\ell_0 << \lambda_P = \frac{1}{\rho\kappa_P} \tag{2.30}$$

where λ_P is the Planck mean free path.

2.6.2 Radiative Effects in Shocks

The equations of motion for a plasma will be modified in the presence of radiation, but the form of these equations depends upon whether the plasma in question is optically thick or thin to radiation. This will be covered in greater detail in chapter 3.

As part of the modification of the dynamics, radiation can also modify the effects of a shock. The effect of this is dependent on the surrounding environment, such as whether the plasma is optically thin or thick, but this can be quantified by various parameters, as defined by Michaut et al. (39) and adapted below. The parameters used are:

$$\chi \equiv \frac{t_{cool}}{\ell_0/u_0}, \tag{2.31a}$$

which is the ratio of the cooling timescale to the characteristic timescale. If $\chi >> 1$ then the shock is not radiative, but if $\chi << 1$ then radiative effects must be considered as radiative cooling dominates.

$$Bo \equiv \frac{(\rho_0\epsilon_0 + p_0)u_0}{\boldsymbol{F}_R f(\tau)} \tag{2.31b}$$

which is a modified version of the Boltzmann number: a ratio of the material energy flux to the radiative flux (effectively the competing forces of convection and radiation on the temperature). $\boldsymbol{F}_R$ is the radiative energy flux, and $f(\tau)$ is a ratio of the actual radiative flux to σT^4, where σ is the Stefan-Boltzmann constant, which takes into account the effect of optical depth, τ, and geometry.

$$R \equiv \frac{\rho_0\epsilon_0}{E_R g(\tau)} \tag{2.31c}$$

which is a modification of the Mihalas number, where E_R is the radiative energy density, and $g(\tau)$ is the ratio of the actual radiative energy density to black body radiation $4\sigma T^4/c$, where σ is the Stefan-Boltzmann constant and c the speed of light, again taking into account the effect of optical depth and geometry.

Using these parameters, we can determine the effect of radiation within a system. For example, a case commonly found in astrophysics, involves a radiating shock in an optically thin environment: where both the pre- and post-shocked material is optically thin. Thus they are characterised by $\chi << 1$ and radiation affects the system predominantly as a loss mechanism, rather than affecting the dynamics elsewhere. Michaut et al. (39) define the other radiative shock types to be:

1. *Optically thin* – as defined above,
2. *Hybrid Radiative Shocks*, $\chi << 1$ and $Bo << 1$ (also possible for $R << 1$) – where one side of the shock front is optically thick, and the other thin,
3. *Optically thick, flux dominated*, $\chi << 1$, $Bo << 1$ & $R >> 1$ – optically thick on both sides of the shock, low Mach number, radiative energy and pressure do not need to be included,
4. *Optically thick, radiation dominated*, $\chi << 1$, $Bo << 1$ & $R << 1$– optically thick on both sides of the shock, high Mach number, radiative energy and pressure are important in the shock structure and dynamics.

2.7 Dynamic Structure Factor

As well as performing experiments, and developing theories, to further understand astrophysical conditions, it is necessary to be able measure properties to determine whether predictions from our current understanding are correct. For many fluid cases experimentally measured properties are compared to values calculated directly from the fluid equations: i.e. density jump across a shock front.

In WDM regimes the dynamic structure factor [DSF] of a material is of use in characterising the system. It relates theoretically to the many-body correlations in time and space within the system (40), and furthermore it can be found experimentally by relation to X-ray Thomson Scattering (41), [XRTS]. Many thermodynamic properties can be defined in terms of the DSF, and therefore it is of interest to calculate and measure. Simply, the DSF tells us how the density in the material at one point in space and time affects the density at another point in space and time.

The Dynamic Structure Factor [DSF], $S(\boldsymbol{k}, \omega)$, is formally defined as (42):

$$S(\boldsymbol{k}, \omega) = \frac{1}{2\pi N} \int e^{i\omega t} \langle \rho(\boldsymbol{k}, t) \rho(-\boldsymbol{k}, 0) \rangle dt, \tag{2.32}$$

which gives the response of a material to density fluctuations $\rho(\boldsymbol{k}, t)$ of wavevector $\boldsymbol{k}$, frequency ω, where N is the total number of particles, and $\langle \cdots \rangle$ represents an ensemble (or thermal) average.

2.8 Astrophysical Relevance

We have previously stated that much of the visible universe is in a plasma state, and have shown that we can scale equations describing the dynamics between the lab and astrophysics. The previous section also defined an important feature of plasma physics: the shock wave. However; what is important to know when considering astrophysics, and in which areas can laboratory experiments be of use?

As briefly discussed in the introduction, chapter 1, the use of laboratory astrophysics has the advantage of on-demand experiments, and allows active probing of the system. As long as we can determine similarity between the equations of motion describing the laboratory and astrophysical plasmas, then we can improve our understanding at the large scale by performing small scale experiments. One caveat of such experiments is that we do not aim for replication of an astrophysical event. For example, when investigating the physics of supernovae explosions, the incentive is *not* to recreate a supernova explosion in the laboratory. In this case there are many properties inherent to the astrophysical case, such as the interplay between gravity and fusion reactions, which cannot be replicated in the laboratory. However, if we are interested in the case of core material transport via instabilities as a result of a supernova explosion (43), or the generation of magnetic field as a result of turbulent flow (44), it is possible to create conditions in the laboratory that show similarity with the astrophysical case. While the source of the plasma flow may be different in both cases, by matching the characteristic ratios, or form of the equations of motion, we have a similarity relation between the flows which allows us to make comparisons.

From understanding aspects of supernovae explosions (e.g. the radiative nature of supernova shocks (30; 45) and the importance of hydrodynamic instabilities in mixing of core and outer elements (13)) and remnants (17; 46), to the core structure of planets (47; 48), and source of magnetic field in the universe (21; 44), laser experiments have wide applications to astrophysics.

2.9 Summary

In this chapter, the basic theory required for the rest of the thesis was described. Plasma physics was introduced as well as a simple, single particle, equation of motion. While exact, this approach causes difficulties when considering the large number of charged particles within a plasma, and so first general fluid theory was shown, which was then expanded to take into account the charged particle nature of a plasma with the introduction of the ideal MHD equations. Despite being a relatively simple formalism – treating the plasma as a single fluid – this approach is surprisingly accurate for many descriptions of plasma dynamics.

Thinking beyond the ideal case, the idea of non-perfectly conducting fluid was introduced, which also introduced the concept of a characteristic ratio, the Magnetic Reynolds number, which relates the importance of different effects within the plasma. Next, by showing that the fluid equations can be written in a form that is independent of the scale of the system, we see that these characteristic ratios are also important when requiring similarity between a laboratory experiment and an astrophysical event. The idea of similarity is briefly discussed.

Beyond standard dynamics, the physics of shocks is introduced, and jump conditions derived for the simple, ideal case. The concept of radiation is introduced, the simplification of using mean opacities when considering its effect, and how radiation can modify shock properties.

As a means of characterising WDM, the dynamic structure factor is briefly introduced, and the relation to the experimentally measureable XRTS is mentioned.

Finally, astrophysical relevance was briefly discussed, defining the scope for similarity between the laboratory and astrophysics.

Many of these elements will be built upon in the following chapters.

CHAPTER 3

Scaling of Hydrodynamics

> *"Space is big. Really big. You just won't believe how vastly, hugely, mind-bogglingly big it is. I mean, you may think it's a long way down the road to the chemist, but that's just peanuts to space."*
>
> – Douglas Adams, *The Hitchhiker's Guide to the Galaxy*

IN this chapter the concepts of scaling will be extended from the ideal case introduced in chapter 2. The concept of similarity and previous work in the area will be discussed. We then write down a general form of the hydrodynamic equations, which considers radiation, magnetic effects, viscous effects, heat transfer and quantum effects together for the first time (1). This equation is then scaled and new characteristic ratios are defined. Examples of how this approach is useful in designing, or analysing, experiments is then shown.

3.1 Similarity Concepts

As previously discussed in the Background Theory chapter 2, when we try to draw parallels from a laboratory experiment to an astrophysical object, we refer to it as a *similarity* relation between the two systems. The simplest case is one where the laboratory experiment exactly reproduces the conditions of the astrophysical case. This would be the 'Perfect Similarity' case from Falize et. al (2011) (31), and it has been used to study equation of state of planetary interiors (49), as well as other compact objects (50; 51). However it is not always possible to reach the exact conditions which we are interested in, as the spatial, temporal and energy scales may be outside the range of what is currently reproducible in an experiment.

However a similarity relation between the laboratory and astrophysical systems exists if we can show that both evolve in a way that the governing equations are invariant under a scale transformation; this requires the corresponding spatial, density, pressure, time, and so on, values in one system to be mapped onto the other system by multiplicative constants. This similarity can be obtained via fluid equations (52), or even at the kinetic level (53; 54) under some conditions.

In the ideal case the exact same form of the equations is acquired, but for non-ideal extensions we find characteristic ratios that are dependent on the scale of the system. We then either need to match the values, or make the value large enough, that we can draw similarities between a laboratory experiment and astrophysics. In this chapter we focus on the magneto-hydrodynamics [MHD] similarity, and provide a general framework to include effects arising from finite resistivity, thermal conduction, radiation diffusion and quantum non-locality.

3.2 Previous Work

Fluid similarity has previously been discussed, quite extensively, by Ryutov et al. and Falize et al. (31; 52; 54; 55; 56; 57). On the other hand, only selected aspects of the full governing equations have been investigated in the previous work, *i.e.* viscous hydrodynamics (52), radiative effects (31; 56; 57), ideal MHD (55; 56), or collisionless shocks (54). In this chapter we bring together the different elements of the equations in a simple conceptual form for the first time. By rewriting these equations in a dimensionless form we derive a set of characteristic ratios containing the details of the microscopic properties of the fluid at a given scale. Values of these ratios tells us how important local properties are in determining the overall fluid motion.

3.3 Full Quantum-Magneto-Radiative Hydrodynamic Equations

We first write the full set of MHD equations in presence of heat conduction, radiation diffusion and quantum effects (25; 58; 59; 60). We assume the plasma is described by a single fluid, but with appropriate transport coefficients that are derived from kinetic theory (61).

3.3.1 Continuity Equation

The equation for the conservation of mass is given by:

$$\frac{\partial \rho}{\partial t} + \nabla \cdot \rho \boldsymbol{u} = 0, \tag{3.1a}$$

where ρ is the mass density, t the time and $\boldsymbol{u}$ the fluid velocity. As we do not generally have sources or sinks for mass, this equation stays the same in the ideal and non-ideal case.

3.3.2 Momentum Equation

The equation for conservation of momentum reads as:

$$\rho \left(\frac{\partial \boldsymbol{u}}{\partial t} + \boldsymbol{u} \cdot \nabla \boldsymbol{u} \right) = -\nabla p + \Phi_{Bohm} + \nabla \cdot \boldsymbol{\sigma}_{\nu} + \boldsymbol{F}_{EM} + f_{rad}, \tag{3.1b}$$

where p is the fluid (ram) pressure, Φ_{Bohm} the quantum Bohm potential, $\boldsymbol{\sigma}_v$ the stress tensor, $\boldsymbol{F}_{EM}$ electromagnetic volume forces (the interaction of charged particles and EM fields), and f_{rad} the volume force of radiation on matter. This equation shows that, in the most general case, the momentum associated to a fluid element can change not only by the inertial term and the pressure gradient – as seen in the ideal case in chapter 2 –, but also due to exchange effects (the Bohm potential contribution), magnetic effects, viscous drag, and radiative forces. Each one of these non-ideal terms will be discussed in detail in the following sections. We also note that in equation (3.1b) the radiation force on matter, f_{rad}, in its most general form, includes effects from absorption and scattering (62).

3.3.3 Energy Equation

The equation for conservation of energy is:

$$\begin{aligned} \frac{\partial}{\partial t} \left(\rho \epsilon + \frac{\rho u^2}{2} + E_R \right) + \nabla \cdot \left[\rho \boldsymbol{u} \left(\epsilon + \frac{u^2}{2} \right) + p \boldsymbol{u} \right] \\ = -\nabla \cdot \boldsymbol{H} - \boldsymbol{J} \cdot \boldsymbol{E} + \Phi_{Bohm} \cdot \boldsymbol{u} - f_{rad} \cdot \boldsymbol{u}, \end{aligned} \tag{3.1c}$$

where ϵ is the specific internal energy, E_R the energy density of the radiation field, $\boldsymbol{H}$ the energy flux from non-ideal terms, $\boldsymbol{J}$ the current density, and $\boldsymbol{E}$ the electric field. The non-ideal energy flux is:

$$\boldsymbol{H} = \boldsymbol{F}_R + (p_R + E_R) \boldsymbol{u} + \boldsymbol{q} - \boldsymbol{\sigma}_{\nu} \cdot \boldsymbol{u}. \tag{3.1d}$$

where $\boldsymbol{F}_R$ is the radiative energy flux, p_R is the radiation pressure and $\boldsymbol{q}$ the heat flux. Here, we have distinguished between the radiative enthalpy flux associated with the matter motion, $(E_R + p_R)\boldsymbol{u}$, and the radiative energy flux in the rest frame of the fluid, $\boldsymbol{F}_R$ (see discussion in (62)).[*]

Differently from previous work, the above equations correctly describe quantum effects, which become important for high density fluids (63) – when the number density reaches values $\gtrsim 10^{24}$ cm^{-3} – as in white dwarfs or neutron star matter, or at small scales. This means that Pauli blocking, tunnelling and wave packet spreading begin to exert an effective *quantum pressure* to the system (60). This approach follows from the fact that deterministic equations can be used to describe both single-particle and many-body distribution functions in the quantum limit if an appropriate potential is introduced in the hydrodynamic equations (64; 65). A description of the source of this term is given in section 3.4.3 below.

3.3.4 Induction Equation

Starting from Ohm's law, and neglecting displacement current, we obtain:

$$\begin{aligned}\frac{\partial \boldsymbol{B}}{\partial t} &= \nabla \times (\boldsymbol{u} \times \boldsymbol{B}) - \nabla \times (\eta \nabla \times \boldsymbol{B}) \\ &\qquad + \frac{m}{e(1+Z)} \frac{\nabla p \times \nabla \rho}{\rho^2} + \nabla \times \left(\boldsymbol{B} \times \frac{\tau_{ei}}{m_e} \frac{\beta_1'' \chi_H^2 + \beta_0''}{\Delta} \nabla T \right), \qquad (3.1e)\end{aligned}$$

where $\boldsymbol{B}$ is the magnetic field, η the magnetic diffusivity ($\eta = 1/\sigma_c \mu_0$ where σ_c is the electric conductivity and μ_0 the vacuum permeability), m the average mass per particle, m_e the electron mass, e the elementary charge, Z the degree of ionisation, τ_{ei} the electron-ion collision time, $\Delta = \chi_H^4 + \delta_1 \chi_H^2 + \delta_0$ (where $\chi_H = \omega_{ce}\tau_{ei}$ is the Hall parameter and ω_{ce} is the electron cyclotron frequency), T the fluid temperature, and β_0'', β_1'', δ_0 and δ_1 are Braginskii coefficients (66). Values for the Braginskii coefficients are given in Table 3.1.

In addition to magnetic diffusion (second term on the right hand side of equation (3.1e)), we have written the induction equation to include baroclinic generation of magnetic field via the Biermann battery mechanism (67; 68), and the advection of the magnetic field due to the Nernst effect (69). These are the last two terms on the right hand side of equation (3.1e), respectively. In many laboratory and astrophysical

---

[*] (We can also rewrite the $\boldsymbol{J} \cdot \boldsymbol{E}$ term in equation (3.1c) to show conservation of magnetic energy more clearly, using $\frac{\partial}{\partial t} \frac{B^2}{2\mu_0} = \frac{-1}{\mu_0} \boldsymbol{B} \cdot \nabla \times \boldsymbol{E}$ which allows us to write:

$$\frac{\partial}{\partial t}\left(\rho\epsilon + \frac{\rho u^2}{2} + E_R + \frac{B^2}{2\mu_0}\right) + \nabla \cdot \left[\rho \boldsymbol{u}\left(\epsilon + \frac{u^2}{2}\right) + p\boldsymbol{u} + \frac{\boldsymbol{E} \times \boldsymbol{B}}{\mu_0}\right] = -\nabla \cdot \boldsymbol{H} + \Phi_{Bohm} \cdot \boldsymbol{u} - f_{rad} \cdot \boldsymbol{u},$$

where $(\boldsymbol{E} \times \boldsymbol{B})/\mu_0$ is the Poynting vector.)

	Z=1	**Z=2**	**Z=3**	**Z=4**	**Z→ ∞**
β_0''	3.053	1.784	1.442	1.285	0.877
δ_0	3.7703	1.0465	0.5814	0.4106	0.0961
β_1''	1.5	1.5	1.5	1.5	1.5
δ_1	14.79	10.80	9.618	9.055	7.482

Table 3.1: Numerical values for the Braginskii coefficients for various values of Z, adapted from (66).

scenarios, these terms represent the next highest order corrections to Ohm's law (70; 71). While Ohm's law contains several additional terms (69), here we restrict to the case of small magnetic fields, where zeroth order (Biermann battery) and first order (Nernst) terms have been shown to be the dominant mechanism for magnetic field generation in many plasma experiments (72).

We require equations for the charge density and electric field to close the set of equations (3.1). We can relate these using Gauss' Law and Ohm's Law:

$$\nabla \cdot \boldsymbol{E} = \frac{\rho_C}{\epsilon} \tag{3.1f}$$

$$\boldsymbol{E} = -\boldsymbol{u} \times \boldsymbol{B} + \eta \nabla \times \boldsymbol{B} - \frac{\nabla p_e}{n_e e} - \boldsymbol{B} \times \frac{\tau_{ei}}{m_e} \frac{\beta_1'' \chi_H^2 + \beta_0''}{\Delta} \nabla T \tag{3.1g}$$

Where, as above, the second term is due to diffusion of the field, the third the Biermann battery, and final term the Nernst effect.

3.4 Explicit Form of Source Terms

The source terms in equations (3.1b), (3.1c) and (3.1d) are explicitly given by:

$$\Phi_{Bohm} = \frac{\hbar^2 \rho}{2 m_e m_i} \nabla \left(\frac{\nabla^2 \sqrt{\rho}}{\sqrt{\rho}} \right) \tag{3.2a}$$

$$\boldsymbol{\sigma}_\nu = \rho \nu \left[\nabla \boldsymbol{u} + (\nabla \boldsymbol{u})^T - \frac{2}{3} (\nabla \cdot \boldsymbol{u}) \underline{\boldsymbol{I}} \right] + \zeta (\nabla \cdot \boldsymbol{u}) \underline{\boldsymbol{I}} \tag{3.2b}$$

$$\boldsymbol{F}_{EM} = \rho_C \boldsymbol{E} + \boldsymbol{J} \times \boldsymbol{B} \tag{3.2c}$$

$$\boldsymbol{q} = -\kappa_{th}\nabla T = -\chi_{th}\rho C_P \nabla T = -\frac{\chi_{th}\rho k_B \gamma}{m(\gamma - 1)}\nabla T \tag{3.2d}$$

where $\hbar$ is the reduced Planck constant, m_i the ion mass, $\nu(= \mu/\rho)$ the kinematic viscosity with μ being the dynamic viscosity, $\underline{\boldsymbol{I}}$ the identity tensor, ζ the second coefficient of viscosity, ρ_C the charge density, κ_R the Rosseland mean opacity, κ_{th} the coefficient of heat conduction, χ_{th} the kinematic coefficient of thermal diffusivity, C_P the specific heat capacity at constant pressure, and γ the adiabatic index.

The quantum potential is explicitly given in Equation (3.2a). A derivation of this term is given below in section 3.4.3. Equation (3.2b) gives the form of the stress tensor which does not assume that the fluid is incompressible, *i.e.* $\nabla \cdot \boldsymbol{u}$ does not have to be equal to zero (25). It also considers the effects of viscosity, and extends this to second order, ζ. Equation (3.2c) defines the electromagnetic (Lorentz) force on the system, in standard form. Finally, equation (3.2d) describes the thermal heat flux in the diffusive limit (73).

3.4.1 Optically Thick

$$-\nabla p_R = f_{rad} \tag{3.2e}$$

$$p_R = \frac{E_R}{3} = \frac{4\sigma T^4}{3c} \tag{3.2f}$$

$$\boldsymbol{F}_R = -\frac{16\sigma T^3}{3\kappa_R \rho}\nabla T \tag{3.2g}$$

When the fluid is optically thick, we can reduce the pressure tensor to a scalar radiation pressure and write it in terms of an isotropic energy density. Equation (3.2e) is thus only applicable in this limit. Equation (3.2f) represents the isotropic thermal radiation pressure within the plasma, and the related energy density of that radiation assuming a Planck distribution (74). Equation (3.2g) gives the radiative energy flux, within the local thermodynamic equilibrium (LTE) approximation. In this form, it corresponds to the *Rosseland heat flux* (25; 74). These equations are not applicable to the case of optically thin systems, or when there is an optically thin pre-shock material, but optically thick post-shot material (59).

3.4.2 Optically Thin

Under optically thin conditions, the source terms relating to radiation can be written as

$$p_R = 0, \tag{3.2ha}$$

$$f_{rad} = 0, \tag{3.2hb}$$

where the transfer of momentum to the plasma by radiation is zero, by definition, as the plasma is optically thin, and the remaining radiation terms, relating to radiative energy flux (equation (3.2i)), are written in terms of a cooling function,

$$L_\Lambda = \frac{\partial E_R}{\partial t} + \nabla \cdot [\boldsymbol{F}_R + E_R \boldsymbol{u}] \approx \rho \kappa_P \sigma T^4. \tag{3.2i}$$

This can be approximated with a form that is similar to the optically thick case (equation (3.2f)) where κ_P is the Planck opacity (57).

3.4.3 Quantum potential

Given the presence of the Bohm potential in the above equations, and the fact that this term is often omitted, it is important to give a detailed explanation and derivation of its appearance. It arises from rewriting the Schrödinger equation in polar form with a wavefunction given by

$$\phi = Re^{iS/\hbar},$$

where R and S are real valued functions. The Schrödinger equation can be thus divided into an imaginary part

$$\frac{\partial R}{\partial t} = -\frac{1}{2m}\left(R\nabla^2 S + 2\nabla R \cdot \nabla S\right), \tag{3.9}$$

and a real part

$$\frac{\partial S}{\partial t} = -\left[\frac{(\nabla S)^2}{2m} + V + Q\right], \tag{3.10}$$

where V is the external potential and

$$Q = -\frac{\hbar^2}{2m}\frac{\nabla^2 R}{R}.$$

If we now identify, using the correspondence to the classical limit, $R^2 = \rho$, and $\mathbf{u} = \nabla S/m$, then equation (3.9) can be re-expressed as a continuity equation, while equation (3.10) has the form of an energy equation with the classical potential corrected by the quantum term Q. This leads, for example, to the inclusion of $\rho Q/m$ as an energy density correction in the momentum equation.

In general the equations with quantum potential correction are written separately for the ion and electron species (60). For simplicity, we start by considering the case of an ideal fluid where the source terms are only pressure gradient and electromagnetic forces:

$$\frac{\partial \boldsymbol{u}_e}{\partial t} + \boldsymbol{u}_e \cdot \nabla \boldsymbol{u}_e = -\frac{\nabla p_e}{m_e n_e} - \frac{e}{m_e}(\boldsymbol{E} + \boldsymbol{u}_e \times \boldsymbol{B}) + \frac{\hbar^2}{2m_e^2}\nabla\left(\frac{\nabla^2\sqrt{n_e}}{\sqrt{n_e}}\right), \tag{3.11a}$$

$$\frac{\partial \boldsymbol{u}_i}{\partial t} + \boldsymbol{u}_i \cdot \nabla \boldsymbol{u}_i = -\frac{\nabla p_i}{m_i n_i} + \frac{e}{m_i}(\boldsymbol{E} + \boldsymbol{u}_i \times \boldsymbol{B}) + \frac{\hbar^2}{2m_i^2}\nabla\left(\frac{\nabla^2\sqrt{n_i}}{\sqrt{n_i}}\right), \tag{3.11b}$$

where n_e (n_i), $\boldsymbol{u_e}$ $(\boldsymbol{u_i})$, and p_e (p_i) are the electron (ion) number density, velocity and pressure, respectively. Quantities with no subscript are instead used to describe average fluid properties. By defining an average mass density and fluid velocity as

$$\rho = m_e n_e + m_i n_i, \quad \boldsymbol{u} = \frac{m_e n_e \boldsymbol{u}_e + m_i n_i \boldsymbol{u}_i}{m_e n_e + m_i n_i},$$

we can combine equations (3.11), into a single fluid description by multiplying each one by $n_e m_e$ and $n_i m_i$, respectively, and by adding them together. The resulting momentum equation is

$$\rho\left(\frac{\partial \boldsymbol{u}}{\partial t} + \boldsymbol{u} \cdot \nabla \boldsymbol{u}\right) = -\nabla p + \boldsymbol{J} \times \boldsymbol{B} + \frac{\hbar^2 \rho}{2 m_e m_i}\nabla\left(\frac{\nabla^2\sqrt{\rho}}{\sqrt{\rho}}\right) \tag{3.12}$$

which has the same form of the quantum potential as seen in equation (3.2a). In this derivation we have assumed quasi-neutrality, and taken the total pressure to be the sum of the electron and ion pressures, that is $p_e + p_i = p$.

3.5 Dimensional Analysis

Now we can take the full forms of the fluid equations, equations (3.1), and apply dimensional analysis to rewrite them in a dimensionless form. Non-ideal terms are modified from the original terms in the non-dimensionless equations by characteristic ratios, which contain the information about the scale of the system. Each non-ideal term generates a characteristic ratio, which can be used to determine conditions for similarity when comparing laboratory experiments to astrophysical events.

We follow the convention set out in chapter 2, equations (2.20)-(2.21) – where *starred quantities* (*i.e.* $\boldsymbol{u}^*$) are dimensionless, while *quantities with subscript 0* (*i.e.* u_0) correspond to a characteristic value for that variable.

3.5.1 Induction Equation

We first consider equation (3.1e) with the inclusion of the resistive, baroclinic and Nernst terms. By applying the transformation defined in chapter 2[†] with the additional inclusion of a temperature scaling $T \rightarrow T_0 T^*$ we have:

$$\begin{aligned}\frac{u_0}{\ell_0}\sqrt{\mu_0\rho_0}u_0\frac{\partial \boldsymbol{B}^*}{\partial t^*} = \frac{u_0}{\ell_0}\sqrt{\mu_0\rho_0}u_0\nabla^* \times (\boldsymbol{u}^* \times \boldsymbol{B}^*) \\ - \eta_0\frac{u_0}{\ell_0^2}\sqrt{\mu_0\rho_0}u_0\nabla^* \times (\eta^*\nabla^* \times \boldsymbol{B}^*) + \frac{m u_0^2}{e\ell_0^2(1+Z)}\frac{\nabla^* p^* \times \nabla^*\rho^*}{\rho^{*2}} \\ + \frac{\sqrt{\mu_0\rho_0}u_0 T_0}{\ell_0^2}\frac{\tau_{ei}}{m_e}\frac{\beta_1''\chi_H^2 + \beta_0''}{\Delta}\nabla^* \times (\boldsymbol{B}^* \times \nabla^* T^*)\,.\end{aligned}$$

Dividing through by $u_0^2\sqrt{\mu_0\rho_0}/\ell_0$, gives:

$$\begin{aligned}\frac{\partial \boldsymbol{B}^*}{\partial t^*} = \nabla^* \times (\boldsymbol{u}^* \times \boldsymbol{B}^*) - \frac{1}{Re_M}\nabla^* \times (\eta^*\nabla^* \times \boldsymbol{B}^*) \\ + \frac{1}{\mathcal{B}i}\frac{\nabla^* p^* \times \nabla^*\rho^*}{\rho^{*2}} + \frac{1}{\mathcal{N}e}\nabla^* \times (\boldsymbol{B}^* \times \nabla^* T^*)\,, \quad (3.13)\end{aligned}$$

where can recognize the magnetic Reynolds number, equation (2.19), as

$$Re_M = \frac{u_0\ell_0}{\eta_0},$$

which represents the ratio of magentic advection to magnetic diffusion, and the dimensionless numbers

$$\mathcal{B}i = \frac{e\sqrt{\mu_0\rho_0}\ell_0(1+Z)}{m}, \quad \mathcal{N}e = \frac{u_0\ell_0 m_e}{T_0\tau_{ei}}\frac{\Delta}{\beta_1''\chi_H^2 + \beta_0''} \quad (3.14)$$

which we will refer to as the Biermann number and Nernst number, respectively. These numbers represent the importance of magnetic field generation, due to the presence of electron currents, compared to magnetic field advection.

This shows that the equations of resistive MHD are scale invariant only if Re_M, $\mathcal{B}i$ and $\mathcal{N}e$, are the same in both the laboratory and astrophysical systems, or, alternatively, very large in both systems, such that these terms are negligible.

[†] $\boldsymbol{u} \rightarrow u_0\boldsymbol{u}^*, \boldsymbol{r} \rightarrow \ell_0\boldsymbol{r}^*, t \rightarrow \frac{\ell_0}{u_0}t^*, \rho \rightarrow \rho_0\rho^*$

3.6 Similarity for non-ideal equations in the optically thick case

We now consider the full system of equations (3.1) and also define additional scaling variables for current density, electric field and charge:

$$\boldsymbol{J} \to J_0 \boldsymbol{J}^*, \quad \boldsymbol{E} \to E_0 \boldsymbol{E}^*, \quad \rho_C \to \rho_{C_0} \rho_C^*.$$

We also use the optically thick expressions for source terms, as defined in section 3.4.1.

3.6.1 Momentum equation

Starting with the momentum equation (3.1b), using the above scaling transformations, dividing through a common factor $\rho_0 u_0^2/\ell_0$, and after manipulation (for a more detailed derivation please see appendix A) we get:

$$\begin{aligned} \rho^* \left(\frac{\partial \boldsymbol{u}^*}{\partial t^*} + \boldsymbol{u}^* \cdot \nabla^* \boldsymbol{u}^* \right) &= -\nabla^* \left[p^* + \frac{1}{R} T^{*4} \right] + \frac{1}{\mathcal{H}_Q} \rho^* \nabla^* \left(\frac{\nabla^{*2} \sqrt{\rho^*}}{\sqrt{\rho^*}} \right) \\ &+ \nabla^* \cdot \left\{ \frac{1}{Re} \left[\nabla^* \boldsymbol{u}^* + (\nabla^* \boldsymbol{u}^*)^T - \frac{2}{3} (\nabla^* \cdot \boldsymbol{u}^*) \underline{\boldsymbol{I}} \right] + \frac{1}{Re_\zeta} (\nabla^* \cdot \boldsymbol{u}^*) \underline{\boldsymbol{I}} \right\} \\ &+ \frac{1}{\Omega_R} \rho_C^* \boldsymbol{E}^* + \frac{1}{\Omega_H} \boldsymbol{J}^* \times \boldsymbol{B}^* \end{aligned} \tag{3.15}$$

Similarly to the resistive case shown in chapter section 2.4.2, we see that we again recover an equation with the same form as (3.1b), but with non-ideal terms modified by characteristic ratios. We define these below.

The Mihalas number, R, represents the ratio of ram pressure to radiation pressure, and it is related to the more familiar Boltzmann, Bo, number by

$$R = \frac{\rho_0 u_0^2}{4\sigma T_0^4/3c} = \frac{3c}{4u_0} \frac{\gamma - 1}{\gamma} Bo, \tag{3.16}$$

where $Bo = \rho_0 C_P T_0 u_0 / \sigma T_0^4$.

Here, we have used $k_B T_0 \sim m u_0^2$, and $C_P \sim \gamma k_B / m(\gamma - 1)$. The Boltzmann number gives the ratio of the material enthalpy flux to the radiation flux. The relation between the Mihalas number and Boltsmann number shows that these terms are of similar magnitude, as can be seen in equation (3.2f).

The importance of quantum effects to classical ones within the system is described by the number:

$$\mathcal{H}_Q = \frac{2m_e m_i \ell_0^2 u_0^2}{\hbar^2}, \tag{3.17}$$

which we will refer to as the Bohm number.

We can also recognise the Reynold's number, the ratio of viscous to inertial effects, and its obvious extension when considering the second coefficient of viscosity:

$$Re = \frac{\rho_0 u_0 \ell_0}{\mu}; \quad Re_\zeta = \frac{\rho_0 u_0 \ell_0}{\zeta} \tag{3.18}$$

From charge conservation, $\rho_{C_0} = J_0/u_0$, it follows

$$\Omega_R = \frac{\rho_0 u_0^2}{\rho_{C_0} \ell_0 E_0} = \frac{\rho_0 u_0^3}{J_0 E_0 \ell_0}, \tag{3.19}$$

which represents the ratio between Ohmic and convective heat transfer, which we call the Ohmic Number.

The ratio between convective transport and Hall diffusion is expressed by the coefficient

$$\Omega_H = \frac{u_0 \sqrt{\mu_0 \rho_0}}{J_0 \ell_0} = \frac{\mu_0 \rho_0 u_0^2}{J_0 B_0 \ell_0}, \tag{3.20}$$

which we refer to as the Hall number.

3.6.2 Energy equation

Following the same approach as before, but now using the energy equation (3.1c), and dividing through by a common factor of $\rho_0 u_0^3/\ell_0$, the dimensionless energy equation can thus be written as (see appendix A for more details):

$$\begin{aligned}
&\frac{\partial}{\partial t^*}\left(\rho^* \epsilon^* + \frac{\rho^* u^{*2}}{2} + \frac{3}{R} T^{*4}\right) + \nabla^* \cdot \left[\rho^* \boldsymbol{u}^* \left(\epsilon^* + \frac{u^2}{2}\right) + p^* \boldsymbol{u}^*\right] \\
&\qquad = \nabla^* \cdot \left\{ \frac{1}{\Pi_{thick}} \frac{T^{*3}}{\rho^*} \nabla^* T^* - \frac{3}{R} T^{*4} \boldsymbol{u}^* + \frac{1}{Pe} \frac{\gamma}{\gamma - 1} \rho^* \nabla^* T^* \right. \\
&\qquad \left. + \frac{1}{Re}\left[\nabla^* \boldsymbol{u}^* + (\nabla^* \boldsymbol{u}^*)^T - \frac{2}{3}(\nabla^* \cdot \boldsymbol{u}^*)\underline{\boldsymbol{I}}\right] \cdot \boldsymbol{u}^* + \frac{1}{Re_\zeta}(\nabla^* \cdot \boldsymbol{u}^*)\underline{\boldsymbol{I}} \cdot \boldsymbol{u}^* \right\} \\
&\qquad - \frac{1}{\Omega_R} \boldsymbol{J}^* \cdot \boldsymbol{E}^* + \frac{1}{\mathcal{H}_Q} \rho^* \nabla^* \left(\frac{\nabla^{*2}\sqrt{\rho^*}}{\sqrt{\rho^*}}\right) \cdot \boldsymbol{u}^* - \frac{1}{R} T^{*4} \nabla^* \cdot \boldsymbol{u}^*
\end{aligned} \tag{3.21}$$

Analogous to the momentum equation we have new dimensionless numbers. Ratios not given above are defined below.

We define the radiation number, Π_{thick}, which is related to the Boltzmann number (in the same way as the Mihalas number, above) by:

$$\Pi_{thick} = \frac{3\kappa_R \rho_0^2 \ell_0 u_0^3}{16\sigma T_0^4} \left(= \frac{3\ell_0}{16\lambda_R} \frac{\gamma - 1}{\gamma} Bo \right). \tag{3.22}$$

This number describes the importance of material energy flux compared to the radiative energy flux, weighted by the ratio of the mean free path of the radiation, $\lambda_R = 1/\kappa_R \rho_0$, to the characteristic length scale of the system.

The Péclet number gives the importance of thermal diffusion against convective transport:

$$Pe = \frac{\ell_0 m u_0^3}{\chi_{th} k_B T_0} = \frac{\ell_0 u_0}{\chi_{th}}, \tag{3.23}$$

where we have used again the relation $k_B T \sim m u_0^2$.

3.7 Similarity for non-ideal equations in the optically thin case

It is worth noting that the Mihalas and the radiation numbers as shown above rely on the material in question being optically thick to radiation. The form of the equations as shown so far cannot be used in presence of an optically thin plasma. The scaling relations in the optically thin case have been discussed in terms of cooling functions and characteristic timescales (52; 56), and using Lie group theory (57). Moreover, in the special situation of thick-thin radiation transport a more complex treatment is required (59).

The dimensionless momentum and energy equations now read as follows, using expressions for optically thin radiation terms from section 3.4.2, where we follow the cooling function formalism.

3.7.1 Momentum Equation

$$\begin{aligned}\rho^* \left(\frac{\partial \boldsymbol{u}^*}{\partial t^*} + \boldsymbol{u}^* \cdot \nabla^* \boldsymbol{u}^* \right) &= -\nabla^* p^* + \frac{1}{\mathcal{H}_Q} \rho^* \nabla^* \left(\frac{\nabla^{*2} \sqrt{\rho^*}}{\sqrt{\rho^*}} \right) \\ &+ \nabla^* \cdot \left\{ \frac{1}{Re} \left[\nabla^* \boldsymbol{u}^* + (\nabla^* \boldsymbol{u}^*)^T - \frac{2}{3} (\nabla^* \cdot \boldsymbol{u}^*) \underline{\boldsymbol{I}} \right] + \frac{1}{Re_\zeta} (\nabla^* \cdot \boldsymbol{u}^*) \underline{\boldsymbol{I}} \right\} \\ &+ \frac{1}{\Omega_R} \rho_C^* \boldsymbol{E}^* + \frac{1}{\Omega_H} \boldsymbol{J}^* \times \boldsymbol{B}^* \end{aligned} \tag{3.24}$$

3.7.2 Energy Equation

$$\begin{aligned} &\frac{\partial}{\partial t^*} \left(\rho^* \epsilon^* + \frac{\rho^* u^{*2}}{2} \right) + \nabla^* \cdot \left[\rho^* \boldsymbol{u}^* \left(\epsilon^* + \frac{u^2}{2} \right) + p^* \boldsymbol{u}^* \right] \\ &= \nabla^* \cdot \left\{ \frac{1}{Pe} \frac{\gamma}{\gamma - 1} \rho^* \nabla^* T^* + \frac{1}{Re} \left[\nabla^* \boldsymbol{u}^* + (\nabla^* \boldsymbol{u}^*)^T - \frac{2}{3} (\nabla^* \cdot \boldsymbol{u}^*) \underline{\boldsymbol{I}} \right] \cdot \boldsymbol{u}^* + \frac{1}{Re_\zeta} (\nabla^* \cdot \boldsymbol{u}^*) \underline{\boldsymbol{I}} \cdot \boldsymbol{u}^* \right\} \\ &\qquad - \frac{1}{\Omega_R} \boldsymbol{J}^* \cdot \boldsymbol{E}^* + \frac{1}{\mathcal{H}_Q} \rho^* \nabla^* \left(\frac{\nabla^{*2} \sqrt{\rho^*}}{\sqrt{\rho^*}} \right) \cdot \boldsymbol{u}^* - \frac{1}{\Pi_{thin}} \rho^* T^{*4} \end{aligned} \tag{3.25}$$

As for the optically thick case, we recover a set of dimensionless characteristic numbers. The only difference is that the radiation term is now altered, and the proper number to use in this case is

$$\Pi_{thin} = \frac{u_0^3}{\kappa_p \sigma \ell_0 T_0^4} = \frac{\lambda_P}{\ell_0} \frac{\rho_0 u_0^3}{\sigma T_0^4} \left(= \frac{\lambda_P}{\ell_0} \frac{\gamma - 1}{\gamma} Bo \right)$$

which has a similar form to the radiation number for the optically thick case. It is a measure of the ratio between the material and radiative energy fluxes, weighted by the ratio of the mean free path, $\lambda_P = 1/\kappa_P \rho_0$, to the characteristic length scale of the system ℓ_0. However, please note that ratio between the radiation mean free path and ℓ_0 is reversed when going from the optically thick to the optically thin regime.

3.8 Laboratory to Astrophysical Scaling

A summary of the scaling variables and all the dimensionless numbers is given in Table 3.2. As discussed earlier, similarity between the laboratory and astrophysical object is achieved if the dimensionless numbers are the same or suffiently large in both systems (the ideal MHD case). Under either of these conditions, we take $\ell_0^{(1)}$, $u_0^{(1)}$,

$\rho_0^{(1)}$, $J_0^{(1)}$, $E_0^{(1)}$, and $T_0^{(1)}$ as the characteristic scaling parameters for the laboratory experiment. The astrophysical system has corresponding values given by

$$\ell_0^{(2)} = g_a \ell_0^{(1)}, \quad u_0^{(2)} = g_b u_0^{(1)}, \quad \rho_0^{(2)} = g_c \rho_0^{(1)},$$
$$J_0^{(2)} = g_d J_0^{(1)}, \quad E_0^{(2)} = g_e E_0^{(1)}, \quad T_0^{(2)} = g_f T_0^{(1)},$$

where $g_{a,b,c,d,e,f}$ are scaling constants. From this set of parameters, we can scale all the other characteristic quantities as

$$t_0^{(2)} = \frac{g_a}{g_b} t_0^{(1)}, \quad p_0^{(2)} = g_c g_b^2 p_0^{(1)}, \quad B_0^{(2)} = g_b \sqrt{g_c} B_0^{(1)},$$
$$\epsilon_0^{(2)} = g_b^2 \epsilon_0^{(1)}, \quad \rho_{C_0}^{(2)} = \frac{g_d}{g_b} \rho_{C_0}^{(1)}.$$

Thus we have the absolute similarity case from Falize et al. (31). All the details concerning the microphysics of the two systems are contained only in the dimensionless numbers given in Table 3.2.

3.9 Experimental Comparison

3.9.1 Assumptions

We now apply the scaling relations to a few recent experiments and discuss how they can be used to meaningfully describe astrophysical environments. We focus our attention on the case when radiation becomes important, mainly because, as we will see below, this is where similarity between the laboratory and the astrophysical systems is difficult to achieve. On the other hand, in absence of significant radiative effects, hydrodynamic or MHD similarities has been successfully applied to wide range of problems. A comprehensive review of laboratory astrophysics experiments is given in the following articles (15; 16; 25; 75).

In order to evaluate these numbers, we will first define some assumptions. We assume the plasma is in thermodynamic equilibrium at temperature T (in eV) and carries a mass density ρ (in g/cm^3) from ions of atomic mass A and charge Z. The magnetic field is B (in G). Charge neutrality implies an equal number of negative charges carried by mobile electrons. These assumptions are applicable to both the laboratory and astrophysical plasmas. Following (52; 76), the kinematic viscosity is

$$\nu\,(\mathrm{cm}^2/\mathrm{s}) = \mathrm{Min}\left\{ \begin{array}{l} 3.3 \times 10^{-5}\, \frac{A^{1/2} T^{5/2}}{Z^4 \rho \Lambda} \\ 2.8 \times 10^{43}\, \frac{\rho^2 \Lambda}{A^{5/2} Z^2 B^2 T^{1/2}} \end{array} \right\}, \tag{3.26}$$

where Λ is the Coulomb logarithm. The thermal diffusivity is (52) is

Characteristic quantity	**Definition**
Length	ℓ_0
Velocity	u_0
Density	ρ_0
Current density	J_0
Electric field	E_0
Temperature	T_0
Time	$t_0 = \ell_0/u_0$
Pressure	$p_0 = \rho_0 u_0^2$
Magnetic field	$B_0 = u_0\sqrt{\mu_0\rho_0}$
Specific internal energy	$\epsilon_0 = u_0^2$
Charge density	$\rho_{C_0} = J_0/u_0$
Reynolds number	$Re = \rho_0 u_0 \ell_0/\mu$
Reynolds number (bulk)	$Re_\zeta = \rho_0 u_0 \ell_0/\zeta$
Magnetic Reynolds number	$Re_M = u_0\ell_0/\eta$
Biermann number	$\mathcal{B}i = e(1+Z)\sqrt{\mu_0\rho_0}\ell_0/m$
Nernst number	$\mathcal{N}e = u_0\ell_0 m_e \Delta/T_0\tau_{ei}(\beta_1''\chi_H^2 + \beta_0'')$
Mihalas number	$R = 3c\rho_0 u_0^2/4\sigma T_0^4$
Radiation number (Thick)	$\Pi_{thick} = 3\ell_0\rho_0 u_0^3/16\lambda_R\sigma T_0^4$
Radiation number (Thin)	$\Pi_{thin} = \lambda_P\rho_0 u_0^3/\ell_0\sigma T_0^4$
Péclet number	$Pe = \ell_0 u_0/\chi_{th}$
Ohmic number	$\Omega_R = \rho_0 u_0^3/J_0 E_0 \ell_0$
Hall number	$\Omega_H = \mu_0\rho_0 u_0^2/J_0 B_0 \ell_0$
Bohm number	$\mathcal{H}_Q = 2m_e m_i u_0^2 \ell_0^2/\hbar^2$

Table 3.2: List of scaling variables and dimensionless numbers

$$\chi_{th}\,(\mathrm{cm^2/s}) = \mathrm{Min}\left\{\begin{array}{l} 3.3\times 10^{-3}\,\frac{AT^{5/2}}{Z(Z+1)\rho\Lambda} \\ 8.6\times 10^{9}\,\frac{A^{1/2}T}{ZB} \end{array}\right\}. \tag{3.27}$$

The magnetic diffusivity can be written as (77)

$$\eta\,(\mathrm{cm^2/s}) = 2.4\times 10^{5}\,\frac{Z\Lambda}{T^{3/2}}. \tag{3.28}$$

The electron-ion collision time is given by (76)

$$\tau_{ei}\,(\mathrm{s}) = 5.2\times 10^{-16}\,\frac{A^2 T^{3/2}}{Z^2\rho\Lambda}. \tag{3.29}$$

In the case of a fully ionised plasma, the Rosseland opacity is only determined by the free-free absorption, thus (58)

$$\kappa_R\,(\mathrm{cm^2/g}) = 4.4\times 10^{8}\frac{Z^3\rho}{A^2 T^{7/2}}. \tag{3.30}$$

For typical astrophysical plasmas, the Planck opacity is (78)

$$\kappa_P\,(\mathrm{cm}^2/\mathrm{g}) = 1.8 \times 10^{13}\,\frac{Z\rho}{A^2T^4}, \tag{3.31}$$

and for bremsstrahlung-dominated cooling (52)

$$\kappa_P\,(\mathrm{cm}^2/\mathrm{g}) = 3.1 \times 10^{10}\,\frac{Z^2\rho}{A^2T^{7/2}}. \tag{3.32}$$

At higher densities (near and above solid) and when line radiation transport must be included in the calculations, the Rosseland and Planck opacity are tabulated as (35)

$$\kappa_{P,R}\,(\mathrm{cm}^2/\mathrm{g}) = \kappa_0\rho^\alpha T^\beta, \tag{3.33}$$

where κ_0, α and β are material dependent constants (see Tables 3.3 & 3.4). The Rosseland and Planck opacities are bound to a maximum value given by (35)

$$\kappa_{P,R}^{\max}\,(\mathrm{cm}^2/\mathrm{g}) = 6.1 \times 10^{6}\,\frac{Z}{AT}. \tag{3.34}$$

Even in the case that the dimensionless numbers are large in both the laboratory and astrophysical systems, their magnitude can be very different. It is then important to quantify the error in fluid variables in the ideal MHD approximation due to finite values for such dimensionless numbers. For the optically thick case, we have:

$$\frac{\Delta B}{B_{\mathrm{id}}} \sim \left(\frac{1}{Re_M^2} + \frac{1}{\mathcal{B}i^2} + \frac{1}{\mathcal{N}e^2}\right)^{1/2}, \tag{3.35}$$

$$\begin{aligned}\frac{\Delta\rho u}{(\rho u)_{\mathrm{id}}} \sim \Bigg(&\frac{1}{R^2} + \frac{1}{\mathcal{H}_Q^2} + \frac{1}{Re^2} + \frac{1}{Re_\zeta^2} + \\ &\frac{1}{\Omega_R^2} + \frac{1}{\Omega_H^2}\Bigg)^{1/2},\end{aligned} \tag{3.36}$$

$$\begin{aligned}\frac{\Delta\rho\epsilon}{(\rho\epsilon)_{\mathrm{id}}} \sim \Bigg(&\frac{1}{R^2} + \frac{1}{\Pi_{thick}^2} + \frac{1}{Pe^2} + \\ &\frac{1}{\mathcal{H}_Q^2} + \frac{1}{Re^2} + \frac{1}{Re_\zeta^2} + \frac{1}{\Omega_R^2}\Bigg)^{1/2},\end{aligned} \tag{3.37}$$

where B_{id}, $(\rho u)_{\mathrm{id}}$, and $(\rho\epsilon)_{\mathrm{id}}$ refers to the magnetic field, momentum and energy, respectively, in the ideal MHD approximation. Similar relations can be straightforwardly derived for optically thin plasmas.

Material	κ_0	α	β
CH	2.00×10^6	0.14	-2.00
Al	1.04×10^8	0.48	-2.48
Ti	3.07×10^7	0.39	-2.21
Fe	6.29×10^7	0.31	-2.27
Cu	5.93×10^7	0.29	-2.21
Mo	1.99×10^6	0.22	-1.49
Sn	3.70×10^6	0.16	-1.57
Xe*	2.00×10^8	0.00	-2.00
Ba	5.89×10^6	0.14	-1.62
Eu	2.89×10^6	0.09	-1.45
W	5.59×10^5	0.01	-1.12
Au	6.00×10^6	0.30	-1.50
Pb	4.11×10^5	0.00	-1.05
U	7.76×10^5	0.04	-1.14

Table 3.3: List of coefficient values for the mean Rosseland opacity for various elements from equation (3.33). Adapted from (35) and (25), and * from SESAME tables.

Material	κ_0	α	β
CH	2.00×10^5	0.00	-1.00
Al	6.01×10^8	0.48	-2.42
Ti	1.40×10^8	0.44	-2.07
Fe	2.22×10^8	0.38	-2.13
Cu	2.31×10^8	0.36	-2.22
Mo	1.54×10^7	0.31	-1.56
Sn	1.91×10^7	0.23	-1.59
Xe*	3.00×10^9	0.00	-2.00
Ba	2.77×10^7	0.24	-1.64
Eu	1.68×10^7	0.24	-1.54
W	3.06×10^6	0.20	-1.23
Au	3.33×10^6	0.17	-1.23
Pb	4.17×10^6	0.16	-1.27
U	1.04×10^7	0.19	-1.42

Table 3.4: List of coefficient values for the mean Planck opacity for various elements from equation (3.33). Adapted from (35) and (25), and * from SESAME tables.

3.9.2 Experiments

Characteristic quantity	**Lab**	**Astro**
Length	100 μm	1.0×10^8 km
Velocity	300 km/s	3.0×10^3 km/s
Density	1 g/cm^3	1.7×10^{-9} g/cm^3
Temperature	250 eV	1000 eV
Time	300 ps	9 hours
Pressure (Ram)	90 TPa	15 MPa
Reynolds number	4.0×10^6	1.9×10^{12}
Magnetic Reynolds number	8.7	1.0×10^{20}
Biermann number	130	5.2×10^{13}
Nernst number	0.1	1.3×10^6
Mihalas number	5,000	3.3×10^{-6}
Radiation number (Thick)	0.5	2.7×10^{-4}
Péclet number	1,200	3.6×10^9
Bohm number	6.4×10^{19}	2.5×10^{48}

Table 3.5: Example of scaling under radiative conditions from the laboratory (10) to a supernova shock breakout.

Firstly, we consider a recent implosion experiment on the National Ignition Facility (NIF) laser (10) which is related to shock waves in core-collapse supernova explosions, surrounded by an optically thick envelope or wind. Typical values for these type of systems are given, based on values from Katz et al. (30), in Table 3.5. Whilst the experiment can indeed reproduce the supernova shock in many aspects, as the Reynold's number and Péclet numbers are large in both cases, the similarity breaks down when considering the Mihalas number, and is only marginally satisfied for magnetic transport (due to diffusion and advection along the temperature gradient, rather than with the fluid flow as in the astrophysical case). This means that the radiation pressure is significantly smaller than the material pressure in the laboratory and it does not change the form of the energy equation, unlike the astrophysical case where radiation pressure is much more important than the material pressure. Even if $R \gg 1$ in the laboratory, the effect of radiation can be important due to radiation flux in the energy equation, but in this case, the large difference in the radiation number makes the similarity marginally satisfied. This example shows that radiation dominated environments are yet challenging to achieve even on the currently available largest laser facilities.

Characteristic quantity	**Lab**	**Astro**
Length	150 μm	1.4 $\times 10^6$ km
Velocity	500 km/s	35 km/s
Density	1 $\times 10^{-4}$ g/cm^3	6.6 $\times 10^{-10}$ g/cm^3
Temperature	100 eV	15 eV
Time	300 ps	0.5 days
Pressure (Ram)	25 GPa	810 Pa
Reynolds number	1,800	1.8×10^7
Magnetic Reynolds number	160	1.6×10^{16}
Biermann number	3.8	1.9×10^9
Nernst number	1.9×10^{-4}	12
Radiation number (Thin)	460	4.4×10^{-6}
Péclet number	3.4	3.4×10^4
Bohm number	6.2×10^{15}	6.2×10^{49}

Table 3.6: Comparison of laboratory experiment to an astrophysical case (Herbig-Haro object). From (19).

Radiative jets and outflows are present in several young stellar objects (79). Amongst more recent work, we focus on the the experiment by Tikhonchuk et al. (19), who claim to have good scaling between their experiment and astrophysics, and have entered a regime where radiative effects are important. The scaling relations and corresponding dimensionless numbers are given in Table 3.6. We indeed see that in this specific case, the experiment succeeds in matching the trend, if not magnitude, of many of the dimensionless numbers, for example the Reynolds and Péclet numbers and therefore we can expect the general hydrodynamic flow to be well matched in the two systems. However the radiation number remains too large compared to the astrophysical case: material energy flux in the laboratory is dominating over the radiation flux. Similarity is partially satisfied when considering Magnetic Reynolds and Biermann numbers – suggesting that the magnetic field diffusion is negligible; but the difference in the Nernst number indicates the importance of thermal advection in the laboratory case.

Other experiments have been able to better match values relating to radiative effects. In the experiments by Krauland et al. (11; 80) the values of Π_{thin} are similar in the experimental and astrophysical cases: ∼0.03 and ∼1, respectively. Thus the radiative and material energy fluxes are comparable within an order of magnitude. This is characteristic of the more complex optically thick post-shock, optically thin pre-shock conditions found, for example, in accretion processes in interacting binary star systems.

It is also important to note that, while values of these characteristic ratios can lead to one process dominating over the other (e.g. the effects of radiative flux are greater than those from material flux in the laboratory, see Table 3.5), their ratio could be many orders of magnitude different to the astrophysical case. A well scaled experiment would show, at least, the correct trend in the ratio of the characteristic values (*i.e.* large, if the value for the astrophysical case is large, or vice versa) for all quantities.

Another aspect of the scaling relations that is worth discussing is the importance of the Bohm potential. Whilst this term is of no significance in the tenuous interstellar plasma, it can become important when considering small scales, or compact objects, particularly for densities exceeding $10^{23} - 10^{29}$ cm^{-3} (60), which are found, for example, in white dwarfs and neutron stars.

This is particularly relevant when considering Kolmogorov turbulence (81). In the inertial range $\rho u_\ell^3/\ell = \dot{\epsilon} =$ constant, where u_ℓ is the characteristic velocity at scale ℓ, and $\dot{\epsilon}$ is the total power injected into turbulence, the characteristic eddy turnover rate at scale ℓ is $u_\ell/\ell \sim (\dot{\epsilon}/\rho)^{1/3}\ell^{-2/3}$. Quantum effects are expected to become important when $\hbar^2/2m_e\ell^2 \sim mu_\ell^2$, which defines the scale

$$\ell_q \simeq \left(\frac{\hbar^2}{2m_e m}\right)^{3/8}\left(\frac{\rho}{\dot{\epsilon}}\right)^{1/4}. \tag{3.38}$$

We also notice that the rate of viscous dissipation on a scale ℓ is given by ν/ℓ^2. Equating this to the eddy turnover rate, we determine the scale at which viscous dissipation becomes dominant:

$$\ell_\nu \simeq \nu^{3/4}\left(\frac{\rho}{\dot{\epsilon}}\right)^{1/4}, \tag{3.39}$$

and quantum effects will lie within the inertial range if $\ell_q > \ell_\nu$, or

$$\nu\,(\mathrm{cm}^2/\mathrm{s}) < \frac{1.9\times10^{-4}}{A^{1/2}}. \tag{3.40}$$

Since the viscosity decreases as function of the density, it is then obvious to expect quantum effects to become more important at higher densities. Similar considerations apply to the resistive scale. If the above conditions are satisfied, we would see some change in the structure of turbulence below the scale ℓ_q. This can become important when considering the fluid core of white dwarf stars (82) as shown in Table 3.7.

Characteristic quantity	**Astro**
Length	10^3 km
Velocity	50 km/s
Density	10^7 g/cm^3
Temperature	10 keV
ℓ_q/ℓ_ν	50

Table 3.7: Typical parameters for white dwarf stars, adapted from (83; 84).

In the laboratory, Bose-Einstein Condensates exhibit both quantum effects and fluid behaviour (85). A calculation of the Bohm number for He-4, with a limiting critical velocity of 18.2 cm/s, gives $\mathcal{H}_Q \sim 0.001$ for a scale length of 0.31 μm (corresponding to the diameter of the cylindrical channel the He fluid was flowing through) (86). As we expect, $\mathcal{H}_Q < 1$, and so quantum effects are of great importance in such systems.

3.10 Summary

In this section we expanded the fluid dynamic equations, introduced in chapter 2, to include non-ideal source terms including quantum, resistive and radiative effects. We then performed dimensional analysis to acquire the scale invariant form of these equations, which revealed a set of characteristic numbers that can be used to quantify the departure from ideal fluid behaviour. The scale invariance properties of the MHD equations have been successfully exploited to describe astrophysical phenomena in a variety of laboratory experiments (16; 25; 75), and here we have provided a unified theoretical framework that is common to all these experiments and can be applied to the planning and analysis of future ones. To show this, we compared recent laboratory experiments to their astrophysical counterparts to determine the extent of their similarity. We conclude that many effects are well described in the lab at present – *i.e.* magnetic and viscous effects – but radiative effects are still difficult and require more research. Work in this chapter is contained in an article published in the Astrophysical Journal, Cross et al. (2015) (**?**).

Chapter 4

The Orion Experiment

> *"See now the power of truth; the same experiment which at first glance seemed to show one thing, when more carefully examined, assures us of the contrary."*
>
> – Galileo Galilei,
>
> *Discorsi e dimostrazioni matematiche, intorno á due nuove scienze*
> *(Discourses and Mathematical Demonstrations Relating to Two New Sciences)*

In this chapter a recent laser experiment, led by the author at the Orion laser facility (87), will be discussed. The relevent astrophysical motivation and theory is introduced in the first section, and then previous work is described. Instrumentation and diagnostics used on the experiment are introduced, as well as the target and laser parameters. Finally the results are shown and discussed, with particular emphasis on the comparison to the astrophysical case.

4.1 Theoretical and Astrophysical Motivation

4.1.1 Astrophysical Background

The Orion experiment is a result of a campaign to further our understanding of an astrophysical event by using a laboratory analogue. The astrophysical case of interest is the accretion region of a binary star system of a Magnetic Cataclysmic Variable [MCV] star pulling material from a late, main sequence star (88).

In binary star systems movement of material from one star to another is common (22). Generally this is mediated by gravity: with the denser star – the primary –

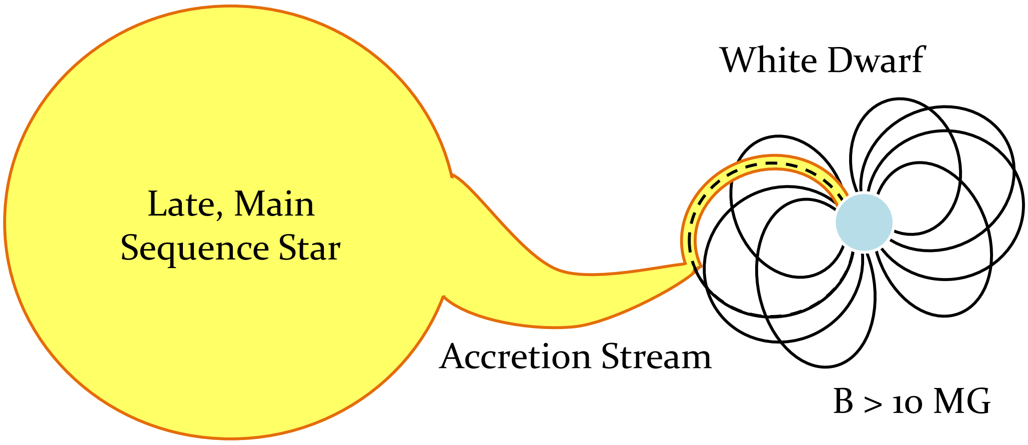

Figure 4.1: Figure, adapted from (89), showing the accretion of material onto a white dwarf from a larger star. Material is initially pulled from the main sequence star, and accelerated, due to the gravitational force of the white dwarf. As the material becomes more ionised, and enters into the white dwarf's magnetic field, it instead follows the field lines and impacts onto the poles of the star in an accretion column.

pulling material from the lighter – the secondary. Under these conditions, we find *accretion discs* around the primary star as a result of conserving angular momentum, where material begins to orbit the star, gradually moving closer to the surface.

If the primary star has a magnetic field, then we can begin to disrupt the normal flow. A class of stars known as Cataclysmic Variables [CVs] can exhibit this behaviour. In the non-magnetic case, we observe the accretion disc case as described above. In this case, and the two following, the secondary star is normally a low mass red dwarf, with the assumption that it is also main sequence (90). As the magnetic field strength increases we encounter a series of stars called *Intermediate Polars*, or *DQ Herculis*, systems (89). In this case the magnetic field is strong enough to disrupt the flow of material from the secondary, but not strong enough to completely remove the accretion disc mediated by the gravitational attraction. (This system can also occur if the two stars are too far apart.) The final class of stars are the *Polar*, or *AM Herculis*, systems. These are characterised by the primary star being a white dwarf with a very strong magnetic field, in excess of tens of megaGauss. In this case the field is strong enough to completely disrupt the flow of material from the secondary star away from the gravitationally-mediated accretion disc. Material is originally pulled away by gravity, but, as it approaches the white dwarf, the accretion stream instead follows the field lines of the white dwarf and so impacts onto the poles of the star in an *accretion column*. A schematic of this system can be seen in figure 4.1.

4.1.2 Accretion Column

It is the accretion column that is of most interest in this system. We see significant departure in observations from the gravitationally-mediated accretion discs, and there are competing theories to try and explain astrophysical observations.

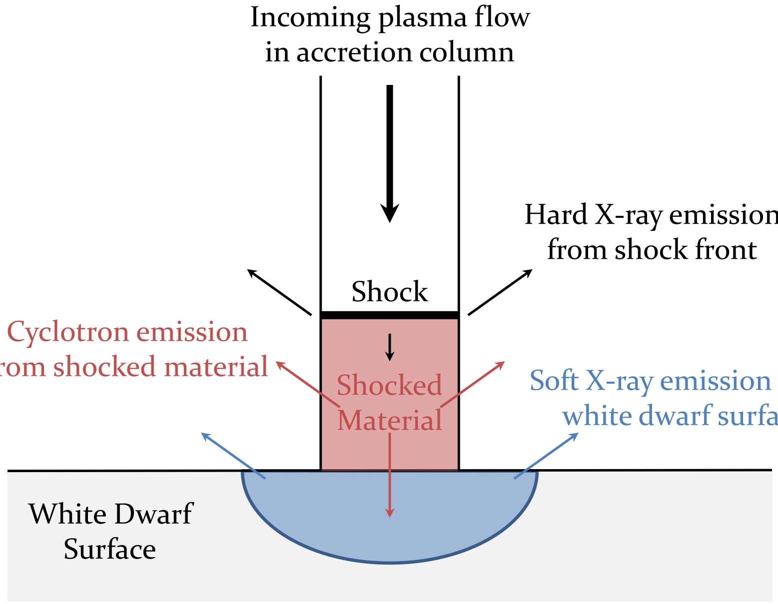

Normal, single accretion mode

Figure 4.2: Figure showing the *normal, single* accretion mode of material onto a white dwarf. Material flows in from the top onto the pole of the white dwarf where a single shock forms in the accretion column above the surface.

The infalling material from the secondary star is directed by the white dwarf magnetic field and accelerated by gravity onto the white dwarf surface at the poles of the star. At this interaction point a strong shock forms, travelling counter to the incoming flow, which is strongly radiative. The shock height above the surface is expected to be stationary (in the frame of the star) as a result of the energy balance between the incoming material energy flux and the radiative losses as the plasma impacts onto the surface of the white dwarf. As a result of this radiation we also observe a different X-ray spectrum: with hard bremsstrahlung X-rays from the shock itself, soft X-rays from the white dwarf photosphere heated by the shock and re-radiated, and cyclotron emission from the shock-heated material.

The expected shock height is of the order of 1,000s of kilometres (91) and thus impossible to resolve against the white dwarf surface with current telescopes. As such, there is some uncertainty in the theory relating to the height of this stand off shock and the explanation of observed radiation. The ratio of the hard to soft X-ray flux emitted is used as a metric (92) to determine the type of accretion that is occuring, which itself determines the shock height.

In general we have two competing accretion modes of interest in MCV star systems: *normal, single accretion* (93), figure 4.2, and *blobby accretion* (94), figure 4.3. In the *single accretion* mode, the incoming material shocks in the optically thin plasma stream within the accretion column before reaching the white dwarf photosphere. As such much of the X-ray spectrum comes from bremsstrahlung from the shock front, the hard to soft X-ray ratio is greater than one. This is thought to be characterised by a single shock across a large accretion column. In the *blobby accretion* mode, the incoming material penetrates the white dwarf photosphere before shocking. Much of the hard X-ray radiated from the shock front is reabsorbed into the white dwarf photosphere and is re-emitted as a thermal source in the soft X-ray and UV range. Thus the ratio of hard to soft X-rays is below one. In this case the incoming flow is expected to filament into multiple streams on the approach to the white dwarf surface. In the experimental case we are interested in being able to distinguish the two thus aiding astrophysical work investigating spectra from such star systems where there is already disagreement in how to interpret such signals (see (96) and response (95)). To this end we will focus on the normal accretion mode, where a single shock is found away from the photosphere. The aim is to create a laboratory analogue of this system to better understand how it forms, and its subsequent dynamics. It is important to understand the physics of the accretion column as many of its properties, and the shock within it, are dependent on the nature of the white dwarf, such as its mass and size. For example in the normal accretion mode, the shock height, h_s, is related to the mass accretion rate, $\dot{m}$, and white dwarf mass and radius, M_{WD} and R_{WD} respectively, by the following (39):

$$h_s = 7.60 \times 10^4 \left(\frac{40}{\dot{m}}\right) \left(2\frac{M_{WD}}{M_\odot}\right)^{\frac{3}{2}} \left(\frac{10^7}{R_{WD}}\right)^{\frac{3}{2}} \tag{4.1}$$

where $M_\odot$ is the solar mass. Being able to interpret the spectra from astrophysics with certainty would thus lead to a much better characterisation of the star system itself.

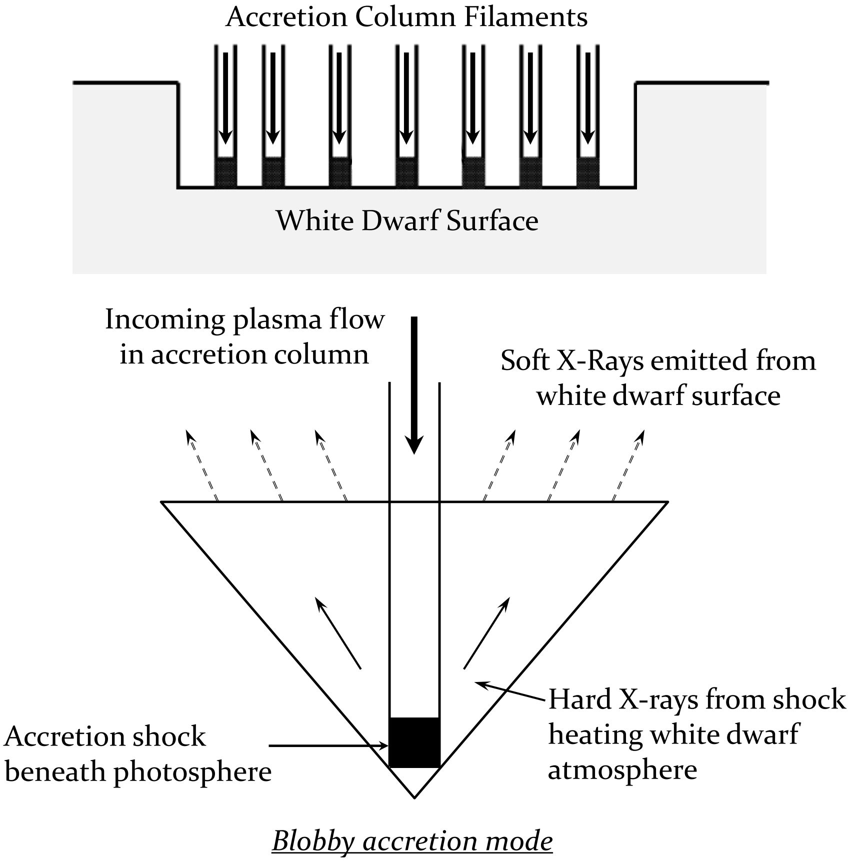

Figure 4.3: Figure, adapted from (95), showing the *blobby* accretion mode of material onto a white dwarf. Material flows in from the top onto the pole of the white dwarf where multiple filaments form in the accretion column and each penetrates into the photosphere before shocking. The lower image shows a single magnified filament.

4.2 Target Design

Part of the previous work in this series of experiments looked at appropriate target design (97) for a laboratory analogue – see section 4.3 below for more detail on the experimental campaign. The target design was carefully considered as it not only needed to fulfill the role as a suitable laboratory analogue to the accretion column system, but also work well with the laboratory based diagnostics and laser system. For this reason some decisions were taken as to increase the similarity, and others to facilitate the use of certain diagnostics.

Simplifying the astrophysical case, we can break down the dynamics of the problem into three steps:

1. Plasma from the secondary star is accelerated,

2. The white dwarf magnetic field constrains the flow into a column,

3. This impacts onto the surface of the white dwarf.

The target needs to mimic the dynamics above. We need to have a source of plasma, a means of constraining the flow, and an obstacle for the plasma to impact onto. (As discussed earlier we are interested in the normal accretion mode, and so are concerned with a shock forming away from an obstacle, rather than penetration of the flow into it.) This is shown in figure 4.4.

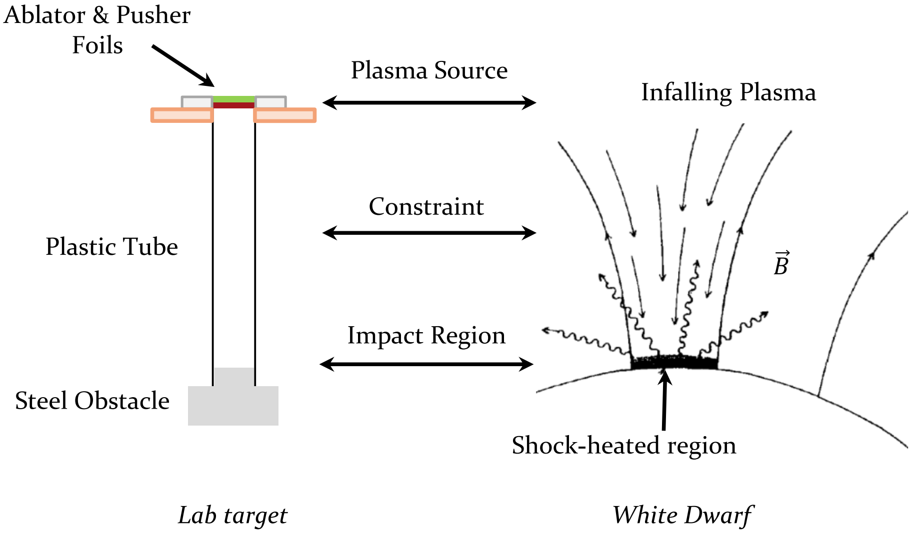

Figure 4.4: Comparison of the astrophysical system and laboratory target. The three important parts of the astrophysical case are simulated using a laboratory target. White dwarf figure adapted from 1978 thesis of A. R. Master, University of Illinois.

The target is made up of a plastic (polyimide) tube closed at one end with an obstacle, and closed at the other with two foils. Lasers illuminate the foils and form a plasma which then flows down the tube and hits the obstacle. In the MCV system, the plasma flow at the poles is parallel to the magnetic field lines, so the field acts to constrain the flow but does not otherwise affect the dynamics. The tube acts to constrain the plasma flow, analgous to the magnetic field in the astrophysical case. The surface of the white dwarf is significantly denser than the incoming flow and so the obstacle in the target (normally steel, but also quartz) was chosen as it is denser than the predicted incoming flow.

Figure 4.5: Images of a target used in our experimental campaign, reproduced from (98). The left image shows the target from the obstacle side, and the right from the pusher side.

4.2.1 Target Details

An image of the final target is shown in figure 4.5. The target consisted of a 550 µm inner diameter, 650 µm outer diameter, 3.5 mm long polyimide tube, with foils affixed at one end and an obstacle at the other. The drive beams illuminated the end of the target capped with two foils: a 25 µm thick plastic ablator and a 25 µm thick doped plastic foil, doped with either gold, bromine or chlorine. For the gold doped plastic, alternating layers of CH and Au, with 6 µm thick CH and 300 nm thick Au, were deposited giving a total Au concentration in the pusher of 39% by mass. The bromine doped plastic was formed by pressing and heating a powder, leading to a foil containing 43% bromine by weight (details are found in the paper by Spindloe et al. (98)). The chlorine (PVDC) foil was commercially available at the thickness required (25 µm), ∼40% by weight. A copper cone was placed just behind the ablator and pusher foils to protect the diagnostics from the direct view of the laser spot, and from emission from the blow-off plasma. These were all attached to the plastic tube using a plastic washer.

The other end of the tube was sealed with a steel obstacle, which was inserted ∼150 µm into the tube. In some targets, ∼1 mm long slits were cut into the tube near the steel obstacle, at 45° to the horizontal plane. This allowed for clearer X-ray radiography of, and collection of optical emission from, the interacting plasma. Some targets also had 400 lines per inch (63 µm spacing) gold grids at 45° to the horizontal plane, as seen in figure 4.5, to act as a fiducial for magnification and resolution in the X-ray diagnostic.

During the experiment the drive beams are focussed onto the plastic ablator foil, which absorbs the laser energy, causing it to expand. This induces the pusher foil to be shocked into the plasma state, accelerated by rocket action and launched down the tube as a fluid. After the laser pulse ends, this accelerated plasma expands and becomes a homogeneous flow. The role of gravity in the astrophysical case as the method accelerating the plasma is taken by the laser in the laboratory experiment. The laser spot size was deliberately chosen to be larger than the inner diameter of the tube so as to be less susceptible to misalignment and thus preserve a relatively uniform transverse profile of the plasma flowing down the tube, more details on the experimental arrangement can be found in section 4.4 below. Progressively, as increasing amount of mass is accumulated, the pressure builds up and a shock wave is launched back in the opposite direction to the incoming plasma flow, as is the case in the accretion column.

4.3 Previous Work

This experiment is part of a series of experiments known collectively as the *POLAR Project*, further details on the following experiment can be found in Falize et al. (99). Theoretical scaling work showed that such an accretion column was able to be simulated in the laboratory under the global similarity concept[*] (32). This work also defined a form for the height of the shock (or width of the cooling layer) which could be measured in the laboratory, and compared to the astrophysical case in equation (4.1) above.

$$h_s = \Xi \times v_s \times t_{cool} \tag{4.2}$$

where Ξ is a dimensionless constant parameter, v_s the incoming material velocity and t_{cool} is the post-shocked material cooling time.

The first experiments were carried out at the LULI2000 facility (103) at École Polytechnique in Paris, France. A similar target to the one shown above was used, though with a layer of aluminium or titanium taking the place of the pusher material. A 300 J in 1.5 ns square (temporal) laser pulse was focussed onto a 400 μm diameter

---

[*] Due to constraints on the regimes accessible on medium-sized laser facilities, the velocities and temperatures required for absolute similarity cannot be reached, although this is the ultimate aim of the project, and should be feasible on megajoule laser facilities such as NIF, (100), and LMJ, (101; 102).

spot on the ablator foil, giving an average intensity of ∼1×10^{14} W cm^{-2}. The metal foil was accelerated down the tube as a plasma, at velocities of the order of 100 km/s, and impacted onto a quartz obstacle. Optical diagnostics were used to diagnose the dynamics. On the rear surface VISAR (104) and streaked optical pyrometry [SOP] were used to time shock breakout in the quartz obstacle. Transverse interferometry, optical shadowgraphy (with a 532 nm probe beam) and SOP were used to image the incident flow and reverse shock. The set up can be seen in figure 4.6. Gated optical imagers [GOIs] were used for the interferometry and shadowgraphy, which had 120 ps resolution.

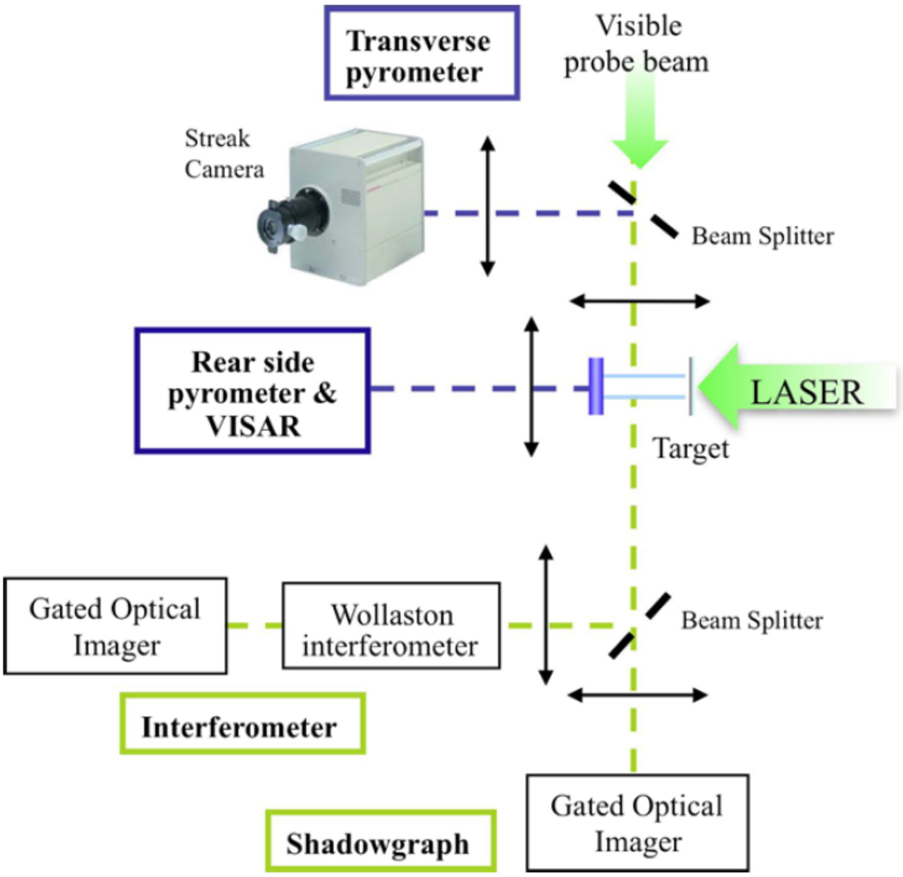

Figure 4.6: Schematic showing the experimental layout of the LULI2000 campaign. Orientation of transverse and optical diagnostic, and the laser, are shown, further details in the text. Image reproduced from Falize et. al (99)

4.3.1 Results

Two shadowgraphy images are shown in figure 4.7, at 5 ns after the end of the laser pulse. Whilst shadowgraphy can image the tube, it is relatively difficult to make out a plasma flow feature. If we take the opaque region to be the plasma flow – the probe beam is a low power 532 nm laser and so at the expected electron density of 10^{20} cm^{-3} it makes sense that the incoming flow would be opaque – and, by using the separation of this from the quartz obstacle, estimates of velocity are of the order of 50–60 km/s. However, looking at the SOP data in figure 4.8 the incoming flow appears to hit the obstacle at 8 ns after laser firing, which gives a velocity nearer 120 km/s. The difference is explained by what is actually measured in each case: the SOP uses the emissive region of the plasma, which at the leading edge is hotter, faster and less dense than the region probed by the optical laser. It is fair to say that in this regime that the bulk of the material is moving with the velocity measured in the shadowgraphy diagnostic.

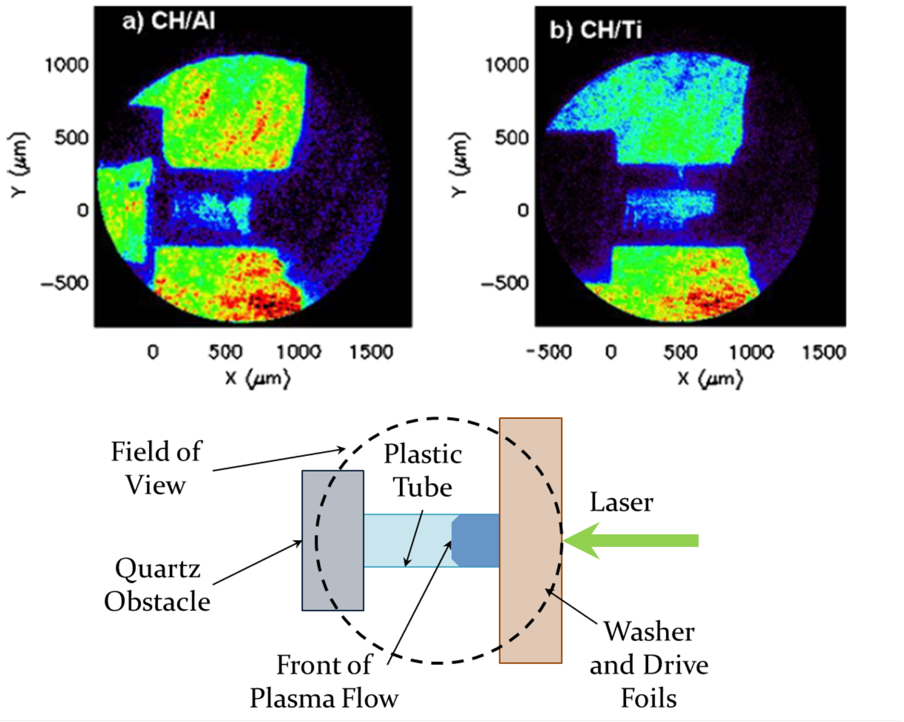

Figure 4.7: Showing optical shadowgraphy images for gold, a), and titanium, b), foils at 5 ns after laser firing. The x-axis origin is the start of the quartz obstacle. Underneath is a schematic showing the position of the target within each shadowgraph. Image modified from Falize et. al (99).

The region of interest was the reverse shock feature in front of the quartz obstacle. However, as figure 4.7 suggests, the incoming plasma flow is already opaque to the probe beam, and thus imaging a shock within this flow is impossible. Further complications arise when looking at the SOP in figure 4.8: after impact, ∼8 ns, there appears to be little emission, until much later at ∼30 ns. One might expect that the shock, being hotter, should emit optical light, but this is not seen. This could be because the incoming plasma becomes optically thick as it densifies, or that the plastic tube itself becomes opaque upon heating. End-on SOP, not shown here, shows optical emission at ∼30 ns outside of the quartz obstacle, which also suggests that plasma outside of the tube could be emitting and causing the second streak in figure 4.8.

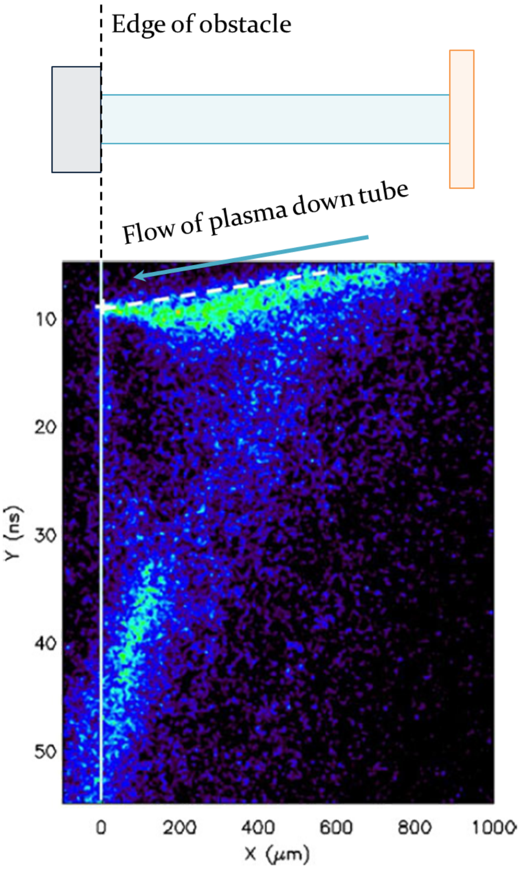

Figure 4.8: Showing the SOP image for titanium pusher, with schematic of the target overlaid. The laser comes in from right to left, and the dashed white line shows the incoming plasma flow, with a measured flow of ∼120 km/s. The x-axis origin is at the quartz obstacle (shown as the solid white line), the y-axis origin is the laser firing. Image modified from Falize et. al (99).

4.3.2 Looking Forward

The LULI experiment gave interesting results which matched with simulated values for the velocity of the incoming flow, but the all other results from the diagnostics were inconclusive. The shadowgraphy was not able to measure the reverse shock feature, and the SOP was unable to show emission within the tube at late time. As well, the experiment failed to reach the regime necessary for comparison to the astrophysical case. This was particularly due to the low incoming flow velocity, which subsequently lead to a low post-shock temperature.

The Orion experiment was designed to build upon the foundations of the LULI experiment, but to better reach the regime for astrophysical comparison, and to improve the imaging of the experimental features required.

4.4 Orion Experimental Set-Up

The experiment was carried out on the Orion laser facility (87), AWE's replacement for the HELEN laser, which has been operational since 2013. As part of its remit 15 % of experimental time is allocated to academic access, of which 4 weeks were given for this experiment.

The laser beams from the Orion facility are arranged in two cones (see Fig. 4.9), which we refer to as 'drive' and 'backlighter'. The drive cone consisted of five beams, which illuminated the target in a 100° cone angle, with each beam supplying ∼400 J (2 kJ in total) in 1 ns onto a 600 μm spot, which gave an average intensity of 7.0×10^{14} W cm^{-2}. For the backlighter cone, we used two laser beams of total energy 150 J, in 500 ps onto a 500 μm spot, which gave an average intensity of 1.5×10^{14} W cm^{-2}. Both sets of beams were delivered at the third harmonic with a wavelength of 351 nm. The drive beams were used to produce an expanding plasma jet, while the backlighter beams generated an X-ray source which imaged the plasma flow and the reverse shock formation.

4.5 Instrumentation and Diagnostics

The same general form of diagnostics used in the previous experiment was kept for the Orion experiment. It was still of importance to image the reverse shock feature, and also to look at the incoming flow of plasma in order to determine a velocity. However; certain modifications were made to mitigate some of the challenges faced previously: namely the shadowgraphy was changed from optical to X-ray to allow for greater penetration of the plasma flow (which was expected to be even denser due to target design and laser properties) and whole target optical emission imaging was used to determine the source of emission seen in the SOP.

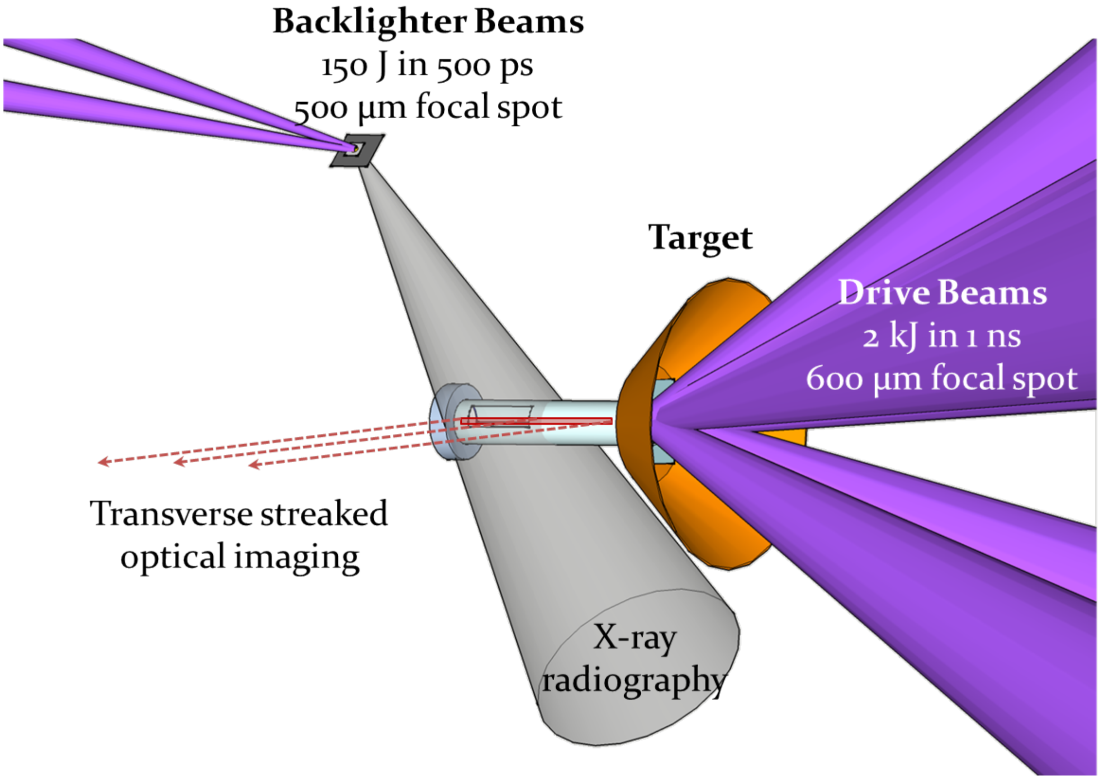

Figure 4.9: Schematic of the experimental set up. Five drive beams were incident on one end of the main target. Two other beams were focussed onto the backlighter target, producing X-rays for use in radiography. Optical self emission is imaged along the tube axis.

4.5.1 X-ray Radiography

4.5.1.1 Choice of X-ray Energy

The energy of the backlighter X-rays was chosen to allow for the best contrast between the reverse shock and the incoming flow. While the incoming flow was expected to be somewhat denser than in the previous experiment, the move from an optical to X-ray probe means a much larger proportion of the flux will pass through the plasma. As low as possible energy X-ray backlighter was wanted, but one that would still pass through the plastic without being attenuated greatly, which ruled out elements lower than Aluminium. (When referring to the energy of a backlighter we generally consider the He-α line emission, which was expected to be the strongest contribution to the emitted radiation upon illumination of the target element by a long pulse laser.)

A series of simulations were run to determine expected X-ray transmission for different backlighter energies. A 1D simulation of the experiment was run using the HELIOS code (105), which was then post-processed with the SPECT3D code (106). (As this used a 1D simulation, it was not possible to include the effect of the tube wall. Thus X-ray energies were chosen that weren't significantly absorbed by the plastic, as determined by cold opacities from the CXRO database (107).) Chlorine, Scandium and Titanium, which have He-α energies of 2.78 keV, 4.32 keV and 4.75 keV respectively, were trialled. Chlorine appeared the most promising from the point of view of contrast, and so was chosen as the main backlighter target, but some Scandium and Titanium targets were also made.

4.5.1.2 X-ray Target and Diagnostic

A secondary target was used as an X-ray source for backlit pinhole radiography of the reverse shock region. This target consisted of a 400 μm diameter, 6 μm thick, chlorinated plastic (parylene-D) foil which was then affixed onto a 50 μm CH foil, and finally placed onto a large tantalum foil with a 15 μm pinhole, which can be seen in figure 4.10. On earlier targets the plastic and tantalum were separated by 500 μm by a mount. This was to stop any closure of the tantalum pinhole by a shock travelling through the target before X-rays had been emitted. Later targets, however, mounted the plastic foil directly onto the tantalum, with no noticeable drop in measured X-ray intensity on the image plate. This target was placed 14.1 mm from the steel obstacle and illuminated by the backlighter beams (see Figure 4.11). (For the Scandium and Titanium backlighters, this material replaced the chlorinated plastic, with thicknesses of 25 and 5 μm respectively.)

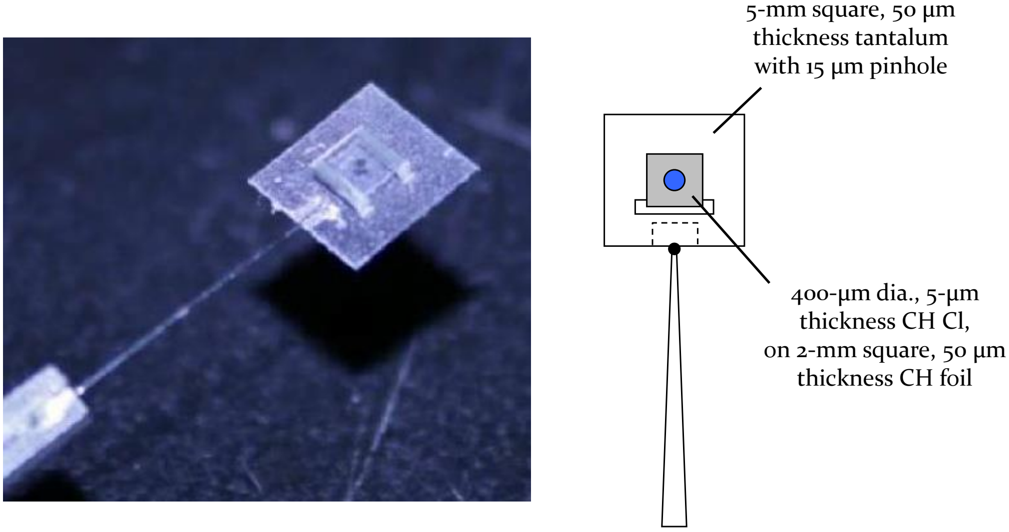

Figure 4.10: Image, reproduced from Spindloe et al. (98), and schematic of the X-ray backlighter target. The plastic foil, with the X-ray producing material affixed on top, is here shown mounted 500 µm from the tantalum pinhole.

For the backlighter cone, two laser beams of total energy 150 J, in 500 ps onto a 500 µm spot were used, giving an average intensity of 1.5×10^{14} W cm^{-2}, delivered at the third harmonic with a wavelength of 351 nm. In order to minimise motion blurring, but still have sufficient signal to noise ratio, we chose the pulse length of 500 ps. Initially a 200 ps pulse was used, but as we could increase the energy by moving to a longer pulse, and the timescale of the experiment was happening over many tens of nanoseconds, we found increasing the pulse length led to greater signal with little to no motion blurring. (If we consider the plasma to be moving around a speed of 100 km/s – greater than expected around the reverse shock feature – in 500 ps it will have moved ∼50 µm, which is approaching the resolution limit of the X-ray radiograph ∼20 µm.) The energy of the X-rays were expected to be mainly from Cl line emission: i.e., He-α at 2.78 keV, He-β at 3.27 keV, Ly-α at 2.96 keV and Ly-β at 3.50 keV.

The backlighter beams overfilled the target, with a focal spot of 500 µm, which caused an expansion of the surrounding plastic, as well as the target material. This acted to contain the blow-off and the tantalum pinhole ensured a point-like source of X-rays, which backlit the main target and were recorded on an image plate detector placed 229 mm from the main target (108). This gave a field of view of ∼2 mm and a magnification of ∼15×.

The image plate was housed inside a open shutter camera, an adaptation of the

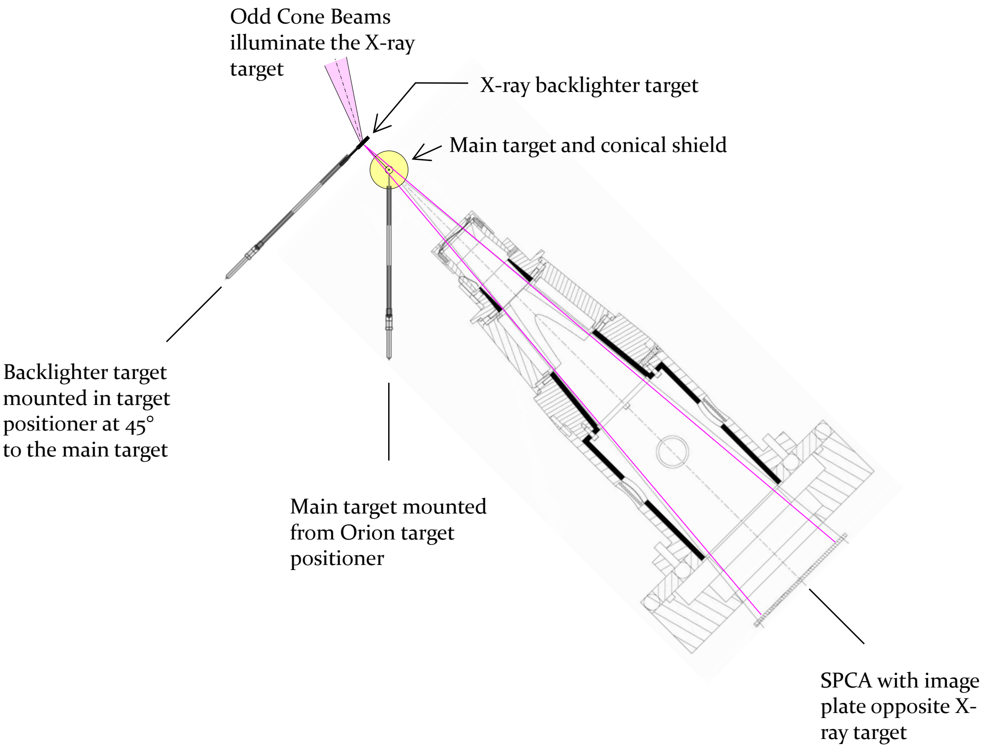

Figure 4.11: Schematic of X-ray diagnostic. The main target is mounted centrally, with the X-ray target mounted off to one side at a 45° angle above the horizontal plane. The open shutter, pinhole camera is opposite the X-ray target, at a 45° angle below the horizontal plane. Two of the odd cone of lasers illuminate the X-ray target, with all five beams of the even cone driving the main target.

SPCA diagnostic (43) previously fielded on the Omega laser. The camera consisted of a 191 mm long metal housing, with a 42 mm diameter image plane detector area. At the end closest to the target a nose cone was fitted, with space for filters, which was designed to restrict the field of view of the image plate to just the area of interest of the target, and to shield it from emission from the blow off plasma from the drive. While initial data were good, a slight double image[†] can be seen, and so between experimental runs the nose cone was redesigned so it was longer, and placed nearer the target. (Previously the end of the nose cone was 20 mm from the target, whereas it changed to be 10 mm). This allowed for better screening of other X-ray sources and removed the double image seen in earlier images.

For the majority of shots the same filters were used. Just behind the nose cone appropriate filters were added: a 12.5 μm PVDC to cut off lower energies, and 5

[†] The source of the double image was considered to be from blow-off plasma from the backlighter target.

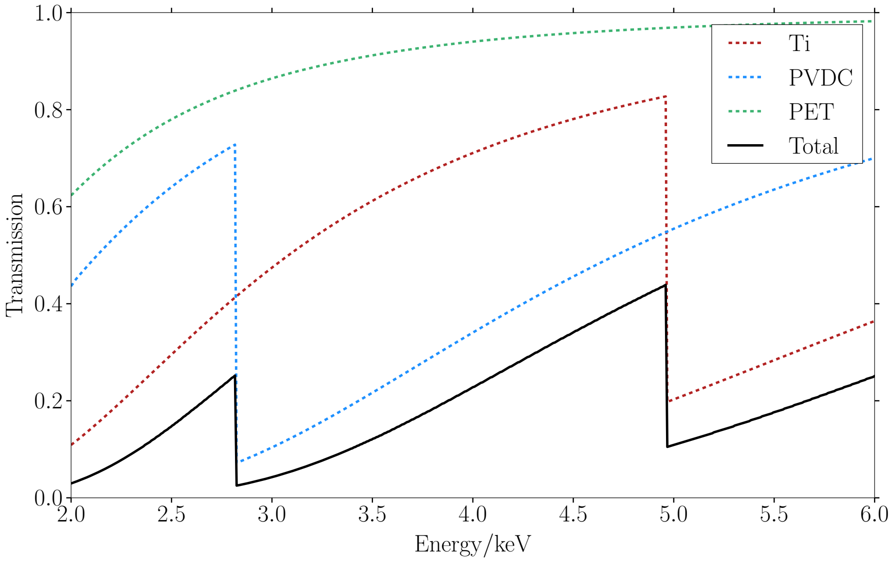

Figure 4.12: Showing the transmission of X-rays through the filters. Nose cone filters of 5 µm of titanium and 12.5 µm PVDC are shown in red and blue respectively. The 8 µm aluminised mylar around the image plate itself is shown here as PET in green. The total of all filters is shown in solid black.

µm Ti to cut off higher energies, giving an effective window of transmission between 2.78 and 5 keV, as can be seen in figure 4.12. Covering the image plate itself was 8 µm thick mylar with a thin coating of aluminium, to shield the image plate from UV/visible light. A step-wedge filter of 50, 100 and 150 µm thick plastic was also placed over the image plate to calibrate the X-ray emission energy on each shot. (The result of this will be discussed in the section 4.6 below.)

4.5.2 Optical Emission

All optical diagnostics, with the exception of VISAR, measured the self-emission of the plasma in the visible, thus being passive imaging. The first run of the experiment fielded a streak camera, SOP, along the target, and an end-on VISAR. However; the VISAR failed to pick up a signal of shock breakout in the quartz (which we put down to the quartz being too thick causing the shock breakout time to be much longer than the experimental timescale). The VISAR diagnostic was then changed to end-on SOP, and, finally, transverse SOP with a different sweep window in time, and different optical filters. For the second run of the experiment the transverse SOP was fielded alongside a framing camera which was sufficiently demagnified to allow for an image of the whole target. Both of these diagnostics used the same optical line, which was split outside the chamber and directed to each camera. Details of these two diagnostics are given below.

4.5.3 Streak Camera

Emitted optical light from the plasma was collected by an imaging line payload in one of the TIMs (ten-inch manipulators) attached to the target chamber and sent down a relay system to an optical table where the streak camera was set up. The streak camera had a spatial field of view of ∼4 mm, and so the entire tube and obstacle were visible, except the region shielded by the copper cone. The imaging line aligned with the central axis of the tube (along the slit cut-out in the tube), in the horizontal plane and was streaked in time over ∼60, 100 or 250 ns as required. This provided a temporal dependence of the plasma flow thus allowing us to calculate velocities. (For the few shots that also fielded end-on streak imaging the same set up as here was used, except that the optical line was orientated across the tube.)

The streak camera itself was sensitive to blue light, with filters in place to block out laser light (and any of the second harmonic unconverted laser light).

4.5.4 Framing Camera

The framing camera used the same optical line as the streak camera above though with a lower magnification, and thus allowed the entire target to be imaged. The field of view was > 4 mm, with an expected spatial resolution of ∼50 μm. Eight frames, time-integrated over 2 to 5 ns, with 0 and 5 ns delay between frames, were taken on each shot. These images helped to explain sources of emission seen in the streaked data.

4.6 Results

4.6.1 Optical

Figures 4.13, 4.15 & 4.16 show examples of the optical streak records for various shots. The same general form is found when using the brominated plastic pusher, figure 4.13, or gold-plastic pusher, figure 4.15. In figure 4.16 the target was rotated such that the slits through the tube were aligned with the optical diagnostics. This allowed us to see inside the tube without attenuation from the tube wall (and also to confirm that light was coming from the plasma inside rather than from the tube itself.) As a consequence of this there is a marked increase in signal from ∼2,200 μm.

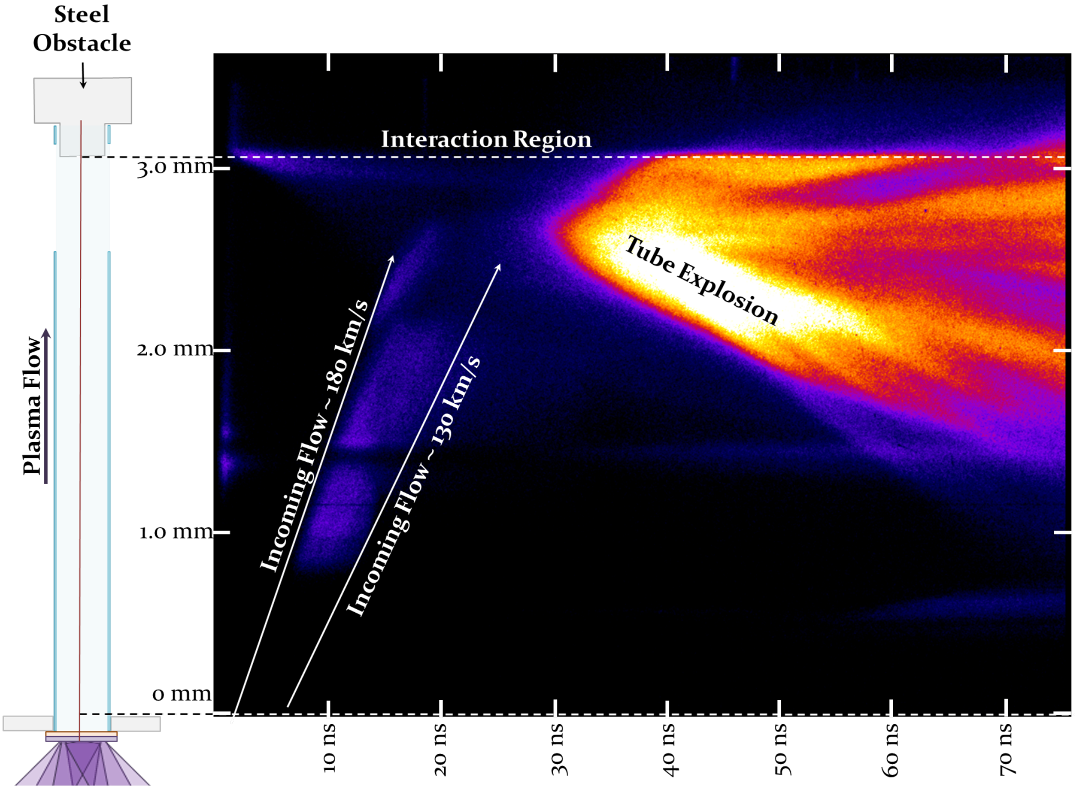

Figure 4.13: Showing the optical streak record of a brominated plastic pusher. A schematic of the target is shown on the left, showing the spatial positions of the obstacle and the start of the streaked image. Time runs from left to right and distance from top to bottom. The distance starts from the end of the copper cone, not from the start of the tube. The leading and trailing edges of the incoming flow are shown, with velocities of 180 km/s and 130 km/s respectively. This is the same shot as the 40 ns delay in figure 4.18.

From the optical streak records we can determine the incoming flow velocity, and also look for the return flow and shock. As we see from figure 4.13 material flows down the tube, starting from the bottom left, towards the obstacle at ∼3 mm. There are a few features of interest here. Firstly, we can see the incoming flow spread out spatially, as a result of the expansion and acceleration of the pusher. This leads to a hot, low density leading edge which flows down the tube at around ∼180 km/s. The trailing edge of the flow moves slower, around 130 km/s, and the time of impact with the obstacle is separated by at least 10 ns. Sufficient material must build up around the obstacle to increase the pressure to the point when a reverse shock is formed. Unfortunately this pressure is somewhat relieved by lateral explosion of the tube, which is heated enough to begin to emit. This is shown as the very bright, symmetric, region in figure 4.13 starting at 30 ns. Another interesting feature is the

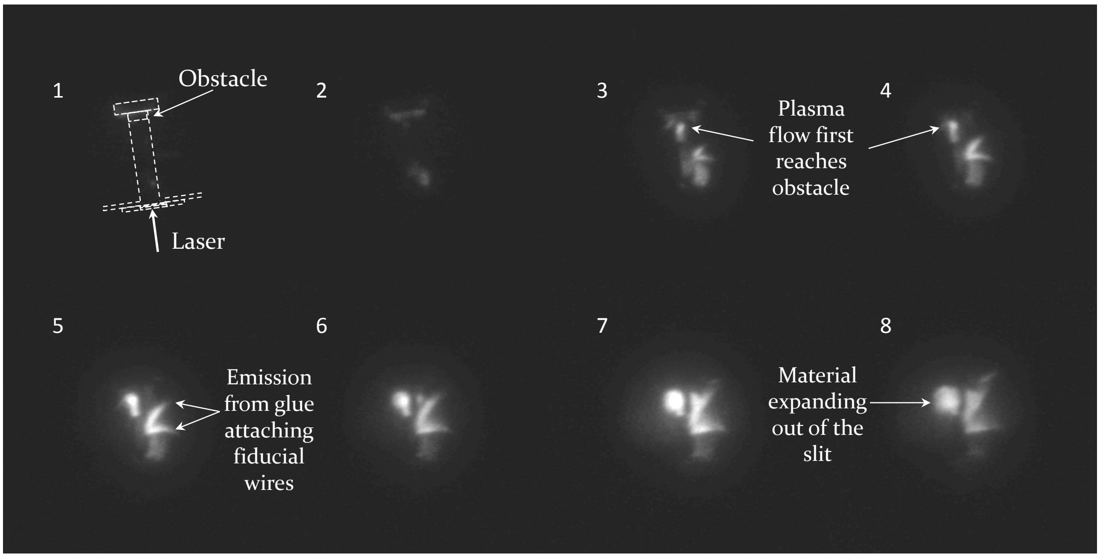

Figure 4.14: Showing eight optical self emission images taken with the framing camera. Each image has an exposure time of 3 ns, with no delay between frames. At early time flow can be seen coming down the tube, and in later frames we see increased emission from the obstacle out of the slits, and side emission, thought to be from glue present to hold position fiducials in place. A sketch of the tube is overlaid in frame 1.

movement of a flow from the obstacle up the tube, as seen in the top left corner. This occurs very soon after the drive beams are fired, and suggests there is some fast heating of material. The streak record is unable to show whether the source of this is inside or outside the tube.

While the framing camera by itself is not of much quantitative use for this experiment, it is of great help when used alongside the streak records to determine whether sources of light are coming from inside or outside of the tube, i.e. true signal from the plasma flow, or a side effect of the laser interaction. The unusual emission from near the obstacle moving up the tube at early time, as seen in figure 4.13 starting top left, can also be seen in the framing camera images. Figure 4.14 shows 8 frames, of 3 ns exposure time, with the sequence starting shortly after the drive lasers were fired. In the first couple of frames we can clearly see emission from the obstacle itself, and thus the feature in the streak record is not from inside the tube (which agrees with the observation that it has no effect on the trajectory of the incoming flow).[‡]

[‡] The reason for this emission is unknown, but it is thought to be because of the laser-plasma interaction of the drive lasers with the ablator. It would be unusual for laser light to be able to propagate through the plastic foils, though it is possible that a low amount of laser energy outside the focal spot passed through the plastic washer holding the cone and tube together, and heated the surface of the obstacle. More likely is that the laser interaction with the ablator heated it sufficiently

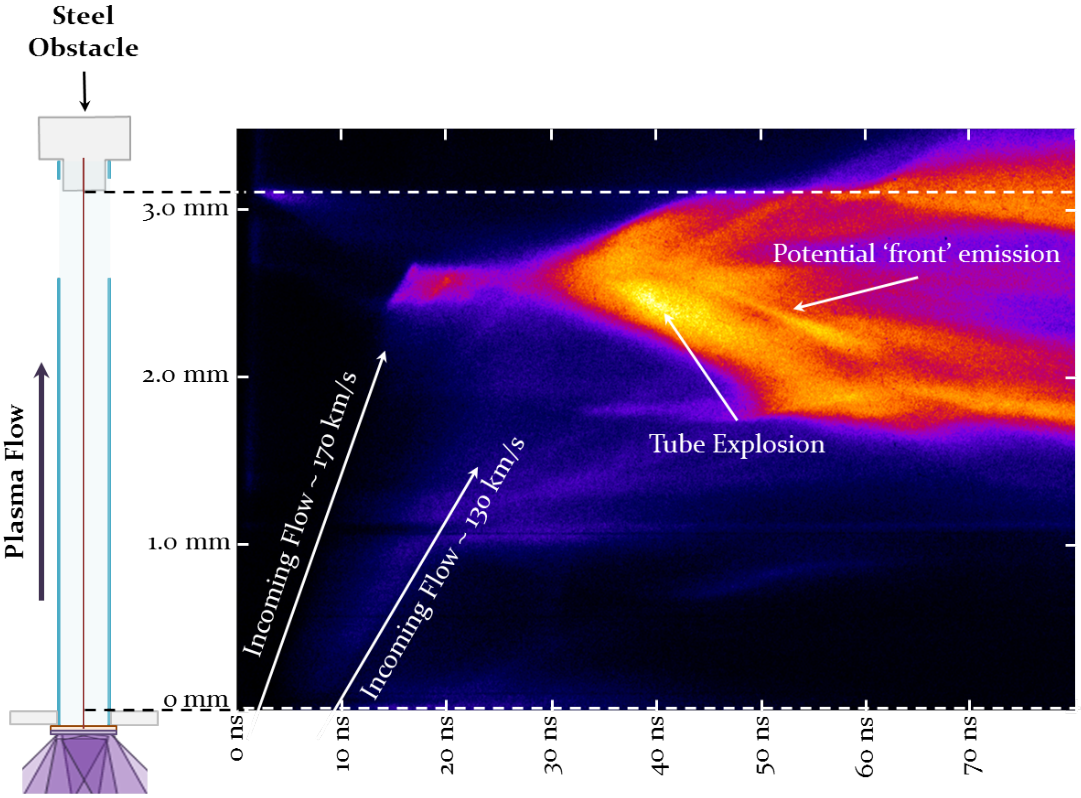

Figure 4.15: Showing optical streak record of a gold-plastic pusher. Target schematic is shown on the left, overlaid with positions in the streaked image. Time runs from left to right and distance from top to bottom. The distance starts from the end of the copper cone, not from the start of the tube. The leading and trailing edges of the flow are shown, with velocities of 170 km/s and 130 km/s respectively. A potential 'shock' feature emitting light is labelled.

In frame 3 we begin to see emission near the obstacle, through the slits in the tube, as well as flow down the tube itself. There is also significant emission from outside the tube in frames 3–8, which we believe is emission from glue holding position fiducials in place. In the standard orientation, the streak camera line of site runs along the centre of the tube axis, and therefore it does not see inside the tube at the slit, nor did it see the emission from the glue which was off axis.

Figure 4.15 shows a typical optical streak record for a gold-plastic pusher target. As with the brominated plastic targets, we see similar features of an incoming flow, interacting with the obstacle and then tube explosion from ∼30 ns. The slight difference between the brominated and gold-plastic pushers seems to be in the incoming

---

to begin to emit X-rays which travelled straight down the tube, but were blocked by the copper cone outside of this angle.

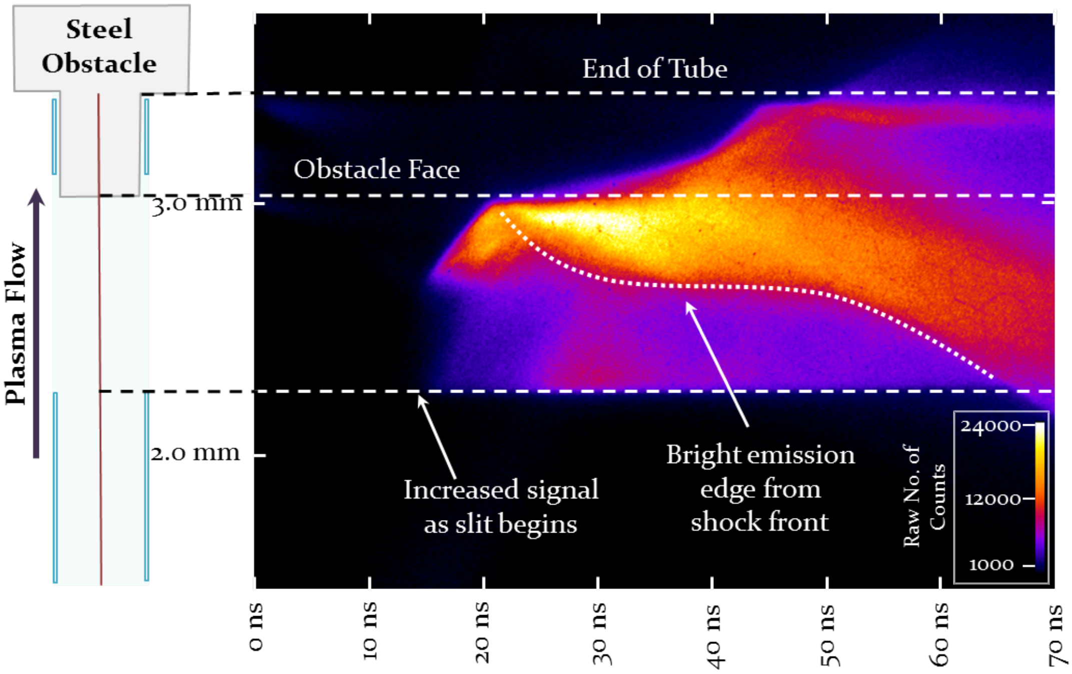

Figure 4.16: Showing optical streak record of a gold-plastic pusher. A schematic of the target is place alongside, aligned with the streaked image position. In this case the slits in the tube were facing towards the optical diagnostics. The dashed horizontal lines shows the edge of the slits, hence the increase in signal beyond this point, and the face of the obstacle and end of the tube. The dotted line shows the leading edge of a bright feature returning from the edge of the tube: thought to be from the reverse shock.

flow velocity, which leads to later features taking slightly longer to appear with the gold targets. The leading edge of the incoming flow for bromine varied between ∼195 – 250 km/s, compared to ∼170 – 230 km/s for the gold targets. The flow velocity is dependent on the laser energy, which fluctuated for different shots, which explains the range of values for each target type.

There is a slight line feature in figure 4.15 starting at ∼45 ns, ∼2.5 mm within the tube explosion region which appears to separate from the tube explosion emission. It is, however, very difficult to state this with any certainty purely from this image. To alleviate the issue of tube explosion emission, figure 4.16 shows the optical streak record when the tube was rotated so that the slits in the tube faced the optical diagnostics. Emission within the tube is much brighter – the edge of the slits can be clearly seen and is marked with a dashed white line at ∼2.2 mm – and features around the obstacle are easier to see. In particular a boundary in signal, highlighted by the

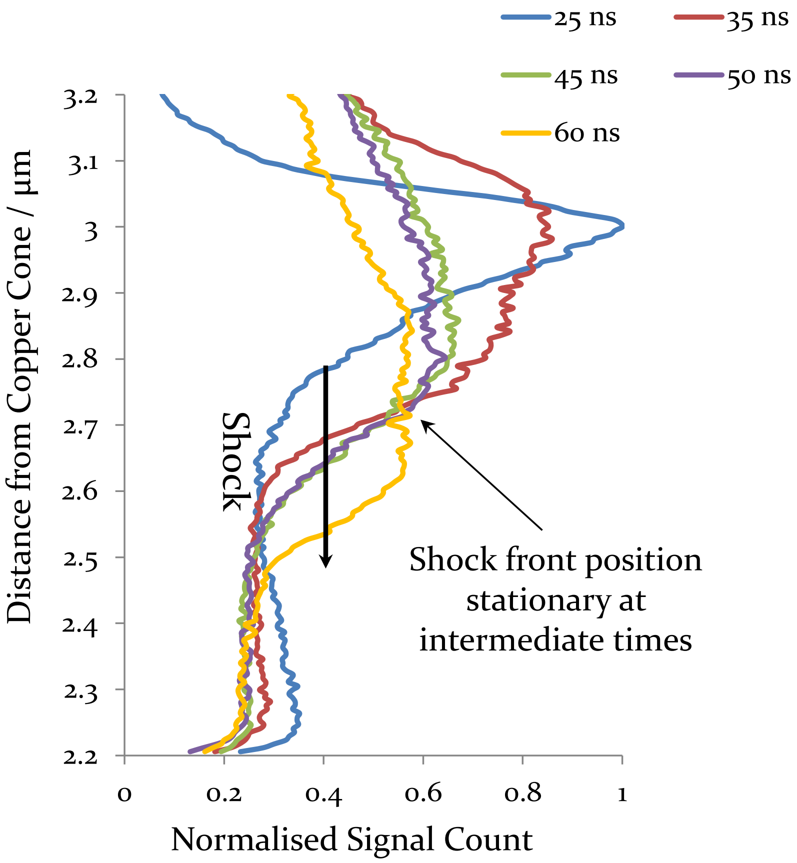

Figure 4.17: Showing line outs of figure 4.16 in position at different times. The lines are normalised to the maximum signal count recorded. The edge of the brightening position overlaps at 35, 45 and 50 ns.

dotted white line, can be seen, which we consider to be the reverse shock surface. This line is drawn by eye, but the position of the emission was determined using lineouts which can be seen in figure 4.17. As the reverse shock passes through the plasma it heats the material behind it, causing greater emission. It appears to move in the laboratory frame between 20-30 ns, and then remain stationary until 50 ns when it again begins to move. Much of this movement can be explained by the density profile of the incoming plasma. The leading edge of the plasma flow is of lower density, with a gradient up to a bulk density, and so the shock moves up the tube until it reaches this bulk. The shock then moves through the flow at the same speed, but opposite direction, as the incoming flow, thus appearing stationary in the laboratory frame. Towards the end of the spatial extent of incoming flow, the density drops off, causing the shock to accelerate. This stationary feature is interesting to compare to the X-ray images, section 4.6.3, as well as to the astrophysical case, section 4.7.

The optical streak images show similar features for each shot taken: there is a high degree of reproducibility between shots. The incoming flow velocity is dependent on the laser energy, which fluctuated around 2.0 kJ over the course of the experiment.

4.6.2 X-ray Radiographs

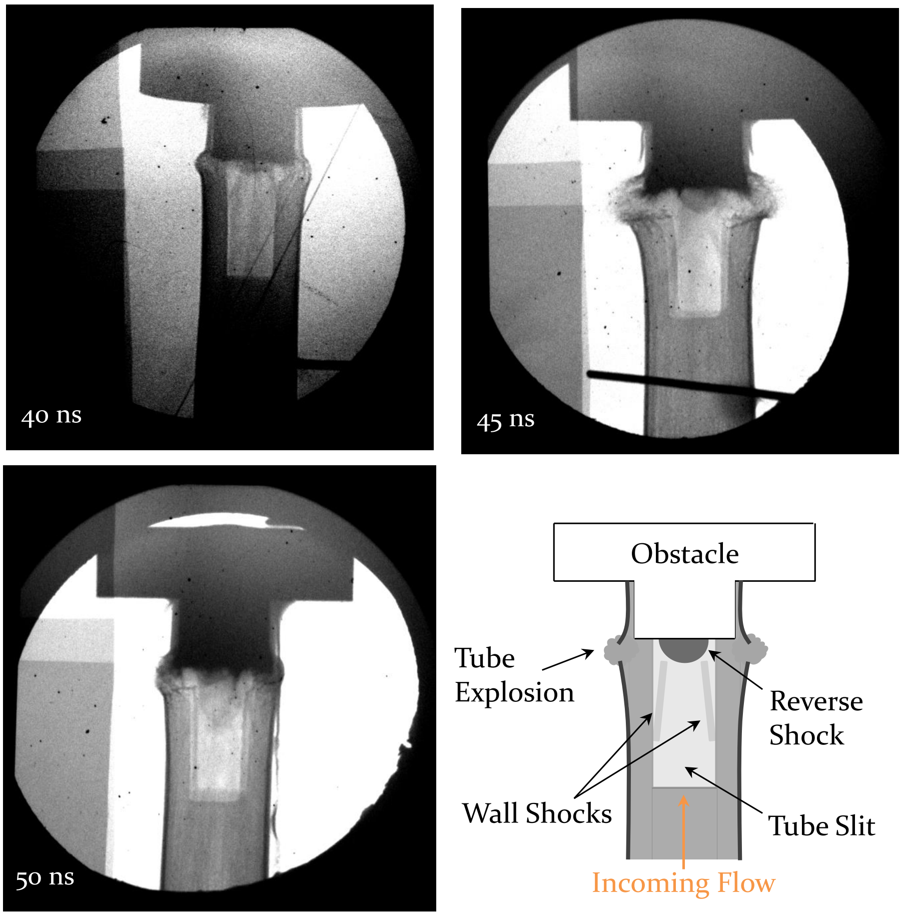

Figure 4.18: Showing a time sequence of X-ray radiographs with a brominated plastic pusher. The reverse shock feature is somewhat diffuse, but can be seen to be moving in time. The schematic in the bottom right labels the main features seen in the radiographs.

Figure 4.18 shows a sequence of X-ray radiographs at different times for a brominated plastic pusher. The main features of these X-rays can be seen in the schematic in the bottom right. At the earliest time we can see the beginnings of a densification in the flow, by a small, dark feature just ahead of the obstacle, which is the beginning of the reverse shock. This is accompanied by diagonal side features, which are less dark than the main feature, but darker than the incoming flow. These features we call wall shocks. Such features have been seen in other shock tube experiments, where they were caused by either radiation from the shock front (109), or preheat from the laser-target interaction in the form of X-rays or hot electrons (110; 111), ablating the inside of the tube and launching a shock wave back into the tube. The source of these shocks in our experiment could either be preheat from the initial interaction, or radiation from the reverse shock/post-shock material. These become harder to see as time progresses.

The reverse shock feature can be seen to move up the tube in time, but becomes quite diffuse by 50 ns. If we take a lineout along the central axis of the tube, and adjust the signal to be that of transmission rather than raw intensity, we can see the jump in transmission at the shock front. Figure 4.19 shows this for the 45 ns delay bromine radiograph above. Transmission is reduced by ∼1.5 times at the shock compared to the incoming flow. (Later it is discussed how this transmission can be related to a density, under certain assumptions.)

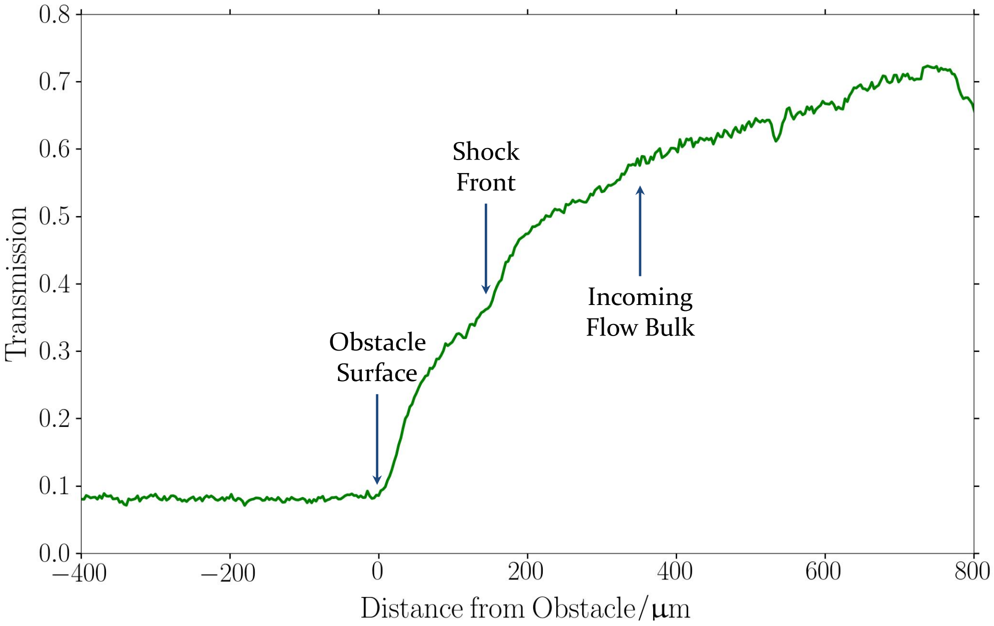

Figure 4.19: Showing a central axis lineout of the 45 ns Bromine pusher, X-ray radiograph from figure 4.18. The jump in transmission, at ∼170 µm from the obstacle, can be clearly seen.

Two X-ray radiographs with the gold-plastic targets are shown in figure 4.20. These targets had a 200 nm layer of aluminium coating the entire inner surface of the cone and the resulting radiographs show a much clearer separation of features, compared to the the bromine radiographs in figure 4.18, and other gold-plastic radiographs, which also show reproducible features.[§] The features are also cylindrically symmetric, as a result of choosing a laser spot larger than the tube radius: small offsets still allow an even 'push' on the material, reducing three-dimensional effects which would further complicate analysis.

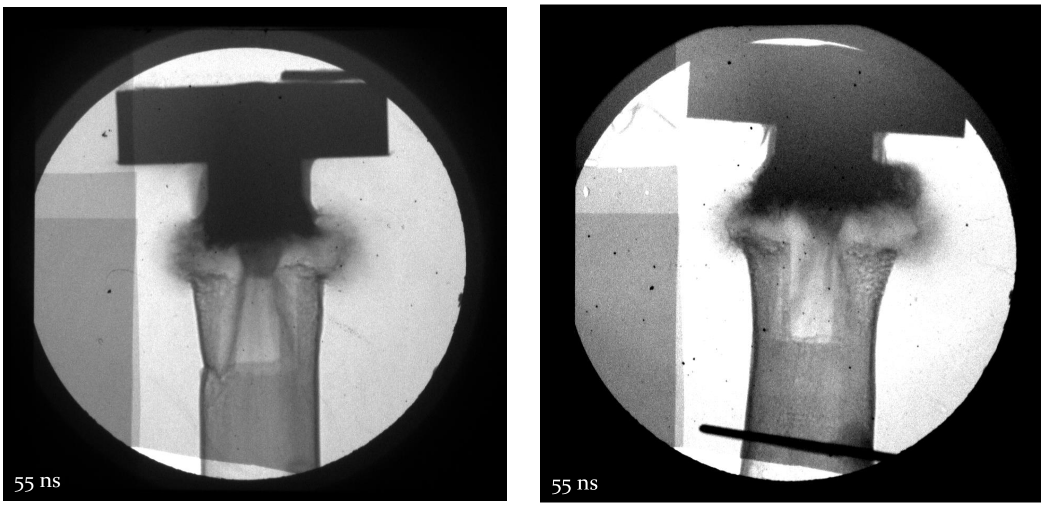

Figure 4.20: Showing two X-ray radiographs of gold-plastic pusher targets at 55 ns after lasers have fired. Compared to the bromine shots, figure 4.18, the features are much better defined. We can easily see the region of reverse shock by the obstacle (the flow comes in from the bottom). The agreement between the two images is testament to the repeatability of the experiment.

As the radiograph shows, we have a region of dense material, a discontinuity in transmission, and the incoming flow, bounded by wall shocks. By taking a lineout down the central axis we can determine the difference in the transmission across the shock front, which, from figure 4.21, is about half that of the incoming flow at the shock front.

Under the following assumptions, we can use the transmission to infer a compression ratio:

1. The gold-plastic layers are uniformly mixed,
2. The total opacity is simply a weighted sum of the individual opacities,
3. We know the energy of the backlighter.

[§] A 200 nm 'flash' of aluminium is unlikely to cause any significant effect on the hydrodynamics. The reason for this marked increase in feature clarity is thus attributed to the aluminium blocking light at early times and reducing the effect of preheat.

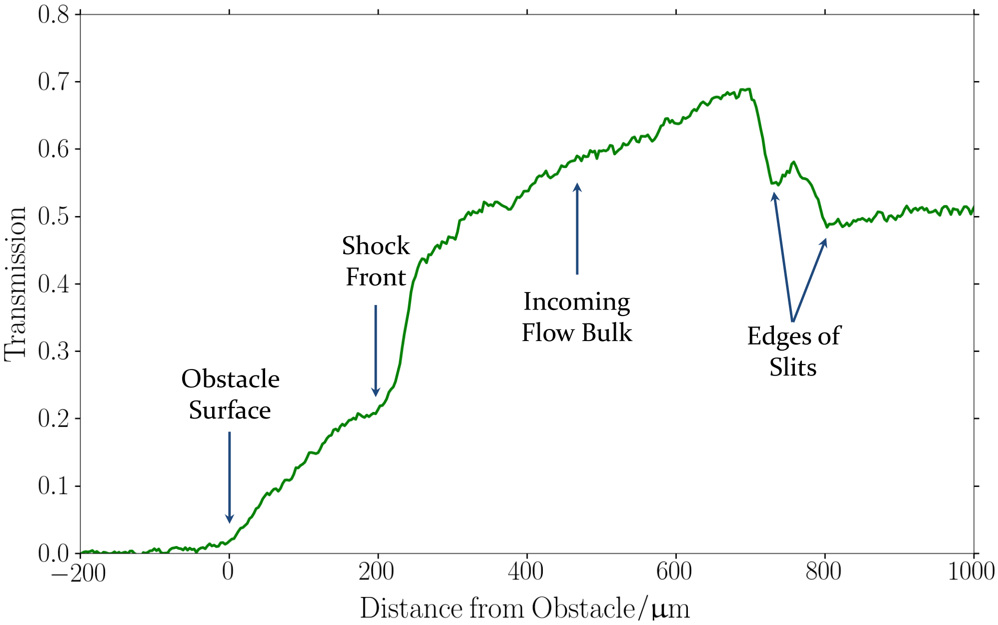

Figure 4.21: Showing lineout along the central axis of the lefthand gold-plastic radiograph of figure 4.20. The obstacle position and shock front are marked. Where the edges of the two slits do not quite overlap, we see steps in transmission.

Discussing these in turn, the gold-plastic targets were formed of multiple layers of alternating plastic and gold. With the different densities of the two, it was expected that the boundaries would become Rayleigh-Taylor unstable and would be sufficiently heated and mixed in the time taken for the plasma to flow down the tube and impact onto the obstacle. Simulations were performed by P. Graham which showed significant mixing at early time, 2 ns, which grew to give a very high degree of mixing after 8 ns. If roughness at the boundaries is higher – which is likely as a result of the production process – then the mixing is even greater. As it takes longer than 20 ns for the plasma to reach the end of the tube, we are confident that the plasma is sufficiently mixed that the assumption of uniform mixing is true.

Under the assumption of uniform mixing, we know the proportion of each element in the plasma in the region of interest. Gold and plastic have different opacities, and while they are in the plasma state it is likely that the opacity does not depend greatly on the interaction between the two.

The energy of the backlighter is the most important. While we expected the He-α line, 2.78 keV, in chlorine to be dominant, we included a step wedge filter (three known thicknesses of plastic overlaid in the corner of each image plate), which can be seen in all radiograph images, as a check for the energy. The step in transmission in the region where the slits do not quite overlap, seen in figure 4.21 at 730 and 800 µm, also acts as a second check. From the step wedge filters, using cold opacities for the plastic step wedge from the CXRO database (107), we can plot expected transmission for different backlighter energies against the experimental data, shown in figure 4.22. Here the data suggest that the transmission is more consistent with a backlighter energy of 3.5 keV than the expected 2.78 keV from the He-α line. While there is a Ly-β line in chlorine at 3.5 keV, it is likely that the emission has a Bremsstrahlung component, peaking at 3.5 keV, which is cut off by our choice of filters in the range from 2.78 – 5 keV.¶ Taking 3.5 keV as the backlighter energy (either as a single source from line emission, or as the peak in a Bremsstrahlung distribution) fits the step wedge filter well, and also agrees with the observed transmission drop through the misaligned tube slits.

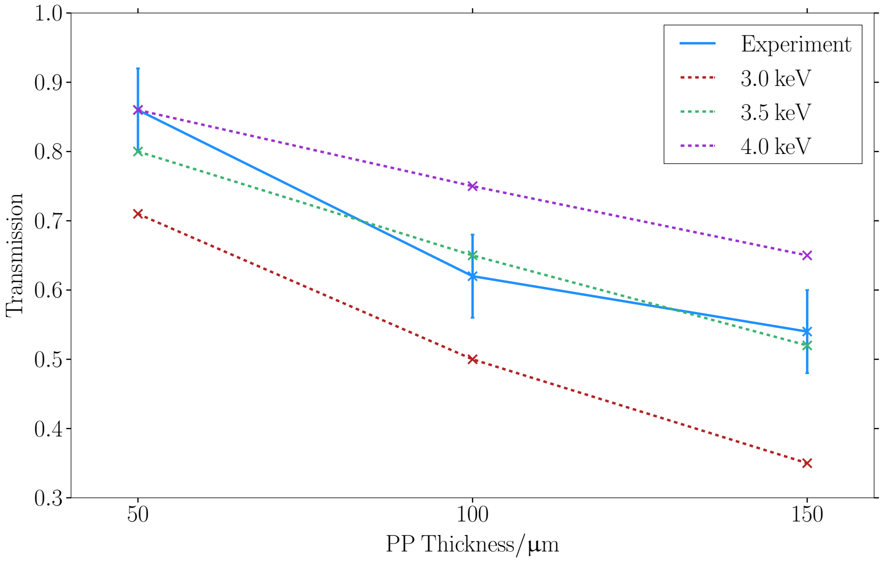

Figure 4.22: Showing the expected transmission through varying thicknesses of plastic step wedge for different X-ray energies. The transmission from the experiment is overlaid, with error bars given by the uncertainty in determining the initial intensity. The experiment most closely agrees with a backlighter energy of 3.5 keV.

From these assumptions, we calculate from the transmission in figure 4.21, a compression ratio in the reverse shock between the upstream and downstream flows to be of the order of ~5.3 ± 0.6 at $t = 55$ ns (where the error comes from allowing the backlighter energy to vary in a range from 3 to 4 keV).

¶An attempt to fit the transmission to a simple model of He-α line emission sitting on top of hard X-ray emission (that effectively passes straight through the target and filters) ($I_{signal} = I_{hard} + I_{He-\alpha} \exp(-\rho\kappa\ell)$) was made, but this failed to reproduce the experimental results.

4.6.3 Consistency of Results

If we now compare the optical and X-ray results, we see consistency between the two diagnostics. Figure 4.24 shows the optical streak records overlaid with an X-ray radiograph. The time at which the X-ray image was recorded is marked on the optical streak.

There is very good agreement relating to positions of the main target features, such as the obstacle and slit positions. The region of brightening in the optical streak, as highlighted in figure 4.16, matches in position to the shock front in the X-ray radiograph.

Similar comparisons of the X-ray and optical diagnostics at early time (<20 ns) were not performed, as the density was not sufficient to appreciably see anything in the X-ray images. At times greater than 45 ns we see similar agreement, though this is complicated by the more diffuse nature of the shock feature without use of the 200 nm flash of aluminium.

Qualitative agreement can been seen between the framing, figure 4.14, and streak, figure 4.13, where the framing camera shows a bright ‘plug’ of material heading down the tube over a series of 3–4 frames (from frame 2), which is consistent with the time frame of $\sim$15 ns from the optical streak record.

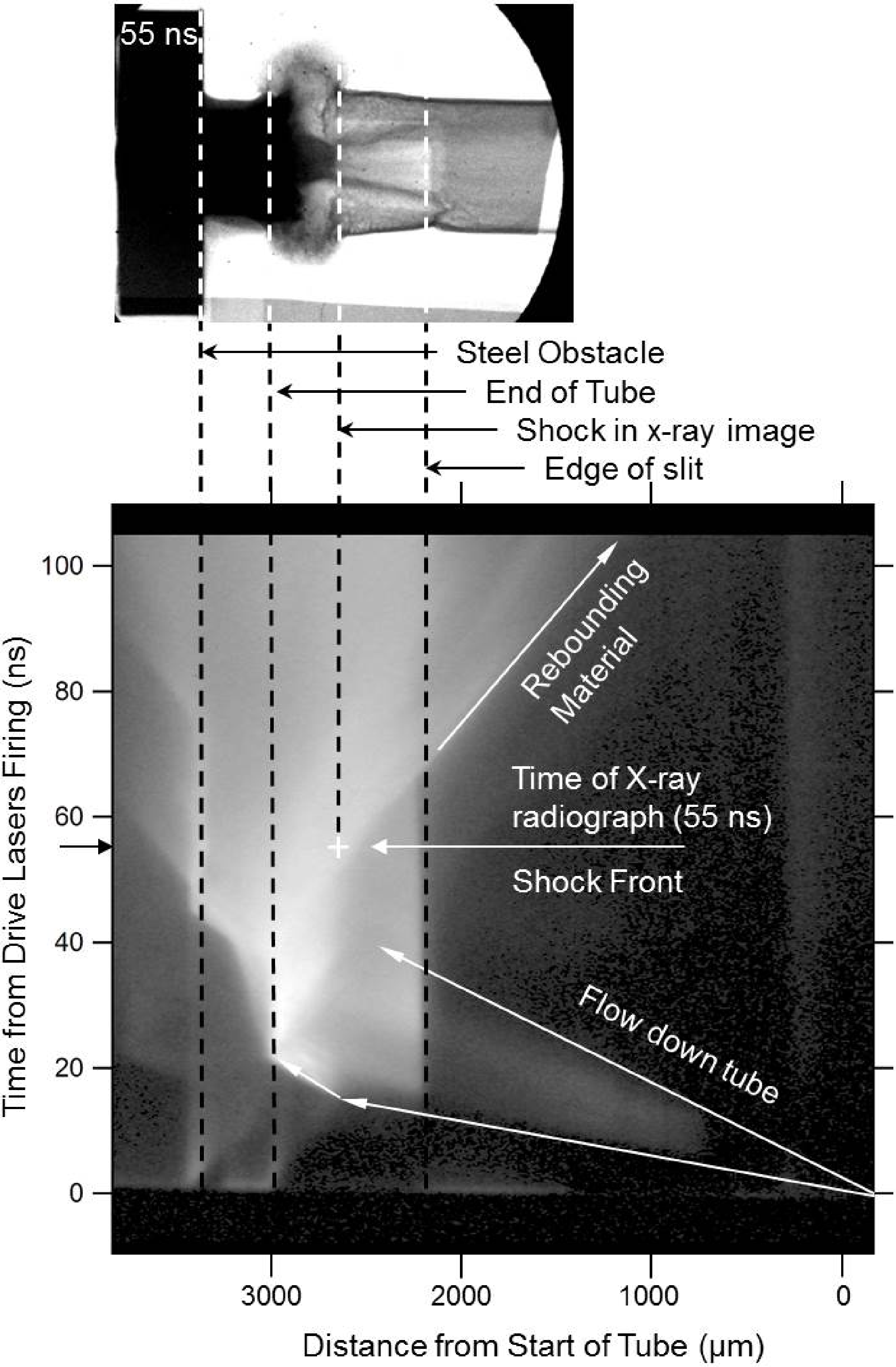

Figure 4.23: Streaked optical data for a shot. Time runs from bottom to top, distance right to left, on the bottom panel. The time evolution of the plasma can clearly be seen inside the tube. The dotted lines and overlaid radiograph show positions of parts of the target on the streaked image.

4.7 Comparison to Simulation

The experimental package was modelled by P. Graham in two stages using a different two dimensional (2D) radiation-hydrodynamic code for each stage. The NYM Lagrangian code (112) was used for the laser-interaction phase since this allowed fine zoning of the ablator foil which is essential to resolve light absorption from inverse bremsstrahlung. X-ray emission and absorption were simulated with full multi-group Monte Carlo photonics (113) utilising CASSANDRA opacities (114) and SESAME equations-of-state (115). After the laser pulse had ended and the coronal plasma had cooled substantially then the simulation was linked to the PETRA code (116) to continue to late time. This used Eulerian hydrodynamics (run on an orthogonal mesh), which is essential to permit the large shear flows of material along the tube walls. This calculation was restricted to multi-group diffusion for the X-ray exchange but the opacities and equations-of-state were unchanged from NYM. The laser was modelled as a 1 kJ beam normal to the surface and a super-gaussian spatial intensity profile with 1/e intensity at 300 μm radius. This gave an approximate intensity of 3.5×10^{14} W cm^{-2}, which is reasonable as the experimental beam angle was not modelled. An electron-conduction flux limiter of 0.05 was used, typical of laser-plasma modelling at this irradiance level.

The simulations were subsequently post-processed to generate synthetic radiographs of the interaction region. Figure 4.24 shows a comparison of simulated and experimental results. It is important to note here that the simulation was carried out *before* the experiment and thus their agreement is even more striking. Both images are quantitatively similar not only in the morphology of the flow structure – where the position of the reverse shock front is nearly identical – but also in the X-ray transmission values which are well matched. It is important to note that the plastic tube in the experiment had slits cut through it, near the obstacle, to improve contrast by allowing X-rays to go through only the plasma and not to be absorbed by the tube wall. We can see the slits were not exactly aligned by the step down in transmission $\lesssim$2,250 μm, and again at $\lesssim$2,200 μm. The predicted X-ray transmission was calculated with and without attenuation from the tube wall. The simulated transmission values without the tube wall are consistent with the experimental data near the reverse shock (that is, between 2,300 and 3,000 μm), while the simulated transmission with the tube wall included is closer to the data for distances $\lesssim$2,300 μm. The jump in the simulated transmission around 2100 μm, which is not seen in the experiment, results from the ablator plasma (which is more transparent to X-rays) immediately following the pusher plasma.

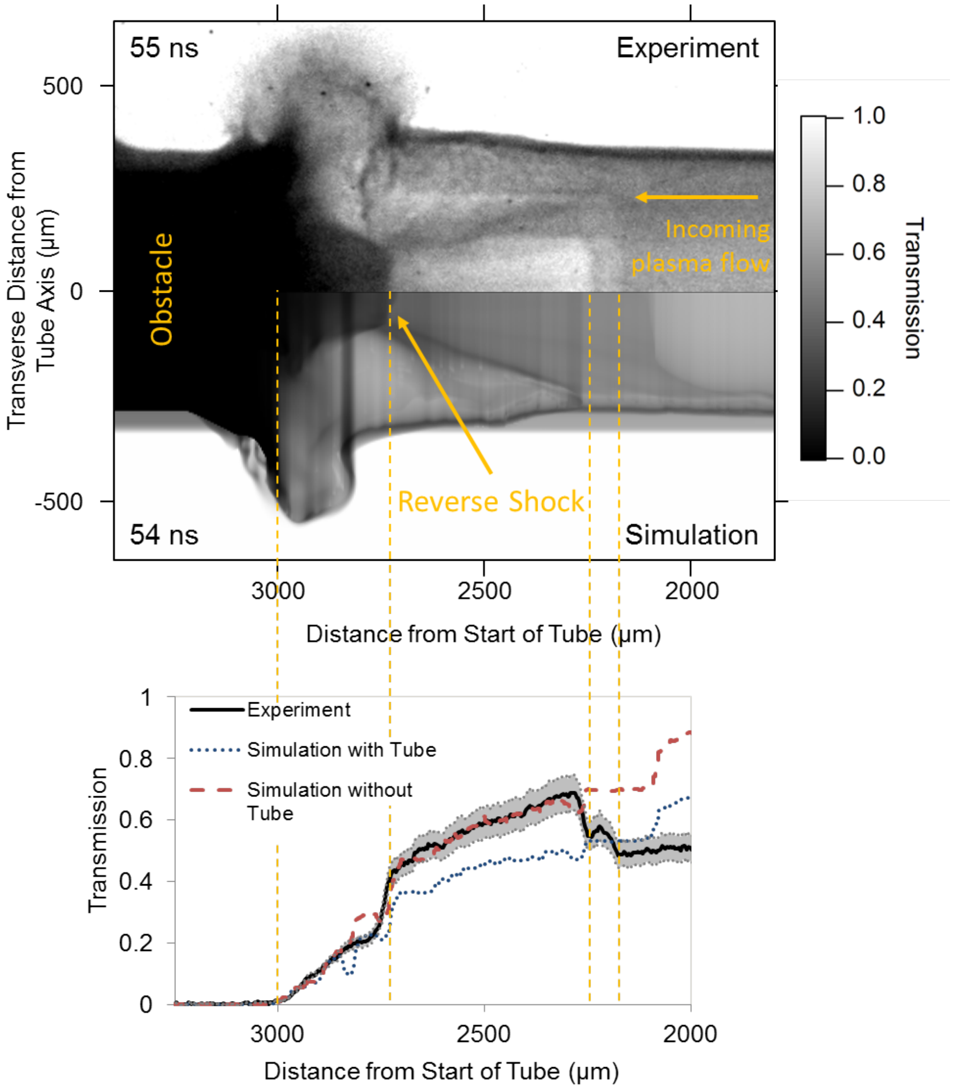

Figure 4.24: Comparison of an experimental radiograph, top, with a radiograph from post-processing a 2D simulation, bottom of top panel. The plasma flow enters from the right, and impacts onto the obstacle, originally around 3000 μm, and a reverse shock can be seen around 2750 μm. A line out of transmission along the central axis can be seen underneath.

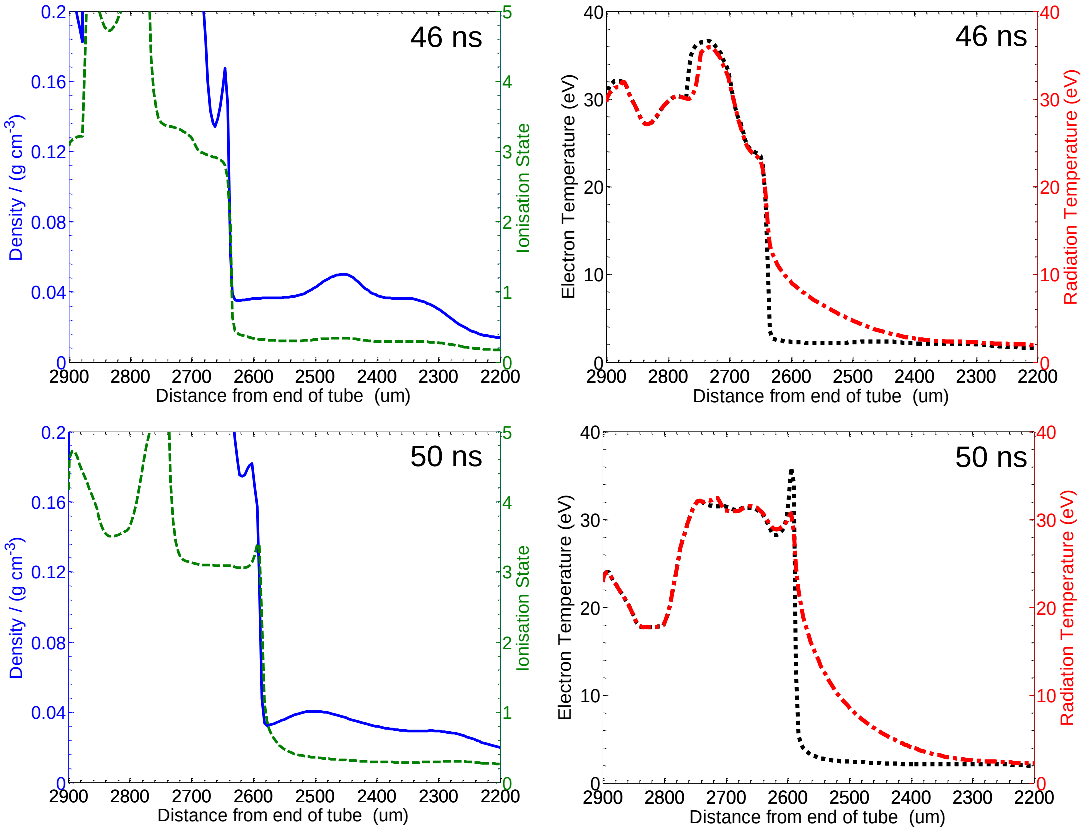

Figure 4.25: Simulated values for density and ionisation state (left panels) – solid blue and dashed green lines respectively – and electron temperature and radiation temperature (right panels) – dotted black and dot-dashed red lines respectively – are shown at two different times. Flow of material is from right to left, with the shock front seen at $\sim$ 2640 μm at 46 ns, and $\sim$ 2590 μm at 50 ns. We ignore effects at distances greater than $\sim$ 2700 μm as these involve material from the obstacle and are not just a result of the incoming flow.

Lineouts from the 2D simulations, along the central axis, can be seen in figure 4.25 for various plasma properties. In the left column we see density, blue, and ionisation state, green dashed, near the obstacle (where the obstacle position is originally at 3000 μm and the flow is moving from right to left.) In the region >∼2,700 μm we believe that the density/ionisation results are as a result of blowoff material from the obstacle itself, mixed with the flow, and therefore we do not use these to calculate jump properties. Instead, for example, for the lower left panel, the density ratio can be calculated from the graph by reading off at 2610 μm (0.176 g/cc) and 2580 μ (0.032 g/cc) which gives a ratio of 5.5. For the right hand columns we show electron temperature, black dot, and radiation temperature, red dot-dash. Here we define the radiation temperature from Drake (25): "The value of the temperature of an equilibrium thermodynamic system that would have the same mean energy as that of the actual system being described." Although this is strictly not a temperature, it is a useful value for characterising the radiation.

4.8 Discussion

Using the standard equations for the conservation of mass and momentum across the shock transition region, ignoring the radiation pressure term (which is negligible under these conditions), and writing the thermal pressure as $p_i = \rho_i(Z_i + 1)k_B T_i/m$, where ρ_i the mass density, Z_i the ionisation state, k_B the Boltzmann constant, T_i the temperature and m the average mass per particle ($i = 1$ for the upstream flow and $i = 2$ for the downstream plasma), then we obtain (38):

$$\frac{\rho_2}{\rho_1} = \frac{1}{2a_2^2}\left\{a_1^2 + u_1^2 \pm \left[\left(a_1^2 + u_1^2\right)^2 - 4a_2^2 u_1^2\right]^{1/2}\right\}, \tag{4.3}$$

with $a_i = \sqrt{p_i/\rho_i}$ the isothermal speed of sound, and u_1 the upstream flow velocity.

Equation 4.3 admits a solution only when $u_1 \geq u_R$ or $u_1 \leq u_D$, where the rarified and dense velocities, respectively, are defined as:

$$u_R = a_2 + \left(a_2^2 - a_1^2\right)^{1/2}, \tag{4.4a}$$

$$u_D = a_2 - \left(a_2^2 - a_1^2\right)^{1/2}. \tag{4.4b}$$

If u_1 is greater than u_R, then the flow is supersonic and it results in a compression of the downstream plasma. This requires us to take the positive root in equation 4.3. This is what is expected to occur in the reverse shocks occurring in both the cataclysmic variable star system as well as in our experiment. The scaling between the two systems is given in Table 1. Values for the incoming flow velocity are taken from our streaked optical data (e.g. figures 4.13 and 4.15), and sound speeds are calculated using simulated values for the temperature. By calculating the Reynolds number, table 4.1, we can see that it is large in the astrophysical system and in the laboratory. This indicates that viscous dissipation can be neglected. On the other hand, the thin radiation number – a measure of the incoming material energy flow compared to the radiation flux (1) – is very small in the astrophysical case, and by no means large in the laboratory. This implies that radiation losses cannot be ignored and they are important in determining the overall evolution of the flow. This is also reflected by the fact that the radiation cooling time (τ_c) is of the order of the characteristic dynamical time.

Using the simulated flow velocity ($u_1 \sim 83$ km/s in the frame of the shock), temperature and ionisation fraction (Figure 4.25) we can estimate, using Eq. 4.3, $\rho_2/\rho_1 \approx 5.7 \pm 0.6$, which is a value close to that inferred from the X-ray radiographs (where the error is calculated by allowing a 10 % variation in the simulated ionisation fraction and temperature when calculating the sound speeds). Equation 4.3 follows from the mass and momentum equations, and is thus not affected by details regarding to ionisation and radiation.

The compression ratio, in the strong shock limit (which applies in our experiment), is given by $\rho_2/\rho_1 = (\gamma+1)/(\gamma-1)$. If we now take the compression value as 5.3, from the experiment, we estimate, from the ideal jump condition, an effective $\gamma \approx 1.46^{+0.08}_{-0.05}$.

Instead if we calculate the adiabatic exponent, taken from the relation of the energy, density and pressure in the ideal case (58), we have $\gamma = 1 + p/\rho\epsilon = 1.4$ where ϵ is the internal energy, and values are taken from the simulation. This ratio agrees with the value of γ taken from the experiment. Ionisation of the material at the shock front thus causes a greater densification of the material. The presence of a spike in the simulated electron temperature at the shock front ($\sim 2590\mu$m in figure 4.25 at 50 ns) suggests the presence of radiative effects (58). Following the analysis by Keiter et al. (117) in determining whether the effects of radiation are important[‖], in our

---

[‖] This result comes about by requiring that the flux of ionising radiation from the shock front must exceed the incoming material flux to be able to form a radiative precursor. By equating the temperature to the shock velocity we can determine the minimum shock velocity for this requirement to be fulfilled.

system the flow and shock velocity must equal or exceed 83 km/s. It follows, from the experimental and simulated numbers, that we are just in this regime.

Characteristic quantity	**Astro**	**Lab**
Length	10^6 m	1.5×10^{-4} m
Incoming Flow Density	10^{-8} g/cm^3	0.03 g/cm^3
Initial Flow Velocity	1,000 km/s	200 km/s
Post Shock Temperature	10,000 eV	28 eV
Cooling time (τ_c)	1 s	3.8×10^{-9} s
Reynolds number	10^6	2.2×10^5
Radiation number (Thin)	10^{-16}	2.3
Mach Number	>10	8
u_R	1,000 km/s	57 km/s
u_D	0.5 km/s	0.55 km/s
Shock Height (h_s)	~1,300 km	200 μm

Table 4.1: Comparison of physical properties, and characteristic values (defined in (1)), between our experiment and the astrophysical case of a magnetic cataclysmicic variable star system, taken from (91).

4.9 Comparison to Astrophysics

In the astrophysical case, the stand-off position of the shock front with respect to the surface of the white dwarf is given by (118; 119)

$$h_s \approx \frac{u_1 \tau_c}{4}, \tag{4.5}$$

where u_1 is the incoming flow velocity to the shock front, and τ_c is the cooling time (31). This is true for Bremsstrahlung-dominated cooling, with radiative losses given in the form of a cooling function (120). As we can see from the optical streak image in Fig. 4.16, the reverse shock in the experiment appears to maintain a steady distance $h_s \approx 200$ μm from the obstacle between 40 ns $\lesssim t \lesssim$ 55 ns. This value is consistent with the prediction of Eq. 4.5, and it corresponds to a stand-off distance of 1,300 km for the magnetic cataclysmic variable system, which is the typical spatial extension as predicted by theory. In the astrophysical case this is mediated by the radiative losses against the incoming mass flux, and hence radiative effects are very important. However in the laboratory the radiative and material energy fluxes are of similar magnitude. Nevertheless this provides an important laboratory platform to investigate the physics of the accretion column near the white dwarf photosphere which is not currently accessible by observational techniques. A similar experiment to the one described here could be performed at LMJ or NIF to increase the radiative nature of the reverse shock, by increasing the incoming flow velocity by ∼2.5x, and comprehensively test how radiative losses affect the stand-off distance.

4.10 Summary

In this chapter the background, design and results of a laboratory astrophysics experiment have been described. The binary star system involving a highly magnetised white dwarf pulling material off its partner star was introduced, and the concept of creating a laboratory analogue was shown. Design of the experiment, guided by the astrophysical case and previous work, was discussed, and optical, X-ray diagnostics and target design were outlined. The experimental results were shown, from which measurements of flow velocity, density and fluid morphology were extracted. Self-consistency between diagnostics was shown, as well as good agreement between experiment and simulation, and experimental and theory. The experiment was designed to test theories of accretion, the differences of which are not able to be resolved via telescope, and results showed the expected stationary shock, where the shock distance from the impact surface matched that expected when scaled to the astrophysical case. This suggests that loss terms, in the form of radiation and ionisation, are of importance in the dynamics, which lends itself to future experiments at larger lasers facilities, to further confirm these effects. Work in this chapter is contained in an article submitted to Nature Communications.

Chapter 5

Density Fluctuations in the Highly Radiative Case

"Nature uses only the longest threads to weave her patterns, so each small piece of her fabric reveals the organisation of the entire tapestry."
– Richard Feynman

Derivation of the dynamic structure factor, an important parameter linking experimental and theoretical work in dense plasmas, is possible starting from hydrodynamic equations. In this chapter we discuss the inclusion of radiative effects by modifying the starting equations and a new form of the dynamic structure factor including radiative terms is derived. Such terms are shown to have an effect on the structure factor at temperatures greater than a few tens of eV, which suggests that its effect must be taken into consideration in such regimes.

5.1 Background Motivation

The warm dense matter [WDM] regime – characterised by strongly correlated ions, and degenerate electrons in a dense plasma state (42) – is found in astrophysical environments such as the core of Jovian planets (121), in white dwarves, and in the crust of neutron stars (122). Simulation and modelling of the dynamical behavior of WDM states, however, remains difficult, though there have been advances stemming from the availability of accurate laboratory data using high intensity lasers and pulsed power facilities (15; 51; 123), as well as newer computational approaches that allow density functional theory techniques to directly simulate the dynamics of thermal density fluctuations (124). In more practical terms, the understanding of the density fluctuations in WDM regimes also plays an important role in the quest for inertial fusion energy (125).

The fundamental thermodynamic quantity that describes the space and time dependent behavior of WDM is the dynamic structure factor [DSF], which is also proportional to the X-ray scattering cross section (41), and thus it can be measured experimentally.

The comparison between the experimental and calculated DSF provides an important tool for the validation of theoretical models, toward a comprehensive understanding of these systems (126).

5.2 Dynamic Structure Factor

The Dynamic Structure Factor [DSF], $S(\boldsymbol{k}, \omega)$, is formally defined as (42):

$$S(\boldsymbol{k}, \omega) = \frac{1}{2\pi N} \int e^{i\omega t} \langle \rho(\boldsymbol{k}, t) \rho(-\boldsymbol{k}, 0) \rangle dt, \tag{5.1}$$

which gives the response of a material to density fluctuations $\rho(\boldsymbol{k}, t)$ of wavevector $\boldsymbol{k}$, frequency ω, where N is the total number of particles, and $\langle \cdots \rangle$ represents an ensemble (or thermal) average.

Experimentally the scattered X-ray spectrum from a material is related to the dynamic structure factor by (41):

$$P_S(\boldsymbol{R}, \omega) d\Omega d\omega \propto \frac{P_0 r_0^2 d\Omega}{2\pi A} N d S(\boldsymbol{k}, \omega) d\omega \tag{5.2}$$

where P_S is the scattered power, at a detector position $\boldsymbol{R}$, from N electrons into a frequency interval, $d\omega$, and solid angle, $d\Omega$, P_0 is the incident X-ray power, r_0 is the classical electron radius, and A the area of plasma irradiated by X-rays.

This direct relation between the theoretically derived structure factor and experimentally measured X-ray spectrum allows for experimental validation of theories, or extraction of plasma properties from experimental results.

5.2.1 Hydrodynamic Regime

The case corresponding to hydrodynamic fluctuations is an important one. By hydrodynamic we consider ourselves in the regime where the spatial and temporal scales of the fluctuations are much larger than the mean particle separation and the mean time between collisions, respectively. This implies $k \to 0$, $\omega \to 0$. However, in practice, for hydrodynamics to be applicable, both the wavenumber and the frequency do not need to be negligibly small as long as the detailed kinetic behavior of the system can be ignored (127). The hydrodynamic description of density fluctuations is important because it can be solved analytically (40; 128). Indeed, the analytical results for the DSF in a dense viscous plasma are in very good agreement with molecular dynamics simulations (129). Thus we can use hydrodynamics as a starting point to then derive the DSF. As the dynamics of a system is fully described by such a density correlation function, we can use the hydrodynamic understanding to interpret fluid systems from the DSF.

5.2.2 Beyond Hydrodynamics

On the other hand, there are several astrophysical and laboratory conditions where viscous hydrodynamics (*i.e.*, the Navier-Stokes equation) may not be sufficient to capture all the relevant physical processes. This include, for example, the presence of dynamically strong magnetic fields, radiation transport as well as quantum effects (1; 63). The Orion experiment in the previous chapter also gives an example of such a phenomenon.

These other terms, as shown in chapter 3, can still be written in the same general form compatible with fluid dynamics, modifying the hydrodynamic equations. As the DSF can be derived from hydrodynamics, we can also investigate the inclusion of radiative effects on the DSF by changing the starting equations from those of hydrodynamics, to those of radiative hydrodynamics. Thus we can use the general framework of equations shown in chapter 3, considering only viscous and radiative terms, and apply the same procedure to analytically derive a modified form of the DSF for both optically thick and optically thin plasmas. We will show that, under certain conditions, radiation transport can induce significant changes in the dynamical response of the medium. This is particularly important since numerical calculations (either based on molecular dynamics or density functional theory) of the DSF in strongly radiating plasmas are not yet possible, due to very demanding computational effort.

5.3 General Equations for an Optically Thick Fluid

The equations for the conservation of mass, momentum and energy, as given in chapter 3, (1), but considering only viscous and radiative terms for an optically thick fluid (that is, a fluid where the mean free path of radiation is less than the spatial extent of the plasma) are given, respectively, by:

$$\frac{\partial \rho}{\partial t} + \nabla \cdot \rho \boldsymbol{u} = 0, \tag{5.3a}$$

$$\rho\left(\frac{\partial \boldsymbol{u}}{\partial t} + \boldsymbol{u}\cdot\nabla\boldsymbol{u}\right) = -\nabla p + \nabla\cdot\boldsymbol{\sigma}_\nu + f_{rad}, \tag{5.3b}$$

$$\begin{aligned}\rho\left(\frac{\partial \epsilon}{\partial t} + \boldsymbol{u}\cdot\nabla\epsilon\right) + \frac{\partial E_R}{\partial t} &= -p\cdot\nabla\boldsymbol{u} - f_{rad}\cdot\boldsymbol{u} \\ &- \nabla\cdot\left[\boldsymbol{F}_R + (p_R + E_R)\cdot\boldsymbol{u}\right] + \nabla\cdot\boldsymbol{\sigma}_\nu\cdot\boldsymbol{u} - \nabla\cdot\boldsymbol{q},\end{aligned} \tag{5.3c}$$

where ρ is the mass density, t is time, $\boldsymbol{u}$ the fluid velocity, p the pressure, $\boldsymbol{\sigma}_\nu$ the stress tensor, f_{rad} the radiation force on matter, ϵ the internal energy, $\boldsymbol{q}$ the heat flux, E_R the energy density of the radiation field, $\boldsymbol{F}_R$ the radiative energy flux, and p_R is the radiation pressure. If radiation transport is considered in the diffusive limit, the above quantities can be written as:

$$-\nabla p_R = f_{rad}; \quad \boldsymbol{F}_R = -\frac{16\sigma T^3}{3\kappa_R \rho}\nabla T$$

$$p_R = \frac{E_R}{3} = \frac{4\sigma T^4}{3c},$$

where σ is the Stefan Boltzmann constant, T the temperature, c is the adiabatic sound speed, κ_R is the Rosseland opacity, given the form $\kappa_R = \widetilde{\kappa_R}\rho^a T^b$ (1). Substituting these relations into 5.3, after some simplification (see Appendix B for details), we obtain:

$$\begin{aligned}\rho\left(\frac{\partial \boldsymbol{u}}{\partial t} + \boldsymbol{u}\cdot\nabla\boldsymbol{u}\right) &= -\left(\frac{c_0^2}{\gamma}\nabla\cdot\rho + \frac{c_0^2}{\gamma}\alpha_{T0}\rho\nabla T\right) \\ &+ \eta_1\left[\nabla^2\boldsymbol{u} + \nabla\left(\nabla\cdot\boldsymbol{u}\right)\right] + \eta_2\nabla\left(\nabla\cdot\boldsymbol{u}\right) - \frac{4\sigma}{3c}\nabla T^4,\end{aligned} \tag{5.5a}$$

$$\begin{aligned}\rho C_V\left(\frac{DT}{Dt} + \frac{\gamma-1}{\alpha_T}\nabla\cdot\boldsymbol{u}\right) + \frac{\partial}{\partial t}\left(\frac{4\sigma T^4}{c}\right) \\ = -\nabla\cdot\left(\frac{16\sigma T^4}{3c}\boldsymbol{u}\right) + \nabla\cdot\left(\frac{16\sigma T^3}{3\kappa_R\rho}\nabla T\right) \\ - \boldsymbol{u}\nabla\cdot\left(\frac{4\sigma T^4}{c}\right) + \nabla\cdot\boldsymbol{\sigma}_\nu\cdot\boldsymbol{u} - \nabla\cdot\boldsymbol{q}\end{aligned} \tag{5.5b}$$

where γ is the adiabatic index, $\eta_{1,2}$ are the first and second coefficients of dynamic viscosity, C_V the heat capacity at constant volume, α_T the coefficient of thermal expansion, and we use D/Dt as the material derivative, defined as $D/Dt = (\partial/\partial t + \boldsymbol{u}\cdot\nabla)$.

5.4 Fluctuations

We now proceed by linearising the above equations. We assume the system is at equilibrium at a density ρ_0, temperature T_0 and velocity $\boldsymbol{u}_0 = 0$. Small perturbations from the equilibrium are written as:

$$\delta\rho = \rho - \rho_0, \quad \delta T = T - T_0, \quad \delta\boldsymbol{u} = \boldsymbol{u},$$

which then allows us to rewrite 5.3a as:

$$\frac{\partial\rho_0}{\partial t} + \frac{\partial\delta\rho}{\partial t} + \nabla\cdot(\rho_0\boldsymbol{u}) + \nabla\cdot(\delta\rho\delta\boldsymbol{u}) = 0.$$

As we consider the fluctuations to be small we disregard fluctuation terms of order greater than one. Thus,

$$\frac{\partial\delta\rho}{\partial t} + \nabla\cdot(\rho_0\boldsymbol{u}) = 0. \tag{5.6a}$$

Similarly we can write the momentum and energy equations respectively as:

$$\rho_0\frac{\partial\boldsymbol{u}}{\partial t} = -\frac{c_0^2}{\gamma_0}\left(\nabla\delta\rho + \alpha_{T0}\rho_0\nabla\delta T\right) + \eta_{1_0}\left[\nabla^2\boldsymbol{u} + \nabla\left(\nabla\cdot\boldsymbol{u}\right)\right] + \eta_{2_0}\nabla\left(\nabla\cdot\boldsymbol{u}\right) - \frac{16\sigma T_0^3}{3c_0}\nabla\cdot\delta T, \tag{5.6b}$$

$$\left[\left(\frac{16\sigma T_0^3}{c_0\rho_0C_{V0}} + 1\right)\frac{\partial}{\partial t} - \left(\gamma_0\frac{\kappa_0}{\rho_0c_{V0}} + \frac{16\sigma T_0^3}{3\kappa_{R0}C_{V0}\rho_0^2}\right)\nabla^2\right]\delta T = -\nabla\cdot u\left(\frac{\gamma_0 - 1}{\alpha_{T0}} + \frac{16\sigma T_0^4}{3c_0\rho_0C_{V0}}\right). \tag{5.6c}$$

We have defined the equilibrium Rosseland opacity to be of the form $\kappa_{R0} = \widetilde{\kappa_R}\rho_0^aT_0^b$. Other terms with subscript 0 are calculated using the equilibrium values only, such as α_{T0} and C_{V0}. As obtaining these equations require a significant amount of algebraic manipulation further detail is given in Appendix B.

To solve equations 5.6 we take the space (Fourier) and time (Laplace) transform,

$$\widetilde{\delta x}_k(s) = \int_0^\infty \mathrm{d}t\, e^{-st}\int_{-\infty}^{+\infty}\mathrm{d}^3r\, e^{i\boldsymbol{k}\cdot\boldsymbol{r}}\,\delta x(\boldsymbol{r},t)$$

where x stands for ρ, T or v, the tilde indicates the transformed property, and $s = \varepsilon + i\omega$ is the complex Laplace variable. Following the method discussed in (130), we define our independent variables as ρ, $\boldsymbol{j^M} = \rho_0 \boldsymbol{u}$ and $g = \rho_0 \delta T$. This gives us the following equations:

$$s\widetilde{\delta\rho_k}(s) + i\boldsymbol{k} \cdot \boldsymbol{j^M}(s) = \delta\rho_k(0) \tag{5.7a}$$

$$(s + \nu_{l_0}k^2)\tilde{\boldsymbol{j}}^{\boldsymbol{M}}_{\boldsymbol{k}}(s) + \frac{c_0^2}{\gamma_0} i\boldsymbol{k}\widetilde{\delta\rho_k}(s) + i\boldsymbol{k}\left(\frac{c_0^2\alpha_{T0}}{\gamma_0} + \frac{16\sigma T_0^3}{3c_0\rho_0}\right)\tilde{g}_k(s) = \boldsymbol{j}^{\boldsymbol{M}}_{\boldsymbol{k}}(0) \tag{5.7b}$$

$$\begin{aligned}\left[\left(\frac{16\sigma T_0^3}{c_0\rho_0 C_{V0}} + 1\right)s + k^2\left(\gamma_0\chi_0 + \frac{16\sigma T_0^3}{3\kappa_R\rho_0^2 C_{V0}}\right)\right]\tilde{g}_k(s) \\ + i\boldsymbol{k}\left(\frac{\gamma_0 - 1}{\alpha_{T0}} + \frac{16\sigma T_0^4}{3c_0\rho_0 C_{V0}}\right)\cdot \boldsymbol{j}^{\boldsymbol{M}}_{\boldsymbol{k}}(s) = \left(\frac{16\sigma T_0^3}{c_0\rho_0 C_{V0}} + 1\right)g_k(0).\end{aligned} \tag{5.7c}$$

where $\nu_{l_0} = (2\eta_{1_0} + \eta_{2_0})/\rho_0$ is the longitudinal viscosity, and $\chi_0 = \kappa_0/\rho_0 C_{P0}$ is the thermal diffusivity (C_{P0} is the heat capacity at constant pressure). These equations can be solved for $\widetilde{\delta\rho_k}(s)$ (see the Appendix for details). Since terms involving cross-correlation of ρ and $\boldsymbol{j}$, or g, vanish, as they are all independent variables, the density-density correlation function is given by 5.8:

$$\frac{\langle\delta\rho_k^*(0)\widetilde{\delta\rho_k}(s)\rangle}{\langle\delta\rho_k^*(0)\delta\rho_k(0)\rangle} = \frac{\left(s + \nu_{l_0}k^2\right)\left(\Delta s + X_{Th}k^2\right) + k^2\left(\frac{c_0^2\alpha_{T0}}{\gamma_0} + 16T_{Th}\right)\left(\frac{\gamma_0 - 1}{\alpha_{T0}} + \frac{16T_{Th}T_0}{C_{V0}}\right)}{s\left[(s + \nu_{l_0}k^2)(\Delta s + X_{Th}k^2) + k^2\left(\frac{c_0^2\alpha_{T0}}{\gamma_0} + 16T_{Th}\right)\left(\frac{\gamma_0 - 1}{\alpha_{T0}} + \frac{16T_{Th}T_0}{C_{V0}}\right)\right] + \frac{(c_0k)^2}{\gamma_0}(\Delta s + X_{Th}k^2)}, \tag{5.8}$$

where $S(k) = \langle\delta\rho_k^*(0)\delta\rho_k(0)\rangle$ is the static structure factor. Here we have defined:

$$\Delta = 1 + \frac{16\sigma T_0^3}{c_0\rho_0 C_{V0}}; \quad T_{Th} = \frac{\sigma T_0^3}{3c_0\rho_0}$$

$$X_{Th} = \gamma_0\chi_0 + \frac{16\sigma T_0^3}{3\kappa_{R0}\rho_0^2 C_{V0}}$$

The dynamic structure factor is then obtained by taking the limit

$$\frac{S(k,\omega)}{S(k)} = 2\Re\left(\lim_{\varepsilon\to 0}\frac{\langle\delta\rho_k^*(0)\widetilde{\delta\rho_k}(s = \varepsilon + i\omega)\rangle}{\langle\delta\rho_k^*(0)\delta\rho_k(0)\rangle}\right) \tag{5.10}$$

This can be separated into partial fractions which have a similar form to the pure hydrodynamic case (as seen below in equation (5.16b)) – in the limit of small k – which gives the dynamic structure factor over the static structure factor:

$$\frac{S(k,\omega)}{S(k)} = \left[1 - \frac{1}{\gamma_0}\left(\frac{\Delta c_0 k}{C_Q}\right)^2\right] \frac{2\xi_Q X_{Th} k^2}{\left(X_{Th}k^2\right)^2 + \omega^2}$$
$$+ \frac{1}{\gamma_0}\left(\frac{\Delta c_0 k}{C_Q}\right)^2 \left\{ \frac{\Gamma_R k^2}{(\Gamma_R k^2)^2 + \left[\omega + \left(\frac{C_Q}{\sqrt{\Delta}}\right)\right]^2} + \frac{\Gamma_R k^2}{(\Gamma_R k^2)^2 + \left[\omega - \left(\frac{C_Q}{\sqrt{\Delta}}\right)\right]^2} \right\}, \quad (5.11)$$

where we have defined:

$$C_Q^2 = \frac{c_0^2 k^2}{\gamma_0}\left((\gamma_0 - 1) + \Delta + \frac{16 T_{Th} T_0 \alpha_{T0}}{C_{V0}}\right) + k^2\left(\frac{16 T_{Th}(\gamma_0 - 1)}{\alpha_{T0}} + \frac{256 T_{Th}^2 T_0}{C_{V0}}\right);$$

$$\xi_Q = \frac{c_0^2 k^2}{\gamma_0}\frac{1}{C_Q^2}; \quad \Gamma_R = \frac{X_{Th}\left(\frac{1}{\Delta} - \xi_Q\right) + \nu_{\ell_0} k^2}{2}.$$

5.5 General Equations for an Optically Thin Fluid

We follow the same general form as previously, but now for an optically thin fluid (that is, a fluid where the mean free path of radiation is far greater than the spatial extent of the plasma) (1). The equations are:

$$\frac{\partial \rho}{\partial t} + \nabla \cdot \rho \boldsymbol{u} = 0, \quad (5.12a)$$

$$\rho\left(\frac{\partial \boldsymbol{u}}{\partial t} + \boldsymbol{u} \cdot \nabla \boldsymbol{u}\right) = -\nabla p + \nabla \cdot \boldsymbol{\sigma}_\nu, \quad (5.12b)$$

$$\rho\left(\frac{\partial \epsilon}{\partial t} + \boldsymbol{u} \cdot \nabla \epsilon\right) = -p \nabla \cdot \boldsymbol{u} + \nabla \cdot \boldsymbol{\sigma}_\nu \cdot \boldsymbol{u} - \nabla \cdot \boldsymbol{q} - L_\Lambda, \quad (5.12c)$$

where radiative losses are treated as a cooling function, L_Λ, using the following parametrization:

$$L_\Lambda \sim \rho \kappa_P \sigma T^4,$$

where κ_P is the Planck mean opacity (which we give the form $\kappa_P = \widetilde{\kappa_P}\rho^a T^b(1)$).

We now proceed by linearising the above equations. We assume the system is at equilibrium with small perturbations from the equilibrium written as for the optically thick case ($\delta\rho = \rho - \rho_0$, $\delta T = T - T_0$, $\delta\boldsymbol{u} = \boldsymbol{u}$):

$$\frac{\partial\delta\rho}{\partial t} + \nabla\cdot(\rho_0\boldsymbol{u}) = 0, \tag{5.13a}$$

$$\rho_0\frac{\partial\boldsymbol{u}}{\partial t} = -\frac{c_0^2}{\gamma_0}\left(\nabla\cdot\delta\rho + \alpha_{T0}\rho_0\nabla\delta T\right) + \eta_{1_0}\left[\nabla^2\boldsymbol{u} + \nabla\left(\nabla\cdot\boldsymbol{u}\right)\right] + \eta_{2_0}\nabla\left(\nabla\cdot\boldsymbol{u}\right), \tag{5.13b}$$

$$\begin{aligned}\left[\frac{\partial}{\partial t} - \frac{\kappa_0}{C_{V0}\rho_0}\nabla^2 + (b+4)\frac{\kappa_{P0}\rho_0}{C_{V0}}\sigma T_0^3\right]\delta T + \frac{\gamma_0 - 1}{\alpha_{T0}}\nabla\cdot\boldsymbol{u}& \\ = -\frac{\kappa_{P0}\sigma}{\rho_0 C_{V0}}\left[\rho_0 T_0^4 + (a+1)T_0^4\delta\rho\right],&\end{aligned} \tag{5.13c}$$

where we have also defined the equilibrium Planck opacity to be of the form $\kappa_{P0} = \widetilde{\kappa_P}\rho_0^a T_0^b$ similarly to the optically thick case.

Taking our independent variables as ρ, $\boldsymbol{j^M} = \rho_0\boldsymbol{u}$ and $g = \rho_0\delta T$, and Laplace and Fourier transforming equation (5.13) gives:

$$s\widetilde{\delta\rho}_k(s) + i\boldsymbol{k}\cdot\boldsymbol{j^M}(s) = \delta\rho_k(0) \tag{5.14a}$$

$$(s + \nu_{l_0}k^2)\tilde{\boldsymbol{j}}_{\boldsymbol{k}}^{\boldsymbol{M}}(s) + \frac{c_0^2}{\gamma_0}i\boldsymbol{k}\left[\widetilde{\delta\rho}_k(s) + \alpha_{T0}\tilde{g}_k(s)\right] = \boldsymbol{j}_{\boldsymbol{k}}^{\boldsymbol{M}}(0) \tag{5.14b}$$

$$\left[s + \gamma_0\chi_0 k^2 + (b+4)\frac{\kappa_{P0}}{C_{V0}}\sigma T_0^3\right]\tilde{g}_k(s) + \frac{\gamma_0 - 1}{\alpha_{T0}}i\boldsymbol{k}\cdot\boldsymbol{j}_{\boldsymbol{k}}^{\boldsymbol{M}}(s) + \frac{\kappa_{P0}}{C_{V0}}(a+1)\sigma T_0^4\delta\tilde{\rho}_k(s) = g_k(0), \tag{5.14c}$$

As for the optically thick case, we can solve these equations to get $\widetilde{\delta\rho}_k(s)$ (for more detail on the procedure see Appendix B) and then construct the correlation function $\langle\delta\rho_k^*(0)\widetilde{\delta\rho}_k(s)\rangle$, as in equation (5.15).

The dynamic structure factor is then obtained by taking the limit as defined above in equation (5.10). Unlike in the optically thick and hydrodynamic cases, this form of the DSF cannot be separated into partial fractions.

$$\frac{\langle \delta\rho_k^*(0)\widetilde{\delta\rho}_k(s)\rangle}{\langle \delta\rho_k^*(0)\delta\rho_k(0)\rangle}$$

$$= \frac{(s+\nu_{l_0}k^2)\left[s+\gamma_0\chi_0k^2+(b+4)\frac{\kappa_P}{C_{V0}}\sigma T_0^3\right]+\frac{\gamma_0-1}{\gamma_0}c_0^2k^2}{s\left[(s+\nu_{l_0}k^2)\left(s+\gamma_0\chi_0k^2+(b+4)\frac{\kappa_P}{C_{V0}}\sigma T_0^3\right)+\frac{\gamma_0-1}{\gamma_0}c_0^2k^2\right]+\frac{c_0^2k^2}{\gamma_0}\left[s+\gamma_0\chi_0k^2+(b+4)\frac{\kappa_P}{C_{V0}}\sigma T_0^3-\alpha_{T0}\frac{\kappa_P}{C_{V0}}(a+1)\sigma T_0^4\right]}. \quad (5.15)$$

5.6 Discussion

It is helpful to compare these results to the pure hydrodynamic case. Equations (5.16) show the raw result of the correlation function, and the further form of the dynamic structure factor when split into partial fractions respectively, for the hydrodynamic case. The form in equation (5.16b) is useful to understand the importance of each term in the form of the structure factor – where $\chi_0 k^2$ sets the width of the central, Rayleigh, peak; Γk^2 the width of the side, ion acoustic, peaks; and the position of these peaks is given by the dispersion relation, $\pm c_0 k$ – however the derivation depends on ignoring terms in k greater than order 2 in equation (5.16a), i.e. in the hydrodynamic limit of $k \to 0$. As has been discussed, this need not be the case for the validity to hold, and so beyond small k it is correct to instead use the form in equation (5.16a), using equation (5.10) to determine the structure factor. The form of this expression is not so concise, but there is significant deviation between the two forms when leaving the pure hydrodynamic limit.

$$\frac{\langle \delta\rho_k^*(0)\widetilde{\delta\rho_k}(s)\rangle}{\langle \delta\rho_k^*(0)\delta\rho_k(0)\rangle} = \frac{\left(s+\nu_{l_0}k^2\right)\left(s+\gamma_0\chi_0 k^2\right)+\frac{\gamma_0-1}{\gamma_0}c_0^2k^2}{s\left[\left(s+\nu_{l_0}k^2\right)\left(s+\gamma_0\chi_0 k^2\right)+\frac{\gamma_0-1}{\gamma_0}c_0^2k^2\right]+\frac{c_0^2k^2}{\gamma_0}\left(s+\gamma_0\chi_0k^2\right)}, \tag{5.16a}$$

$$\frac{S(k,\omega)}{S(k)} = \frac{\gamma_0-1}{\gamma_0}\frac{2\chi_0k^2}{\omega^2+\left(\chi_0k^2\right)^2}+\frac{1}{\gamma_0}\left[\frac{\Gamma k^2}{\left(\Gamma k^2\right)^2+\left(\omega+c_0k\right)^2}+\frac{\Gamma k^2}{\left(\Gamma k^2\right)^2+\left(\omega-c_0k\right)^2}\right]. \tag{5.16b}$$

Comparing the form of equation (5.11), optically thick, and equation (5.16b), hydrodynamic, we can see similarities, and where the radiation terms have modified the expression. If the radiative effects are large enough, we would expect the structure factor to change in the width of its central and side peaks, as well as the side peak positions, when compared to the purely hydrodynamic case. We might also expect a difference in the peak widths for the optically thin case, 5.15, though this is harder to see as the expression cannot be separated into fractions, even in the hydrodynamic limit, as the modifications to the denominator no longer allow for it to be factorised.

In figure 5.1 we can see the result of modifying the structure factor with radiation terms, plasma parameters are given in table 5.1. The graph shows the dynamic structure factor for a dense, aluminium plasma. Many properties are calculated from

Parameter		**Value**
Atomic Number	A	13
Mass Density	ρ	7.0 g/cc
Temperature	T	5–75 eV
Plasma Frequency	ω_p	0.15 fs^{-1}
Wavenumber	$\boldsymbol{k}$	2.1×10^{10} m^{-1}
Adiabatic Index	γ	1.79
Coloumb Logarithm	Λ	10
Thermal Diffusivity [m^2/s]	χ_{th}	$3.3 \times 10^{-7} \frac{AT^{5/2}}{Z(Z+1)\rho\Lambda}$
Kinematic Viscosity [m^2/s]	ν_ℓ	$3.3 \times 10^{-9} \frac{A^{1/2}T^{5/2}}{Z^4\rho\Lambda}$
Planck Mean Opacity [m^2/kg]	κ_P	$6.01 \times 10^7 \rho^{0.48} T^{-2.42}$
Rosseland Mean Opacity [m^2/kg]	κ_R	$1.04 \times 10^7 \rho^{0.48} T^{-2.48}$

Table 5.1: List of plasma parameters used in generating figure 5.1. The thermal diffusivity, kinematic viscosity and opacity expressions are taken from (76), (52) and (35) respectively.

relevant expressions within (1), such as the thermal diffusivity, viscosity and opacities. Ionisation state was taken from the PrOpacEos tables (105). The lines have all been scaled to the hydrodynamic case such that the peak of the hydrodynamic line has a value of 1.0. As expected, at low temperatures there is no effect on the shape of the structure factor. As we increase the temperature, the DSF including radiation increases in intensity, but the width thins compared to the hydrodynamic case. This is more pronounced as we go to higher temperatures. This effect can be related to the T^4 dependence of the radiative terms: being too small at low temperature to have a significant effect. The radiation here is acting as a heat bath, reducing the thermal fluctuations of the plasma, and thus sharpening the peaks. The opacity acts as a coupling parameter, and so explains why this effect is more pronounced in the optically thick case. There is also a slight modification of the side peak position (on the order of 0.01 fs^{-1} at 25 eV), as we increase in temperature. Assuming the same conditions, but for an optically thin plasma, produces a DSF that is essentially the same as the one we have calculated for ideal hydrodynamics.

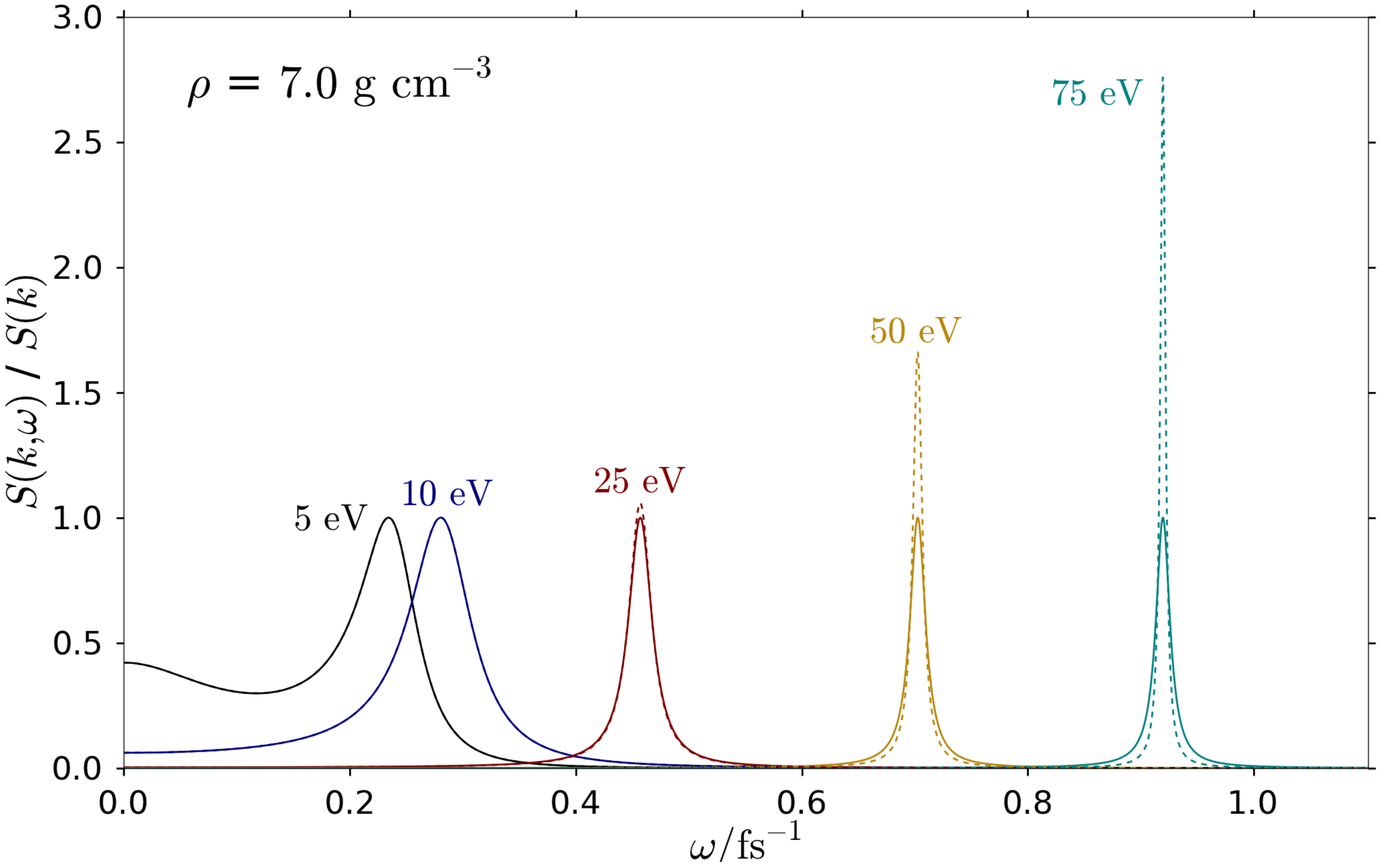

Figure 5.1: Showing the Dynamic Structure factor against frequency for a variety of temperatures. The hydrodynamic case is shown with a complete line, with the radiative case shown with a dashed line. Each line is scaled to the hydrodynamic case. We can see the increasing intensity, and narrowing, of the side peaks with increasing temperature.

The modification of the expression for the dynamic structure factor by radiation terms seems to have a modest, but present, effect. A measure of the relative importance of radiative energy flux to material energy flux is given by the Thick Radiation number derived in chapter 3, (1) (a similar number for the thin system is also applicable). When this shows that radiation is an important fraction of the energy, then there is likely to be a change in the shape of the structure factor (At temperatures greater than 10 eV, an estimate of this number is below 1 indicating that radiative effects, at least in terms of flux, become important).

5.7 Conclusion

Inclusion of radiative terms within the fluid dynamic equations leads to addition terms in the DSF following derivation from generalised hydrodynamics. As expected, at low temperature, the DSF agrees in the hydrodynamic and radiative forms, with differences occurring as the temperature increases. Further work on this could look into the feasibility of performing an experiment to check for the appearance of such modifications to the DSF.

5.8 Summary

In this chapter we have derived, from the relevant radiation hydrodynamic equations, the form of the dynamic structure factor in the presence of an optically thin or thick fluid. Inclusion of radiation terms was shown to have a modest, but noticeable, effect on the form of the dynamic structure factor in the optically thick case at higher temperatures, and a small effect at high temperatures and low densities in the optically thin case. In cases when radiation is expected to play a significant part in the fluid dynamics, which can be estimated by relevant ratios, calculation of the dynamic structure factor will have to take into account radiative terms.

Chapter 6

Conclusions and Further Work

> *"Don't cry because it's over. Smile because it happened."*
>
> – Dr Seuss

The work detailed in this thesis has primarily been interested in the modification of hydrodynamic equations beyond ideal conditions, and the application of this in laboratory experiments with the ultimate aim of furthering our understanding of astrophysics. As we probe further into plasma physics, into more extreme cases of high-energy-density matter, simple hydrodynamics, or even ideal MHD, equations are not sufficient to be able to describe the dynamics. The case of the inertial fusion campaign at NIF, and elsewhere, has shown many results that cannot be explained without introduction of further physics into the problem (33). Many cosmic events occur in regimes where radiation or magnetic field dominate over hydrodynamic effects. For example in ideal MHD there is no source term for magnetic field, so it is important to consider this when trying to answer some of the big questions of the field, such as from where the magnetic field in the ISM comes (21).

As well as correctly writing out terms of importance within our equations of motion, it is necessary to show that they can be written in a form that does not depend on the scale. This is a requirement for showing that lab based experiments are of relevance to astrophysics. As many cosmic events occur over long time scales, happen infrequently, or occur in environments that are not visible to telescopes, laboratory experiments are a valuable addition to observation and simulation.

Chapter 3 therefore defined a series of fluid equations that take into account many non-ideal effects. Magnetic effects were included beyond the ideal case, taking into account the effects of finite resistivity, baroclinic generation and advection of the field. Radiative effects in the form of radiation pressure, radiative flux, and volume forces of radiation on matter are included in the appropriate forms for an optically thin, or thick, fluid. Heat conduction, viscosity and, for the first time, quantum effects were also included.

These more complete forms of the fluid equations were then modified by dimensional analysis in order to make them scale invariant. This process created modifications to the non-ideal terms in the form of characteristic ratios which are of use in defining the flow and showing the effects that dominate the dynamics. They are also of importance when determining similarity between laboratory experiments and astrophysical phenomena, requiring either matching of the values or being sufficiently large such that the equations determining the motion have the same form.

Our derivation shows a simple conceptual form from which well known ratios, such as the Reynolds number, are derived, but it also introduced ratios relating to the effect of radiation in optically thin and thick environments, and quantum effects. The radiation numbers differ from others derived by taking into account the mean free path in relation to the characteristic spacial extent of the system. Quantum effects are included in the form of a potential and an example is given to show that their effect can be seen in a wider range of cases than may otherwise be thought.

Chapter 3 concludes with the practical application of the derived ratios applied to recent experiments. The ability to quickly determine the similarity is shown, as well as the current difficulty in matching phenomena with strong radiative components.

Chapter 4 describes the motivation, preparation, analysis and discussion of a laboratory astrophysics experiment performed at the Orion laser facility. The experiment concerned a laboratory analogue of a magnetic cataclysmic variable system, where material from a late, main sequence star is pulled onto a highly magnetised white dwarf. The strong magnetic field of the white dwarf diverts the incoming plasma away from a normal accretion disc, and instead directs the material onto the poles of the star, in an accretion column. Different accretion modes have been put forward, in order to explain ratios of hard and soft X-ray emission from the systems, but telescopes are not able to resolve such small features to discriminate the source of emission.

Using the results of the previous chapter, it was possible to design an experiment to test aspects of these theories. Thus preparation for the experiment was discussed in the form of simulation and target design, of which the salient features were the incoming plasma flow, confinement by magnetic field, and impact onto the white dwarf surface. A laboratory analogue was created using a laser-produced plasma, collimated by a plastic tube, which impacted onto an obstacle.

Optical and X-ray diagnostics were used in order to extract velocity and density measurements respectively. Well resolved, and reproducible, results are shown, which were consistent with simulation. Theoretical analysis also showed the importance of ionisation in increasing compression of the shocked material beyond the ideal case. Threshold analysis also places the experiment in the regime where radiative effects are beginning to become important, confirmed by the value of the thin radiation number.

A comparison to astrophysics was made, with agreement to predicted shock height above the impact region being seen. While the material and radiative energy fluxes are approaching the same magnitude in the laboratory, in the astrophysical case radiation effects dominated. Further work is thus needed to confirm that the shock height is caused by radiative loss. Nevertheless this chapter details the advancement of a platform to study the accretion column regime in MCVs.

Finally, in chapter 5, the effect of radiation on a plasma in thermal equilibrium was investigated theoretically. By addition of radiation terms to the fluid equations, following the formalism introduced in chapter 3, the dynamic structure factor was derived, and modification away from the pure hydrodynamic case was seen. The effect of radiation appeared to act as a cooling function, reducing thermal fluctuations and narrowing the width of ion acoustic peaks.

6.1 Further Work

Purely from an experimental viewpoint, there is much that can be further investigated in relation to laboratory analogues of accretion columns. In one recent experiment at LULI, the role of collimation was performed by a magnetic field from a pulsed power coil, instead of a tube, otherwise the experiment followed the same general set up as the Orion experiment, detailed in Chapter 4. The magnetic field is created by passing a very high current through a wire coil in a short space of time. The field establishes itself and is quasi-static over a timescale of microseconds, far longer than the timescale of the experiment. To get to sufficiently high fields to show collimation, however, requires that the dimensions of the coil are small, and that the target is placed in the centre to avoid field edge effects. The magnetic field is parallel to the plasma flow, as in the astrophysical case, and so acts only to collimate the flow, rather than changing the dynamics within it. This has practical benefits for radiography, as only the experimental plasma is present, but also more closely simulates the astrophysical environment.

As figure 6.1 shows, we see a definite collimation of the incoming plasma when the field is present. Due to experimental complications, we were unable to see the reverse shock feature in this experimental run. Further work can thus expand upon use of the magnetic field as collimation, and try to recreate the images seen in the Orion experiment. The MIFED coils at the Omega Laser facility would also enable an experiment like this to occur, but with the advantage of a much larger laser system, thus allowing faster flow velocities, which would lead to better similarity between the laboratory experiment and astrophysics.

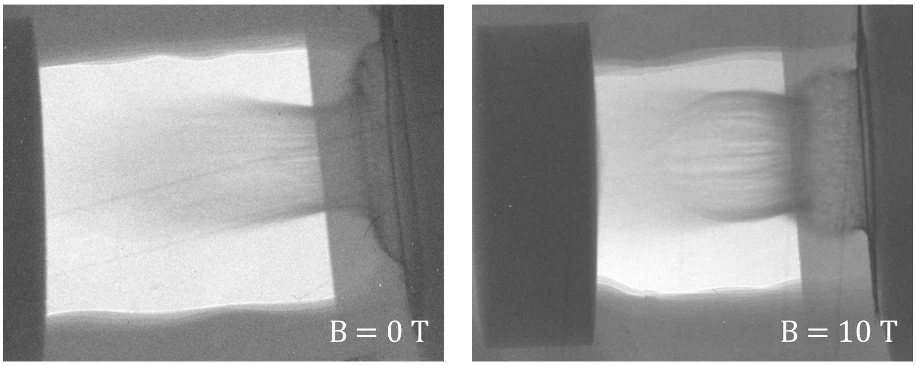

Figure 6.1: Figure showing radiographs at 60 ns delay of plasma flow with, right, and without, left, a 10 T magnetic field. The laser is fired on the right of the images, and the plasma flows from right to left, with the very dark region on the left hand side being the obstacle. We can see a marked difference in the shape of the plasma jet, with more collimation with a magnetic field present.

The fact that the radiative energy flux dominates over the mass flux is of great importance in MCV star systems. Energy lost through radiation flux counters the incoming material energy flux and is thought to cause a stationary shock to form in the accretion column. In the Orion experiment we showed a stationary shock, and showed radiation was beginning to have an effect, but further work can be performed to increase the radiative nature of the shock. Using a laser system such as NIF or LMJ would allow us to drive the target harder, leading to a greater incoming flow velocity and higher post-shock temperature. This should cause radiative energy flux to dominate over material energy flux, and thus cause a stationary shock. If this agrees with predicted shock heights then it would further validate this theory, and thus be of use in understanding the astrophysical case.

From a theoretical point of view, there are many more terms that could be included when considering the full equations, for example, we only include two extra from the modified Ohm's Law defined by Haines (70), though there are many more. Using the formalism in chapter 3 it would be simple to add these and derive ratios, if further work entered a regime where they became important. When considering the DSF we have assumed a stationary plasma, instead we could consider cases where we have a dense radiating plasma flow, more similar to the experimental case of chapter 4. The theory also has the opportunity to be expanded in the case were fluctuations in the properties are not small or not in equilibrium. Experimental validation of the difference in XRTS signal when in a regime where radiation is important compared to the hydrodynamic case would also be of use.

6.2 Final Remarks

The aim throughout this thesis has been to understand astrophysics through the design of laboratory experiments. Particularly we have focussed on cases where radiation plays a large part in the overall dynamics. This was introduced theoretically by showing how this modifies the hydrodynamic equations, along with other non-ideal terms, and also the by its effect on the dynamic structure factor. Experimentally we showed an attempt to simulate, in the laboratory, an astrophysical system where radiation is expected to play a key role in the system's evolution.

As touched upon at the end of chapter 3, and in the result of chapter 4, performing experiments beyond the ideal case, especially with radiation, is challenging. However, we should take heart from the progress that has been made in the field since its conception, which in itself is young. Even for the case of our experiment we show significant improvement over the previous experimental attempt, and we begin to see the effect of radiation, and draw closer to similarity with the astrophysical case. Work is already ongoing to build and improve upon this. As experimental facilities improve, and more theoretical work is undertaken, we continue to open up new possibilities for lab-based experiments with greater similarity to the astrophysical case.

All of this work helps further our understanding but also makes clear one point: that there is still much research to be done in the realm of laboratory astrophysics to understand plasma physics and the universe!

Appendix A

Derivation of Dimensionless Full Magneto-Quantum-Radiative Hydrodynamic Equations

The derivation of the dimensionless form of the momentum and energy equations (in the radiative thick regime) is outlined here in detail.

A.1 Momentum Equation

Considering each term separately, we have:

$$\rho\left(\frac{\partial \boldsymbol{u}}{\partial t}+\boldsymbol{u}\cdot\nabla\boldsymbol{u}\right)\rightarrow\frac{\rho_0 u_0^2}{\ell_0}\rho^*\left(\frac{\partial\boldsymbol{u}^*}{\partial t^*}+\boldsymbol{u}^*\cdot\nabla^*\boldsymbol{u}^*\right), \tag{A.1a}$$

$$-\nabla\left(p+\frac{4\sigma T^4}{3c}\right)\rightarrow-\frac{\rho_0 u_0^2}{\ell_0}\nabla^*\left(p^*+\frac{4\sigma T_0^4}{3\rho_0 u_0^2 c}T^{*4}\right), \tag{A.1b}$$

$$\frac{\hbar^2\rho}{2m^2}\nabla\left(\frac{\nabla^2\sqrt{\rho}}{\sqrt{\rho}}\right)\rightarrow\frac{\rho_0 u_0^2}{\ell_0}\left(\frac{\hbar}{\ell_0 u_0\sqrt{2}m}\right)^2\rho^*\nabla^*\left(\frac{\nabla^{*2}\sqrt{\rho^*}}{\sqrt{\rho^*}}\right), \tag{A.1c}$$

$$\begin{aligned}&\nabla\cdot\left\{\rho\nu\left[\nabla\boldsymbol{u}+(\nabla\boldsymbol{u})^T-\frac{2}{3}(\nabla\cdot\boldsymbol{u})\underline{\boldsymbol{I}}\right]+\zeta(\nabla\cdot\boldsymbol{u})\underline{\boldsymbol{I}}\right\}\\&\quad\rightarrow\frac{\rho_0 u_0^2}{\ell_0}\nabla^*\cdot\left\{\frac{\mu}{\rho_0 u_0\ell_0}\left[\nabla^*\boldsymbol{u}^*+(\nabla^*\boldsymbol{u}^*)^T-\frac{2}{3}(\nabla^*\cdot\boldsymbol{u}^*)\underline{\boldsymbol{I}}\right]+\frac{\zeta}{\rho_0 u_0\ell_0}(\nabla^*\cdot\boldsymbol{u}^*)\underline{\boldsymbol{I}}\right\},\end{aligned} \tag{A.1d}$$

$$\rho_C\boldsymbol{E}+\boldsymbol{J}\times\boldsymbol{B}\rightarrow\frac{\rho_0 u_0^2}{\ell_0}\left(\frac{\rho_{C_0}\ell_0 E_0}{\rho_0 u_0^2}\rho_C^*\boldsymbol{E}^*+\frac{J_0\ell_0}{u_0\sqrt{\mu_0\rho_0}}\boldsymbol{J}^*\times\boldsymbol{B}^*\right). \tag{A.1e}$$

If we divide through by the common term $\rho_0 u_0^2/\ell_0$, we obtain equation (3.15).

A.2 Energy Equation

Considering again each term separately as we have done for the momentum equation:

$$\frac{\partial}{\partial t}\left(\rho\epsilon+\frac{\rho u^2}{2}+\frac{4\sigma T^4}{c}\right)\rightarrow\frac{\rho_0 u_0^3}{\ell_0}\frac{\partial}{\partial t^*}\left(\rho^*\epsilon^*+\frac{\rho^* u^{*2}}{2}+\frac{4\sigma T_0^4}{\rho_0 u_0^2 c}T^{*4}\right), \tag{A.2a}$$

$$\nabla\cdot\left[\rho\boldsymbol{u}\left(\epsilon+\frac{u^2}{2}\right)+p\boldsymbol{u}\right]\rightarrow\frac{\rho_0 u_0^3}{\ell_0}\nabla^*\cdot\left[\rho^*\boldsymbol{u}^*\left(\epsilon^*+\frac{u^2}{2}\right)+p^*\boldsymbol{u}^*\right], \tag{A.2b}$$

$$\nabla\cdot\left(\frac{16\sigma T^3}{3\kappa_R\rho}\nabla T\right)\rightarrow\frac{\rho_0 u_0^3}{\ell_0}\nabla^*\cdot\left(\frac{16\sigma T_0^4}{3\kappa_R\rho_0^2\ell_0 u_0^3}\frac{T^{*3}}{\rho^*}\nabla^* T^*\right), \tag{A.2c}$$

$$-\nabla\cdot\left(\frac{3\sigma T^4}{c}\right)\cdot\boldsymbol{u}\rightarrow-\frac{\rho_0 u_0^3}{\ell_0}\nabla^*\cdot\left(\frac{4\sigma T_0^4}{\rho_0 u_0^2 c}T^{*4}\right)\cdot\boldsymbol{u}^*, \tag{A.2d}$$

$$\nabla\cdot\left[\frac{\chi_{th}\rho k_B\gamma}{m(\gamma-1)}\nabla T\right]\rightarrow\frac{\rho_0 u_0^3}{\ell_0}\nabla^*\cdot\left[\frac{\chi_{th}k_B T_0\gamma}{\ell_0 m u_0^3(\gamma-1)}\rho^*\nabla^* T^*\right], \tag{A.2e}$$

$$\begin{aligned}&\nabla\cdot\left\{\rho\nu\left[\nabla\boldsymbol{u}+(\nabla\boldsymbol{u})^T-\frac{2}{3}(\nabla\cdot\boldsymbol{u})\underline{\boldsymbol{I}}\right]+\zeta(\nabla\cdot\boldsymbol{u})\underline{\boldsymbol{I}}\right\}\cdot\boldsymbol{u}\\&\qquad\rightarrow\frac{\rho_0 u_0^3}{\ell_0}\nabla^*\cdot\left\{\frac{\mu}{\rho_0 u_0\ell_0}\left[\nabla^*\boldsymbol{u}^*+(\nabla^*\boldsymbol{u}^*)^T-\frac{2}{3}(\nabla^*\cdot\boldsymbol{u}^*)\underline{\boldsymbol{I}}\right]\right.\\&\qquad\qquad\left.+\frac{\zeta}{\rho_0 u_0\ell_0}(\nabla^*\cdot\boldsymbol{u}^*)\underline{\boldsymbol{I}}\right\}\cdot\boldsymbol{u}^*,\end{aligned} \tag{A.2f}$$

$$\boldsymbol{J}\cdot\boldsymbol{E}\rightarrow\frac{\rho_0 u_0^3}{\ell_0}\frac{J_0 E_0\ell_0}{\rho_0 u_0^3}\boldsymbol{J}^*\cdot\boldsymbol{E}^*, \tag{A.2g}$$

$$\frac{\hbar^2\rho}{2m^2}\nabla\left(\frac{\nabla^2\sqrt{\rho}}{\sqrt{\rho}}\right)\cdot\boldsymbol{u}\rightarrow\frac{\rho_0 u_0^3}{\ell_0}\left(\frac{\hbar}{u_0\ell_0\sqrt{2}m}\right)^2\rho^*\nabla^*\left(\frac{\nabla^{*2}\sqrt{\rho^*}}{\sqrt{\rho^*}}\right)\cdot\boldsymbol{u}^*, \tag{A.2h}$$

$$-\frac{4\sigma T^4}{3c}\nabla\cdot\boldsymbol{u}\rightarrow-\frac{\rho_0 u_0^3}{\ell_0}\left(\frac{4\sigma T_0^4}{3cu_0^2\rho_0}\right)T^{*4}\nabla^*\cdot\boldsymbol{u}^*. \tag{A.2i}$$

The factor $\rho_0 u_0^3/\ell_0$ has been isolated from each term. If we divide through by this, we then obtain equation (3.21).

A.3 Full Equations

Here we give a full summary of all the dimensionless equation of magneto-quantum-resistive hydrodynamics:

A.3.1 Continuity Equation

$$\frac{\partial \rho^*}{\partial t^*} + \nabla^* \cdot \rho^* \boldsymbol{u}^* = 0,$$

A.3.2 Induction Equation

$$\frac{\partial \boldsymbol{B}^*}{\partial t^*} = \nabla^* \times (\boldsymbol{u}^* \times \boldsymbol{B}^*) - \frac{1}{Re_M} \nabla^* \times (\eta^* \nabla^* \times \boldsymbol{B}^*) + \frac{1}{\mathcal{B}i} \frac{\nabla^* p^* \times \nabla^* \rho^*}{\rho^{*2}} + \frac{1}{\mathcal{N}e} \nabla^* \times (\boldsymbol{B}^* \times \nabla^* T^*)$$

A.3.3 Momentum Equation

A.3.3.1 Optically Thick

$$\rho^* \left(\frac{\partial \boldsymbol{u}^*}{\partial t^*} + \boldsymbol{u}^* \cdot \nabla^* \boldsymbol{u}^* \right) = -\nabla^* \left[p^* + \frac{1}{R} T^{*4} \right] + \frac{1}{\mathcal{H}_Q} \rho^* \nabla^* \left(\frac{\nabla^{*2} \sqrt{\rho^*}}{\sqrt{\rho^*}} \right)$$
$$+ \nabla^* \cdot \left\{ \frac{1}{Re} \left[\nabla^* \boldsymbol{u}^* + (\nabla^* \boldsymbol{u}^*)^T - \frac{2}{3} (\nabla^* \cdot \boldsymbol{u}^*) \underline{\boldsymbol{I}} \right] + \frac{1}{Re_\zeta} (\nabla^* \cdot \boldsymbol{u}^*) \underline{\boldsymbol{I}} \right\} + \frac{1}{\Omega_R} \rho_C^* \boldsymbol{E}^* + \frac{1}{\Omega_H} \boldsymbol{J}^* \times \boldsymbol{B}^*$$

A.3.3.2 Optically Thin

$$\rho^* \left(\frac{\partial \boldsymbol{u}^*}{\partial t^*} + \boldsymbol{u}^* \cdot \nabla^* \boldsymbol{u}^* \right) = -\nabla^* p^* + \frac{1}{\mathcal{H}_Q} \rho^* \nabla^* \left(\frac{\nabla^{*2} \sqrt{\rho^*}}{\sqrt{\rho^*}} \right)$$
$$+ \nabla^* \cdot \left\{ \frac{1}{Re} \left[\nabla^* \boldsymbol{u}^* + (\nabla^* \boldsymbol{u}^*)^T - \frac{2}{3} (\nabla^* \cdot \boldsymbol{u}^*) \underline{\boldsymbol{I}} \right] + \frac{1}{Re_\zeta} (\nabla^* \cdot \boldsymbol{u}^*) \underline{\boldsymbol{I}} \right\} + \frac{1}{\Omega_R} \rho_C^* \boldsymbol{E}^* + \frac{1}{\Omega_H} \boldsymbol{J}^* \times \boldsymbol{B}^*$$

A.3.4 Energy Equation

A.3.4.1 Optically Thick

$$\begin{aligned}
&\frac{\partial}{\partial t^*}\left(\rho^*\epsilon^* + \frac{\rho^* u^{*2}}{2} + \frac{3}{R}T^{*4}\right) + \nabla^*\cdot\left[\rho^*\boldsymbol{u}^*\left(\epsilon^* + \frac{u^2}{2}\right) + p^*\boldsymbol{u}^*\right] \\
&\qquad = \nabla^*\cdot\left\{\frac{1}{\Pi_{thick}}\frac{T^{*3}}{\rho^*}\nabla^* T^* - \frac{3}{R}T^{*4}\cdot\boldsymbol{u}^* + \frac{1}{Pe}\frac{\gamma}{\gamma-1}\rho^*\nabla^* T^*\right. \\
&\qquad\left. + \frac{1}{Re}\left[\nabla^*\boldsymbol{u}^* + (\nabla^*\boldsymbol{u}^*)^T - \frac{2}{3}(\nabla^*\cdot\boldsymbol{u}^*)\underline{\boldsymbol{I}}\right]\cdot\boldsymbol{u}^* + \frac{1}{Re_\zeta}(\nabla^*\cdot\boldsymbol{u}^*)\underline{\boldsymbol{I}}\cdot\boldsymbol{u}^*\right\} \\
&\qquad\qquad - \frac{1}{\Omega_R}\boldsymbol{J}^*\cdot\boldsymbol{E}^* + \frac{1}{\mathcal{H}_Q}\rho^*\nabla^*\left(\frac{\nabla^{*2}\sqrt{\rho^*}}{\sqrt{\rho^*}}\right)\cdot\boldsymbol{u}^* - \frac{1}{R}T^{*4}\nabla^*\cdot\boldsymbol{u}^*
\end{aligned}$$

A.3.4.2 Optically Thin

$$\begin{aligned}
&\frac{\partial}{\partial t^*}\left(\rho^*\epsilon^* + \frac{\rho^* u^{*2}}{2}\right) + \nabla^*\cdot\left[\rho^*\boldsymbol{u}^*\left(\epsilon^* + \frac{u^2}{2}\right) + p^*\boldsymbol{u}^*\right] \\
&= \nabla^*\cdot\left\{\frac{1}{Pe}\frac{\gamma}{\gamma-1}\rho^*\nabla^* T^* + \frac{1}{Re}\left[\nabla^*\boldsymbol{u}^* + (\nabla^*\boldsymbol{u}^*)^T - \frac{2}{3}(\nabla^*\cdot\boldsymbol{u}^*)\underline{\boldsymbol{I}}\right]\cdot\boldsymbol{u}^* + \frac{1}{Re_\zeta}(\nabla^*\cdot\boldsymbol{u}^*)\underline{\boldsymbol{I}}\cdot\boldsymbol{u}^*\right\} \\
&\qquad\qquad - \frac{1}{\Omega_R}\boldsymbol{J}^*\cdot\boldsymbol{E}^* + \frac{1}{\mathcal{H}_Q}\rho^*\nabla^*\left(\frac{\nabla^{*2}\sqrt{\rho^*}}{\sqrt{\rho^*}}\right)\cdot\boldsymbol{u}^* - \frac{1}{\Pi_{thin}}\rho^* T^{*4}
\end{aligned}$$

APPENDIX B

Derivation of Structure Factor

The Appendix outlines the procedure for calculating the dynamic structure factor starting from the hydrodynamic equations using the example of the radiation hydrodynamic equations suitable for an optically thin fluid. The procedure itself is general: by substituting in the correct form of the momentum and energy equations for an optically thick fluid the dynamic structure factor can be calculated.

B.1 Momentum Equation

Starting from equation 5.12b we write the equation with the explicit form of the stress tensor:

$$\rho\left(\frac{\partial \boldsymbol{u}}{\partial t}+\boldsymbol{u}\cdot\nabla\boldsymbol{u}\right)=-\nabla p+\eta_1\left[\nabla^2\boldsymbol{u}+\nabla\left(\nabla\cdot\boldsymbol{u}\right)\right]+\eta_2\nabla\left(\nabla\cdot\boldsymbol{u}\right), \tag{B.1}$$

where ρ is the mass density, t the time, $\boldsymbol{u}$ the velocity, p the pressure and η_i are the first and second coefficients of viscosity. We now use the thermodynamic relations:

$$\frac{\partial}{\partial r_i}p=\left(\frac{\partial p}{\partial \rho}\right)_T\frac{\partial}{\partial r_i}\rho+\left(\frac{\partial p}{\partial T}\right)_\rho\frac{\partial}{\partial r_i}T,$$

$$\left(\frac{\partial p}{\partial \rho}\right)_T=\frac{C_V}{C_P}\left(\frac{\partial p}{\partial \rho}\right)_{\mathcal{S}}=\frac{c^2}{\gamma},\quad \left(\frac{\partial p}{\partial T}\right)_\rho=\left(\frac{\partial p}{\partial \rho}\right)_T\left(\frac{\partial \rho}{\partial T}\right)_p=\frac{c^2}{\gamma}\alpha_T\rho,$$

where T is the temperature, C_V the heat capacity at constant volume, C_P is the heat capacity at constant pressure, $\mathcal{S}$ is the entropy, c is the adiabatic sound speed, γ is the adiabatic index, and α_T is the coefficient of thermal expansion.

We now replace these terms in equation B.1 to give:

$$\rho\left(\frac{\partial \boldsymbol{u}}{\partial t}+\boldsymbol{u}\cdot\nabla\boldsymbol{u}\right)=-\left(\frac{c^2}{\gamma}\nabla\cdot\rho+\frac{c^2}{\gamma}\alpha_T\rho\nabla T\right)+\eta_1\left[\nabla^2\boldsymbol{u}+\nabla\left(\nabla\cdot\boldsymbol{u}\right)\right]+\eta_2\nabla\left(\nabla\cdot\boldsymbol{u}\right),$$

Linearising with $\delta\rho = \rho - \rho_0$, $\delta T = T - T_0$, $\delta u = u$, and only keeping terms to first order in the fluctuations, gives equation 5.13b.

B.2 Energy Equation

Starting from equation 5.12c we use the thermodynamic relations:

$$d\epsilon = \left(\frac{\partial \epsilon}{\partial \rho}\right)_{\mathcal{S}} d\rho + \left(\frac{\partial \epsilon}{\partial \mathcal{S}}\right)_{\rho} d\mathcal{S}, \quad \left(\frac{\partial \epsilon}{\partial \rho}\right)_{\mathcal{S}} = \frac{p}{\rho^2}, \quad \left(\frac{\partial \epsilon}{\partial \mathcal{S}}\right)_{\rho} = T,$$

(where ϵ is the internal energy per unit mass, $\mathcal{S}$ the entropy) and the continuity equation (5.12a) to give:

$$\rho T \frac{d\mathcal{S}}{dt} = \nabla \cdot \boldsymbol{\sigma}_\nu \cdot \boldsymbol{u} - \nabla \cdot \boldsymbol{q} - \ell_\Lambda.$$

Next we explicitly write out the form of the heat flux, $\boldsymbol{q}$, and define the entropy in terms of ρ and T:

$$\nabla \cdot \boldsymbol{q} = -\kappa \nabla^2 T, \quad d\mathcal{S} = \left(\frac{\partial \mathcal{S}}{\partial \rho}\right)_T d\rho + \left(\frac{\partial \mathcal{S}}{\partial T}\right)_\rho dT,$$

$$\left(\frac{\partial \mathcal{S}}{\partial \rho}\right)_T = \frac{-1}{\rho^2}\left(\frac{\partial p}{\partial T}\right)_\rho, \quad \left(\frac{\partial \mathcal{S}}{\partial T}\right)_\rho = \frac{C_V}{T}, \quad \left(\frac{\partial p}{\partial T}\right)_\rho = \frac{C_P - C_V}{\alpha_T T}\rho$$

where κ is the thermal conductivity coefficient.

Substituting these into the above equation, and making use of the continuity equation again, gives:

$$\frac{\partial T}{\partial t} + \boldsymbol{u} \cdot \nabla T = \frac{1}{C_V \rho}\left(\nabla \cdot \boldsymbol{\sigma}_\nu \cdot \boldsymbol{u} + \kappa \nabla^2 T - \rho \kappa_P \sigma T^4\right) - \frac{\gamma - 1}{\alpha_T} \nabla \cdot \boldsymbol{u}$$

Linearising with $\delta\rho = \rho - \rho_0$, $\delta T = T - T_0$, $\delta u = u$, and only keeping terms to first order in the fluctuations gives equation 5.13c.

B.3 Solving for Transformed Fluctuation in Density ($\widetilde{\delta\rho}_k(s)$)

We can solve 5.14 for $\widetilde{\delta\rho}_k(s)$. Following Cramer's Rule we write:

$$\widetilde{\delta\rho}_k(s) = \frac{|N(k,s)|}{|M(k,s)|}$$

where we define the matrices $N(k,s)$ and $M(k,s)$ from 5.14 as (with independent variables ρ, $\boldsymbol{j^M} = \rho_0 \boldsymbol{u}$ and $g = \rho_0 \delta T$):

$$M(k,s) = \begin{bmatrix} s & i\boldsymbol{k} & 0 \\ \frac{c_0^2}{\gamma_0} i\boldsymbol{k} & s + \nu_{l_0} k^2 & \frac{\alpha_{T0} c_0^2}{\gamma_0} i\boldsymbol{k} \\ \frac{\kappa_{P0}}{C_{V0}}(a+1)\sigma T_0^4 & \frac{\gamma_0 - 1}{\alpha_{T0}} i\boldsymbol{k} & s + \gamma_0 \chi_0 k^2 + (4+b)\frac{\kappa_{P0}}{C_{V0}} \rho T_0^3 \end{bmatrix} \tag{B.2a}$$

$$N(k,s) = \begin{bmatrix} \delta\rho_k(0) & i\boldsymbol{k} & 0 \\ \boldsymbol{j_k^M}(0) & s + \nu_{l_0} k^2 & \frac{\alpha_{T0} c_0^2}{\gamma_0} i\boldsymbol{k} \\ g_k(0) & \frac{\gamma_0 - 1}{\alpha_{T0}} i\boldsymbol{k} & s + \gamma_0 \chi_0 k^2 + (4+b)\frac{\kappa_{P0}}{C_{V0}} \rho_0 T_0^3 \end{bmatrix} \tag{B.2b}$$

which gives:

$$\widetilde{\delta\rho_k}(s) = \frac{\delta\rho_k(0)\left[\left(s + \nu_{l_0}k^2\right)\left(s + \gamma_0\chi_0 k^2 + (4+b)\frac{\kappa_{P0}}{C_{V0}}\sigma T_0^3\right) + \frac{\gamma_0 - 1}{\gamma_0} c_0^2 k^2\right] - i\boldsymbol{k}\left[\boldsymbol{j_k^M}(0)\left(s + \gamma_0\chi_0 k^2 + (4+b)\frac{\kappa_{P0}}{C_{V0}}\sigma T_0^3\right) - g_k(0)\frac{\alpha_{T0}c_0^2}{\gamma_0} i\boldsymbol{k}\right]}{s\left[(s + \nu_{l_0}k^2)\left(s + \gamma_0\chi_0 k^2 + (4+b)\frac{4\kappa_{P0}}{C_{V0}}\sigma T_0^3\right) + \frac{\gamma_0 - 1}{\gamma_0} c_0^2 k^2\right] - i\boldsymbol{k}\left[\frac{c_0^2}{\gamma_0} i\boldsymbol{k}\left(s + \gamma_0\chi_0 k^2 + (4+\beta)\frac{\kappa_{P0}}{C_{V0}}\sigma T_0^3 - \frac{\alpha_{T0}\kappa_{P0}}{C_{V0}}(a+1)\sigma T_0^4\right)\right]}$$

where ν_{ℓ_0} is the kinematic viscosity, $\chi_0 = \kappa_0/\rho_0 C_{P0}$ is the thermal diffusivity.

Bibliography

[1] J. E. Cross, B. Reville, and G Gregori. Scaling of Magneto-Quantum-Radiative Hydrodynamic equations: from laser-produced plasmas to astrophysics. *The Astrophysical Journal*, 795(1):59, 2014.

[2] E. R. Tubman, R. Crowston, R. Alraddadi, H. W. Doyle, J. Meinecke, J. E. Cross, R. Bolis, D. Lamb, P. Tzeferacos, D. Doria, B. Reville, H. Ahmed, M. Borghesi, G. Gregori, and N. C. Woolsey. Nanosecond Imaging of Shock- and Jet-Like Features. *IEEE Transactions on Plasma Science*, 42(10):2496–2497, Oct 2014.

[3] J. J. Santos, M. Bailly-Grandvaux, L. Giuffrida, P. Forestier-Colleoni, S. Fujioka, Z. Zhang, P. Korneev, R. Bouillaud, S. Dorard, D. Batani, M. Chevrot, J. E. Cross, R. Crowston, J-L Dubois, J. Gazave, G. Gregori, E. d'Humieres, S. Hulin, K. Ishihara, S. Kojima, E. Loyez, J-R Marques, A. Morace, P. Nicolai, O. Peyrusse, A. Poye, D. Raffestin, J. Ribolzi, M. Roth, G. Schaumann, F. Serres, V. T. Tikhonchuk, P. Vacar, and N. Woolsey. Laser-driven platform for generation and characterization of strong quasi-static magnetic fields. *New Journal of Physics*, 17(8):083051, 2015.

[4] P. Mabey, N. J. Hartley, H. W. Doyle, J. E. Cross, L. Ceurvorst, A. Savin, A. Rigby, M. Oliver, M. Calvert, I. J. Kim, D. Riley, P. A. Norreys, C. H. Nam, D. C. Carroll, C. Spindloe, and G. Gregori. Characterization of x-ray lens for use in probing high energy density states of matter. *Journal of Instrumentation*, 10(04):P04010, 2015.

[5] R. D. Speck, E. S. Bliss, J. A. Glaze, J. W. Herris, F. W. Holloway, J. T. Hunt, B. C. Johnson, D. J. Kuizenga, R. G. Ozarski, H. G. Patton, P. R. Rupert,

G. J. Suski, C. D. Swift, and C. E. Thompson. The Shiva Laser-Fusion Facility. *IEEE Journal of Quantum Electronics*, 17(9):1599, 1981.

[6] T. Ditmire. High-Power Lasers. *American Scientist*, 98:394, 2010.

[7] T. R. Boehly, R. L. McCrory, C. P. Verdon, W. Seka, S. J. Loucks, A. Babushkin, R. E. Bahr, R. Boni, D. K. Bradley, R. S. Craxton, J. A. Delettrez, W. R Donaldson, R. Epstein, D. Harding, P. A. Jaanimagi, S. D. Jacobs, K. Kearney, R. L. Keck, J. H. Kelly, T. J. Kessler, R. L. Kremens, J. P. Knauer, D. J. Lonobile, L. D. Lund, F. J. Marshall, P. W. McKenty, D. D. Meyerhofer, S. F. B. Morse, A. Okishev, S. Papernov, G. Pien, T. Safford, J. D. Schnittman, R. Short, M. J. Shoup, M. Skeldon, S. Skupsky, A. W. Schmid, V. A. Smalyuk, D. J. Smith, J. M. Soures, M. Wittman, and B. Yaakobi. Inertial confinement fusion experiments with OMEGA-A 30-kJ, 60-beam UV laser. *Fusion Engineering and Design*, 44(14):35 – 42, 1999.

[8] E. M. Campbell, J. T. Hunt, E. S. Bliss, D. R. Speck, and R. P. Drake. Nova experimental facility (invited). *Review of Scientific Instruments*, 57(8), 1986.

[9] C. Yamanaka, S. Nakai, T. Yamanaka, Y. Izawa, Y. Kato, K. Mima, K. Nishihara, T. Mochizuki, M. Yamanaka, M. Nakatsuka, T. Sasaki, T. Yabe, K. Yoshida, H. Azechi, H. Nishimura, T. Norimatsu, S. Ido, N. Miyanaga, S. Sakabe, H. Takabe, J. Jitsuno, and M. Takagi. High thermonuclear neutron yield by shock multiplexing implosion with GEKKO XII green laser. *Nuclear Fusion*, 27(1):19, 1987.

[10] A. Pak, L. Divol, G. Gregori, S. Weber, J. Atherton, R. Bennedetti, D. K. Bradley, D. Callahan, D. T. Casey, E. Dewald, T. Döppner, M. J. Edwards, J. A. Frenje, S. Glenn, G. P. Grim, D. Hicks, W. W. Hsing, N. Izumi, O. S. Jones, M. G. Johnson, S. F. Khan, J. D. Kilkenny, J. L. Kline, G. A. Kyrala, J. Lindl, O. L. Landen, S. Le Pape, T. Ma, A. MacPhee, B. J. MacGowan, A. J. MacKinnon, L. Masse, N. B. Meezan, J. D. Moody, R. E. Olson, J. E. Ralph, H. F. Robey, H.-S. Park, B. A. Remington, J. S. Ross, R. Tommasini, R. P. J. Town, V. Smalyuk, S. H. Glenzer, and E. I. Moses. Radiative shocks produced from spherical cryogenic implosions at the National Ignition Facility. *Physics of Plasmas*, 20:056315–056326, 2013.

[11] C. M. Krauland, R. P. Drake, C. C. Kuranz, R. Sweeney, M. Grosskopf, S. Klein, R. Gillespie, P. A. Keiter, B. Loupias, and É. Falize. Radiative reverse

shock laser experiments relevant to accretion processes in cataclysmic variables. *Physics of Plasmas*, 20:056502, 2013.

[12] S. V. Lebedev, A. Ciardi, D. J. Ampleford, S. N. Bland, S. C. Bott, J. P. Chittenden, G. N. Hall, J. Rapley, C. Jennings, M. Sherlock, A. Frank, and E. G. Blackman. Production of radiatively cooled hypersonic plasma jets and links to astrophysical jets. *Plasma Physics and Controlled Fusion*, 47:465–479, 2005.

[13] J. Kane, D. Arnett, B. A. Remington, S. G. Glendinning, J. Castor, R. Wallace, A. Rubenchik, and B. A. Fryxell. Supernova-relevant Hydrodynamic Instability Experiments on the Nova Laser. *The Astrophysical Journal*, 478(2):L75–L78, 1997.

[14] B. A. Remington, J. Kane, R. P. Drake, S. G. Glendinning, K. Estabrook, R. London, J. Castor, R. J. Wallace, D. Arnett, E. Liang, R. McCray, A. Rubenchik, and B. Fryxell. Supernova hydrodynamics experiments on the Nova laser. *Physics of Plasmas*, 4(5/2):1994–2003, 1997.

[15] B. A. Remington, R. P. Drake, and D. D. Ryutov. Experimental astrophysics with high power lasers and Z pinches. *Reviews of Modern Physics*, 78(3):755–807, 2006.

[16] B. A. Remington, D. Arnett, R. P. Drake, and H. Takabe. Modeling Astrophysical Phenomena with Intense Lasers in the laboratory. *Science*, 284(5419):1488–1493, 1999.

[17] R. P. Drake, J. J. Carroll III, K. Estabrook, S. G. Glendinning, B. A. Remington, R. Wallace, and R. McCray. Development of a laboratory environment to test models of supernova remnant formation. *The Astrophysical Journal*, 500:157–161, 1998.

[18] R. P. Drake, S. G. Glendinning, K. Estabrook, B. A. Remington, R. McCray, R. J. Wallace, L. J. Suter, T. B. Smith, J. J. Carroll III, R. A. London, and E. Liang. Observation of Forward Shocks and Stagnated Ejecta Driven by High-Energy-Density Plasma Flow. *Physical Review Letters*, 81(10):1–4, 1998.

[19] V. T. Tikhonchuk, Ph. Nicolaï, X. Ribeyre, C. Stenz, G. Schurtz, A. Kasperczuk, T. Pisarczyk, L. Juha, E. Krousky, M. Masek, K. Pfeifer, K. Rohlena,

J. Skala, J. Ullschmied, M. Kalal, D. Klir, J. Kravarik, P. Kubes, and P. Pisarczyk. Laboratory modeling of supersonic radiative jets propagation in plasmas and their scaling to astrophysical conditions. *Plasma Physics and Controlled Fusion*, 50:124056, 2008.

[20] R. Yurchak, A. Ravasio, A. Pelka, S. Pikuz, É. Falize, T. Vinci, M. Koenig, B. Loupias, M. Fatenejad, P. Tzeferacos, D. Q. Lamb, and E. G. Blackman. Experimental Demonstration of an Inertial Collimation Mechanism in Nested Outflows. *Physical Review Letters*, 155001(April):2–6, 2014.

[21] J. Meinecke, H. W. Doyle, F. Miniati, A. R. Bell, R. Bingham, R. Crowston, R. P. Drake, M. Fatenejad, M. Koenig, Y. Kuramitsu, C. C. Kuranz, D. Q. Lamb, D. Lee, M. J. Macdonald, C. D. Murphy, H.-S. Park, A. Pelka, A. Ravasio, Y. Sakawa, A. A. Schekochihin, A. Scopatz, P. Tzeferacos, W. C. Wan, N. C. Woolsey, R. Yurchak, B. Reville, and G. Gregori. Turbulent amplification of magnetic fields in laboratory laser-produced shock waves. *Nature Physics*, 10(June):2–6, 2014.

[22] A. L. Kraus, M. J. Ireland, L. A. Hillenbrand, and F. Martinache. The Role of Multiplicity in Disk Evolution and Planet Formation. *The Astrophysical Journal*, 745(1):19, 2012.

[23] R. O. Dendy. *Plasma Dynamics*. Oxford science publications. Clarendon Press, 1990.

[24] F. F. Chen. *Introduction to Plasma Physics and Controlled Fusion*. Number v. 1 in Introduction to Plasma Physics and Controlled Fusion. Springer, 2006.

[25] R. P. Drake. *High-Energy-Density Physics: Fundamentals, Inertial Fusion, and Experimental Astrophysics*. Shock Wave and High Pressure Phenomena. Springer, 2006.

[26] G. Aulanier, E. E. DeLuca, S. K. Antiochos, R. A. McMullen, and L. Golub. The Topology and Evolution of the Bastille Day Flare. *The Astrophysical Journal*, 540:1126–1142, 2000.

[27] M. Pfister and H. Chanson. Discussion of Scale effects in physical hydraulic engineering models By Valentin Heller, Journal of Hydraulic Research, Vol. 49, No. 3 (2011), pp. 293306. *Journal of Hydraulic Research*, 50(2):244–246, 2012.

[28] R. K. Saha, C. Zhang, and M. B. Ray. Similitude in an Open-Channel UV Wastewater Disinfection Reactor. *Journal of Environmental Engineering*, 141(3):1–10, 2015.

[29] H Alfvén. Existence of electromagnetic-hydrodynamic waves. *Nature*, 150(3805):405–406, 1942.

[30] B. Katz, R. Budnik, and E. Waxman. Fast Radiation Mediated Shocks and Supernova Shock Breakouts. *The Astrophysical Journal*, 716(1):781–791, June 2010.

[31] E. Falize, A. Dizière, and B. Loupias. Invariance concepts and scalability of two-temperature astrophysical radiating fluids. *Astrophysics and Space Science*, 336(1):201–205, 2011.

[32] E. Falize, S. Bouquet, and C. Michaut. Scaling laws for radiating fluids: the pillar of laboratory astrophysics. *Astrophysics and Space Science*, 322(1-4):107–111, January 2009.

[33] O. A. Hurricane, D. A. Callahan, D. T. Casey, P. M. Celliers, C. Cerjan, E. L. Dewald, T. R. Dittrich, T. Döppner, D. E. Hinkel, L. F. Berzak Hopkins, J. L. Kline, S. Le Pape, T. Ma, A. G. MacPhee, J. L. Milovich, A. Pak, H.-S. Park, P. K. Patel, B. A. Remington, J. D. Salmonson, P. T. Springer, and R. Tommasini. Fuel gain exceeding unity in an inertially confined fusion implosion. *Nature*, 506(7488):343–8, 2014.

[34] D. G. Sibeck, R. E. Lopez, and E. C. Roelof. Solar Wind Control of the Magnetopause Shape, Location and Motion. *Journal of Geophysical Research*, 96(A4):5489–5495, 1991.

[35] D. Tsakiris, G. and K. Eidmann. An approximate method for calculating Planck and Rosseland mean opacities in hot, dense plasmas. *Journal of Quantitative Spectroscopy and Radiative Transfer*, 38(5):353–368, 1987.

[36] J. E. Bailey, T. Nagayama, G. P. Loisel, G. A. Rochau, C. Blancard, J. Colgan, Ph. Cosse, G. Faussurier, C. J. Fontes, F. Gilleron, I. Golovkin, S. B. Hansen, C. A. Iglesias, D. P. Kilcrease, J. J. Macfarlane, R. C. Mancini, S. N. Nahar, C. Orban, J. Pain, A. K. Pradhan, M. Sherrill, and B. G. Wilson. A higher-than-predicted measurement of iron opacity at solar interior temperatures. *Nature Letters*, 517:56–60, 2014.

[37] J. E. Bailey, G. A. Rochau, R. C. Mancini, C. A. Iglesias, J. J. MacFarlane, I. E. Golovkin, C. Blancard, Ph. Cosse, and G. Faussurier. Experimental investigation of opacity models for stellar interior, inertial fusion, and high energy density plasmas. *Physics of Plasmas*, 16(5), 2009.

[38] D. Mihalas and B. Weibel-Mihalas. *Foundations of Radiation Hydrodynamics.* Dover Books on Physics. Dover, 1999.

[39] C. Michaut, É. Falize, C. Cavet, S. Bouquet, M. Koenig, T. Vinci, A. Reighard, and R. P. Drake. Classification of and recent research involving radiative shocks. *Astrophysics and Space Science*, 322(1-4):77–84, 2009.

[40] J.-P. Hansen and I. R. McDonald. *Theory of Simple Liquids.* 2013.

[41] S. H. Glenzer and R. Redmer. X-ray Thomson scattering in high energy density plasmas. *Reviews of Modern Physics*, 81:1625, 2009.

[42] S. Ichimaru. Strongly coupled plasmas: high-density classical plasmas and degenerate electron liquids. *Reviews of Modern Physics*, 54:1017, 1982.

[43] C. C. Kuranz, R. P. Drake, T. L. Donajowski, K. K. Dannenberg, M. Grosskopf, D. J. Kremer, C. Krauland, D. C. Marion, H. F. Robey, B. A. Remington, J. F. Hansen, B. E. Blue, J. Knauer, T. Plewa, and N. Hearn. Assessing mix layer amplitude in 3D decelerating interface experiments. *Astrophysics and Space Science*, 307(1-3):115–119, 2007.

[44] G. Gregori, A. Ravasio, C. D. Murphy, K. Schaar, A. Baird, A. R. Bell, A. Benuzzi-Mounaix, R. Bingham, C. Constantin, R. P. Drake, M. Edwards, E. T. Everson, C. D. Gregory, Y. Kuramitsu, W. Lau, J. Mithen, C. Niemann, H.-S. Park, B. A. Remington, B. Reville, A. P. L. Robinson, D. D. Ryutov, Y. Sakawa, S. Yang, N. C. Woolsey, M. Koenig, and F. Miniati. Generation of scaled protogalactic seed magnetic fields in laser-produced shock waves. *Nature*, 481(7382):480–3, January 2012.

[45] J. F. Hansen, M. J. Edwards, D. Froula, G. Gregori, A. Edens, and T. Ditmire. Laboratory Simulations of Supernova Shockwave Propagation. *Astrophysics and Space Science*, 298(1-2):61–67, July 2005.

[46] R. I. Klein, K. S. Budil, T. S. Perry, and D. R. Bach. The interaction of supernova remnants with interstellar clouds: experiments on the NOVA laser. *The Astrophysical Journal*, pages 245–259, 2003.

[47] M. Koenig, E. Henry, G. Huser, A. Benuzzi-Mounaix, B. Faral, E. Martinolli, S. Lepape, T. Vinci, D. Batani, M. Tomasini, B. Telaro, P. Loubeyre, T. Hall, P. Celliers, G. Collins, L. DaSilva, R. Cauble, D. Hicks, D. Bradley, A. MacKinnon, P. Patel, J. Eggert, J. Pasley, O. Willi, D. Neely, M. Notley, C. Danson, M. Borghesi, L. Romagnani, T. Boehly, and K. Lee. High pressures generated by laser driven shocks: applications to planetary physics. *Nuclear Fusion*, 44(12):S208–S214, 2004.

[48] M. D. Knudson, D. L. Hanson, J. E. Bailey, C. A. Hall, J. R. Asay, and C. Deeney. Principal Hugoniot, reverberating wave, and mechanical reshock measurements of liquid deuterium to 400 GPa using plate impact techniques. *Physical Review B*, 69(14):144209, 2004.

[49] R. Jeanloz, P. M. Celliers, G. W. Collins, J. H. Eggert, K. K. M. Lee, R. S. McWilliams, S. Brygoo, and P. Loubeyre. Achieving high-density states through shock-wave loading of precompressed samples. *Proceedings of the National Academy of Sciences of the United States of America*, 104(22):9172–7, May 2007.

[50] A. L. Kritcher, P. Neumayer, J. Castor, T. Döppner, R. W. Falcone, O. L. Landen, H. J. Lee, R. W. Lee, E. C. Morse, A. Ng, S. Pollaine, D. Price, and S. H. Glenzer. Ultrafast X-ray Thomson Scattering of Shock-Compressed Matter. *Science*, 322:69–71, 2008.

[51] E. García Saiz, G. Gregori, D. O. Gericke, J. Vorberger, B. Barbrel, R. J. Clarke, R. R. Freeman, S. H. Glenzer, F. Y. Khattak, M. Koenig, O. L. Landen, D. Neely, P. Neumayer, M. M. Notley, A. Pelka, D. Price, M. Roth, M. Schollmeier, C. Spindloe, R. L. Weber, L. van Woerkom, K. Wünsch, and D. Riley. Probing warm dense lithium by inelastic X-ray scattering. *Nature Physics*, 4(12):940–944, October 2008.

[52] D. Ryutov, R. P. Drake, J Kane, E. Liang, B. A. Remington, and W. M. Wood-Vasey. *The Astrophysical Journal*, (2):821–832.

[53] J. W. Connor and J. B. Taylor. Scaling laws for plasma confinement. *Nuclear Fusion*, 17:1047–1055, 1977.

[54] D. D. Ryutov, N. L. Kugland, H.-S. Park, C. Plechaty, B. A. Remington, and J. S. Ross. Basic scalings for collisionless-shock experiments in a plasma

without pre-imposed magnetic field. *Plasma Physics and Controlled Fusion*, 54(10):105021, October 2012.

[55] D. D. Ryutov, R. P. Drake, and B. A. Remington. Criteria for scaled laboratory simulations of astrophysical MHD phenomena. *The Astrophysical Journal*, 465(2):465–468, 2000.

[56] D. D. Ryutov, B. A. Remington, H. F. Robey, and R. P. Drake. Magnetohydrodynamic scaling: From astrophysics to the laboratory. *Physics of Plasmas*, 8(5):1804, 2001.

[57] É. Falize, C. Michaut, and S. Bouquet. Similarity Properties and Scaling Laws of Radiation Hydrodynamic Flows in Laboratory Astrophysics. *The Astrophysical Journal*, 730(2):96, April 2011.

[58] Y. B. Zel'dovich and Y. P. Raizer. *Physics of Shock Waves and High-temperature Hydrodynamic Phenomena.* Academic Press, 1966.

[59] R. G. McClarren, R. P. Drake, J. E. Morel, and J. P. Holloway. Theory of radiative shocks in the mixed, optically thick-thin case. *Physics of Plasmas*, 17(9):093301, 2010.

[60] F. Haas. *Quantum Plasmas: An Hydrodynamic Approach.* Springer, 2011.

[61] A. Chapman and T. G Cowling. *The Mathematical Theory of Non-Uniform Gases.* Cambridge University Press, 1970.

[62] F. H. Shu. *The Physics of Astrophysics Volume II: Gas Dynamics.* University Science Books, 1992.

[63] R. Schmidt, B. J. B. Crowley, J. Mithen, and G. Gregori. Quantum hydrodynamics of strongly coupled electron fluids. *Physical Review E*, 85:046408–046412, 2012.

[64] D. Bohm. A suggested interpretation of the quantum theory in terms of "hidden" variables. I. *Phys. Rev.*, 85(2):166–179, 1952.

[65] D. Mostacci, V. Molinari, and F. Pizzio. A Derivation of Quantum Kinetic Equation from Bohm Potential. *Transport Theory and Statistical Physics*, 37(5-7):589–600, 2008.

[66] I. Braginskii, S. Transport process in a plasma. *Reviews of Plasma Physics*, 1:205–311, 1965.

[67] L. Biermann. Uber den ursprung der magnetfelder auf sternen und im interstellaren raum. *Zeitschrift fur Naturforschung Section A*, 5(2):65–71, 1950.

[68] R. M. Kulsrud and E. G. Zweibel. On the origin of cosmic magnetic fields. *Reports on Progress in Physics*, 71:046901–046934, 2008.

[69] M. G. Haines. Heat flux effect in Ohm's Law. *Plasma Physics and Controlled Fusion*, 28(11):1705–1716, 1986.

[70] M. G. Haines. Magnetic-field generation in laser fusion and hot-electron transport. *Canadian Journal of Physics*, 64:912–918, 1986.

[71] Yabe T. Nishiguchi, A. and G. Haines, M. Nernst effect in laser-produced plasmas. *Physics of Fluids*, 28(12):3683–3690, 1985.

[72] M. J.-E. Manuel, C. K. Li, F. H. Seguin, N. Sinenian, J. A. Frenje, D. T. Casey, R. D. Petrasso, J. D. Hager, R. Betti, S. X. Hu, J. Delettrez, and D. D. Meyerhofer. Instability-driven electromagnetic fields in coronal plasmas. *Physics of Plasmas*, 20(5):056301–10, 2013.

[73] L. D. Landau and E. M. Lifshitz. *Fluid Mechanics.* Pergamon Press, 1959.

[74] J. I. Castor. *Radiation Hydrodynamics.* Cambridge University Press, 2004.

[75] D. W. Savin, N. S. Brickhouse, J. J. Cowan, R. P. Drake, S. R. Federman, G. J. Ferland, A. Frank, M. S. Gudipati, W. C. Haxton, E. Herbst, S. Profumo, F. Salama, L. M. Ziurys, and E. G. Zweibel. The impact of recent advances in laboratory astrophysics on our understanding of the cosmos. *Reports on Progress in Physics*, 75(3):036901, 2012.

[76] J. D. Huba. *Revised NRL Plasma Formulary.* Office of Naval Research, 2002.

[77] L. D. Landau, E. M. Lifshitz, and L. P. Pitaevskii. *Physical Kinetics.* 1981.

[78] R. S. Sutherland and M. A. Dopita. Cooling functions for low-density astrophysical plasmas. *The Astrophysical Journal*, 88:253–327, 1993.

[79] B. Reipurth and J. Bally. Herbig-Haro flows: Probes of early stellar evolution. *Annual Review of Astronomy and Astrophysics*, 39:403–55, 2001.

[80] C. M. Krauland, R. P. Drake, C. C. Kuranz, B. Loupias, T. Plewa, C. M. Huntington, D. N. Kaczala, S. Klein, R. Sweeney, R. P. Young, É. Falize, B. Villette, and P. A. Keiter.

[81] A. N. Kolmogorov. The local structure of turbulence in incompressible viscous fluid for very large Reynolds numbers. *Proceedings: Mathematical and Physical Sciences*, 434(1890):9–13, 1991.

[82] L. Boldsten and D. M. Hall. Gravitational settling of 22Ne in liquid white dwarf interiors. *The Astrophysical Journal*, 549:219–233, 2001.

[83] D. Lai. Matter in strong magnetic fields. *Reviews of Modern Physics*, 73(3):629–661, 2001.

[84] M. Zingale, A. S. Almgren, J. B. Bell, A. Nonaka, and S. E. Woosley. Low Mach Number Modeling of Type Ia Supernovae. Iv. White Dwarf Convection. *The Astrophysical Journal*, pages 196–210.

[85] W. F. Vinen. An Introduction to Quantum Turbulence. *Journal of Low Temperature Physics*, 148(1–4):7, 2006.

[86] A. C. Biswas and R. K. Pathria. Critical Velocity in Superfluid Helium. *Journal of Low Temperature Physics*, 28(1/2):151, 1976.

[87] N. Hopps, C. Danson, S. Duffield, D. Egan, S. Elsmere, M. Girling, E. Harvey, D. Hillier, M. Norman, S. Parker, P. Treadwell, D. Winter, and T. Bett. Overview of laser systems for the Orion facility at the AWE. *Applied Optics*, 52(15):3597–607, 2013.

[88] B. Warner. *Cataclysmic Variables.* Cambridge Univ. Press, 1995.

[89] M. Cropper. The Polars. *Space Science Reviews*, 54(3-4):195–295, 1990.

[90] J. Patterson. The evolution of cataclysmic and low-mass X-ray binaries. *The Astrophysical Journal Supplementary Series*, 54:443–493, 1984.

[91] É Falize, A. Ravasio, B. Loupias, A. Dizière, C. D. Gregory, C. Michaut, C. Busschaert, C. Cavet, and M. Koenig. High-energy density laboratory astrophysics studies of accretion shocks in magnetic cataclysmic variables. *High Energy Density Physics*, 8:1–4, 2012.

[92] I. Traulsen, K. Reinsch, R. Schwarz, S. Dreizler, K. Beuermann, A. D. Schwope, and V. Burwitz. X-ray spectroscopy and photometry of the long-period polar AI Tri with XMM-Newton. *Astronomy & Astrophysics*, 76:11, 2010.

[93] R. Schwarz, A. D. Schwope, K. Beuermann, V. Burwitz, J. Fischer, R. Fried, I. Lehmann, and K. Mantel. The new long-period AM Herculis system RX J0203 . 8 + 2959. *Astronomy & Astrophysics*, 478:465–478, 1998.

[94] J. Frank, A. R. King, and J.-P. Lasota. The soft X-ray excess in accreting magnetic white dwarfs. *Astronomy & Astrophysics*, 193:113–118, 1988.

[95] A. R. King. Blob model for polar accretion. *The Astrophysical Journal*, 20(1988):306–307, 2000.

[96] B. W. Greeley, W. P. Blair, K. S. Long, and J. C. Raymond. The Far-Ultraviolet Spectrum and Short Timescale Variability of AM Herculis from Observations with the Hopkins Ultraviolet Telescope. *The Astrophysical Journal*, 1(1982):491–505, 1998.

[97] C. Busschaert, É Falize, B. Loupias, C. Michaut, A. Ravasio, A. Pelka, R. Yurchak, and M. Koenig. POLAR project: A numerical study to optimize the target design. *New Journal of Physics*, 15:035020, 2013.

[98] C. Spindloe, D. Wyatt, D. Haddock, I. East, J.E. Cross, C.N. Danson, E. Falize, J.M. Foster, M. Koenig, and G. Gregori. Target fabrication for the POLAR experiment on the Orion laser facility. *High Power Laser Science and Engineering*, 3:e8, 2015.

[99] É. Falize, B. Loupias, A. Ravasio, C. D. Gregory, A. Dizière, M. Koenig, C. Michaut, C. Cavet, P. Barroso, J.-P. Leidinger, X. Ribeyre, J. Breil, H. Takabe, Y. Sakawa, Y. Kuramitsu, T. Morita, N. C. Woolsey, W. Nazarov, and S. Pikuz. The scalability of the accretion column in magnetic cataclysmic variables: the POLAR project. *Astrophysics and Space Science*, 336(1):81–85, March 2011.

[100] E. I. Moses and C. R. Wuest. The National Ignition Facility: Laser performance and first experiments. *Fusion Science and Technology*, 47(3):314, 2005.

[101] M. L. Andr. The French Megajoule Laser Project (LMJ). *Fusion Engineering and Design*, 44(14):43 – 49, 1999.

[102] N. Fleurot, C. Cavailler, and J. L. Bourgade. The Laser Megajoule (LMJ) Project dedicated to inertial confinement fusion: Development and construction status. *Fusion Engineering and Design*, 74(1-4):147–154, NOV 2005. 23rd Symposium on Fusion Technology (SOFT 23), Venice, ITALY, SEP 20-24, 2004.

[103] J.-P. Zou, A.-M. Sautivet, J. Fils, L. Martin, K. Abdeli, C. Sauteret, and B. Wattellier. Optimization of the dynamic wavefront control of a pulsed kilojoule/nanosecond-petawatt laser facility. *Applied Optics*, 47(5):704–710, 2008.

[104] L. M. Barker and R. E. Hollenbach. Laser interferometer for measuring high velocities of any reflecting surface. *Journal of Applied Physics*, 43(11):4669, 1972.

[105] J. J. MacFarlane, I. E. Golovkin, and P. R. Woodruff. HELIOS-CR A 1-D radiation-magnetohydrodynamics code with inline atomic kinetics modeling. *Journal of Quantitative Spectroscopy and Radiative Transfer*, 99(13):381 – 397, 2006. Radiative Properties of Hot Dense Matter.

[106] J. J. MacFarlane, I. E. Golovkin, P. Wang, P. R Woodruff, and N. A Pereyra. SPECT3D A multi-dimensional collisional-radiative code for generating diagnostic signatures based on hydrodynamics and {PIC} simulation output. *High Energy Density Physics*, 3(12):181 – 190, 2007. Radiative Properties of Hot Dense Matter.

[107] B. L. Henke, E. M. Gullikson, and J. C. Davis. X-ray interactions: photoabsorption, scattering, transmission, and reflection at E=50-30000 eV, Z=1-92. *Atomic Data and Nuclear Data Tables.*

[108] C. C. Kuranz, B. E. Blue, R. P. Drake, H. F. Robey, J. F. Hansen, J. P. Knauer, M. J. Grosskopf, C. Krauland, and D. C. Marion. Dual, orthogonal, backlit pinhole radiography in OMEGA experiments. *Review of Scientific Instruments*, 77(10), 2006.

[109] F. W. Doss, R. P. Drake, and E. S. Myra. Oblique radiative shocks, including their interactions with non-radiative polytropic shocks. *Physics of Plasmas*, 18(5):056901, 2011.

[110] F. W. Doss, H. F. Robey, R. P. Drake, and C. C. Kuranz. Wall shocks in high-energy-density shock tube experiments. *Physics of Plasmas*, 16(11):112705, 2009.

[111] C. C. Kuranz, F. W. Doss, R. P. Drake, M. J. Grosskopf, and H. F. Robey. Using wall shocks to measure preheat in laser-irradiated, high-energy-density, hydrodynamics experiments. *High Energy Density Physics*, 6(2):215 – 218, 2010. {ICHED} 2009 - 2nd International Conference on High Energy Density Physics.

[112] P. D. Roberts, S. J. Rose, P. C. Thompson, and R. J. Wright. The stability of multiple-shell ICF targets. *Journal of Physics D*, 13(11):1957–1969, 1980.

[113] J. A. Fleck and J. D. Cummings. An implicit Monte Carlo scheme for calculating time and frequency dependent nonlinear radiation transport. *Journal of Computational Physics*, 8(3):313, 1971.

[114] B. J. B. Crowley and J. W. O. Harris. Modelling of plasmas in an average-atom local density approximation: the CASSANDRA code. *Journal of Quantitative Spectroscopy & Radiative Transfer*, 71(2-6):257–272, 2001.

[115] K. S. Holian. *T-4 handbook of material properties data bases. Vol Ic: Equations of state*, Los Alamos National Laboratory Report No. LA-10160-MS, 1984.

[116] D. L. Youngs. Numerical-simulation of turbulent mixing by Rayleigh-Taylor instability. *Physica D*, 12(1-3):32, 1984.

[117] P. A. Keiter, R. P. Drake, T. S. Perry, H. F. Robey, B. A. Remington, C. A. Iglesias, R. J. Wallace, and J. Knauer. Observation of a hydrodynamically driven, radiative-precursor shock. *Physical Review Letters*, 89(16):165003, 2002.

[118] D. Q. Lamb and A. Masters. X and UV radiation from accreting magnetic degenerate dwarfs. *The Astrophysical Journal*, 234:L117–L122, 1979.

[119] K. Wu, G. Chanmugam, and G. Shaviv. Structure of steady state accretion shocks with several cooling functions: Closed integral-form solution. *The Astrophysical Journal*, 426:664–668, 1994.

[120] É. Falize, C. Michaut, C. Cavet, S. Bouquet, M. Koenig, B. Loupias, A. Ravasio, and G. Gregory, C. Scaling laws for radiating fluids: the pillar of laboratory astrophysics. *Astrophysics and Space Science*, 322:71–75, 2009.

[121] T. Guillot. Interiors of giant planets inside end outside the solar system. *Science*, 286(5437):72–77, 1999.

[122] J. Daligault and S. Gupta. Electron-ion scattering in dense multi-component plasmas: application to the outer crust of an accreting neutron star. *The Astrophysical Journal*, 703(1):994, 2009.

[123] M. D. Knudson, M. P. Desjarlais, and D. H. Dolan. Shock-Wave Exploration of the High-Pressure Phases of Carbon. *Science*, 322(5909):1822, 2008.

[124] T. G. White, S. Richardson, B. J. B. Crowley, L. K. Pattison, J. W. O. Harris, and G. Gregori. *Physical Review Letters*, (17):175002.

[125] J. Lindl. Development of the indirect-drive approach to inertial confinement fusion and the target physics basis for ignition and gain. *Physics of Plasmas*, 2:3933, 1995.

[126] G. Gregori, S. H. Glenzer, W. Rozmus, R. W. Lee, and R. W. Landen. Theoretical model of x-ray scattering as a dense matter probe. *Physical Review E*, 67(2):026412, 2003.

[127] J. P. Mithen, J. Daligault, and G. Gregori. Extent of validity of the hydrodynamic description of ions in dense plasmas. *Phys. Rev. E*, 83(1):015401(R), 2011.

[128] I. R. McDonald, P. Vieillefosse, and J.-P. Hansen. Time-Dependent Density Fluctuations in a Strongly Coupled Ionic Mixture. *Physical Review Letters*, 39(5):271, 1977.

[129] J. P. Mithen, J. Daligault, B. J. B. Crowley, and G. Gregori. Density fluctuations in the Yukawa one-component plasma: An accurate model for the dynamical structure factor. *Phys. Rev. E*, 84(2):046401, 2011.

[130] J. P. Boon and S. Yip. *Molecular Hydrodynamics.* Dover Publications, 1991.